ZINC OXIDE: A SPECTROSCOPIC INVESTIGATION OF BULK CRYSTALS AND THIN FILMS

A thesis submitted in partial fulfilment of the requirements for the

Degree of

Doctor of Philosophy

in Physics

at the University of Canterbury

by Paul Miller

University of Canterbury

Christchurch, New Zealand

2008

Abstract

The optical properties of zinc oxide crystals and thin films prepared by different methods are investigated.

Single crystal zinc oxide samples prepared by melt and hydrothermal growth techniques were obtained. The influence of polarity and growth method on the optical properties were studied and correlated with their electronic properties.

Thin films prepared by molecular beam epitaxy (MBE) and sputtering were studied and the influence of growth conditions and post growth treatment on the optical properties of the films was investigated.

The photo-luminescence (PL) of bulk zinc oxide was examined at high resolution. Line widths of less than 0.1 meV were observed. More than a dozen different transitions in the near band edge region (NBE 360-380 nm) were noted, several of which displayed a separation of <0.5 meV which goes some way to illustrating the complexity of the system. Attempts were made, with some success, to reconcile the two main competing identification systems of the NBE transitions and explanations for some of the discrepancies are provided.

The controversial deep level transitions in the visible part of the spectrum are fit with 3 Gaussians and their identities discussed with relation to the available literature. The presence of copper impurities was detected in annealed films and a model to explain their behaviour under annealing conditions is hypothesised.

Films grown by MBE here at the University of Canterbury are shown to have PL line widths of as little as 2.2 meV, the ratio of active oxygen species in the growth chamber during deposition is shown to effect the optical quality of the films. It is shown that annealing can improve the optical quality of the films and various other methods of influencing the films properties are discussed.

Reactive, magnetron, direct current sputtering is shown to be the optimal method of growth for maximising both optical and piezo-electric properties.

Optimum annealing temperatures were found at 900 and 1100 ^{o}C with a local minimum at 1000 ^{o}C. X-ray diffraction, atomic force and scanning electron microscopy measurements in addition to optical PL measurements show the influence of annealing on the polycrystalline sputtered ZnO films. Films grown on glass, silicon, sapphire and quartz were shown to display similar behaviour under annealing conditions. It was found that zinc oxide based devices were liable to be chemically unstable at temperatures above 1100 ^{o}C.

The piezo electric properties of the films were examined and attempts were made to prepare a zinc oxide film optimised for both optical quality and piezo-electric properties for possible future applications of a hybrid opto-mechanical coupled devices.

Acknowledgements

To my supervisor, Dr Roger Reeves and my associate supervisor Dr Steve Durbin, I extend my eternal thanks for your endless patience and support. There would be no thesis without your guidance and experience.

There are those whose own work has contributed significantly to this thesis.

William Lee and Leo Schuler who, by their own efforts, grew most of the materials investigated. This thesis is largely the result of your hard work. It was a pleasure to work with you both.

Martin Allen whose vast knowledge of the literature and continued high expectations has been the impetus for the dramatic improvement in experimental results over the last two years.

My work and office mates who have provided assistance, discussion and answers whenever asked. Scott Choi, Ian Farrell, Martin Henseler, Reuben Mendelsberg, Young-Wook Song, and Lyndon Williams.

Dr Zheng Wei Li and Dr Wei Gao of Auckland University whose collaboration contributed to my early thesis work.

There are the technical staff, Wayne Smith, Geoff Graham, Stephen Hemmingsen, Ross Ritchie who turned a 1960's relic into a state of the art spectrometer and a dusty room into a world class spectroscopy lab. Your talents never cease to amaze.

To Rhonda Sullivan, Rosalie Reilly and Gill Evans, for looking the other way when contracts and reports were submitted late, and for being on my side.

Professors Simon Brown, Mike Reid, Phil Butler, Rod Syme and Adrian McDonald who have inspired and motivated at various times throughout the course of this thesis. You have kept me on the path.

I thank you all

This work has been funded by the MacDiarmid Institute for Advanced Materials and Nanotechnology, the University of Canterbury, and all of you friendly and generous taxpayers.

To my friends, without whom this thesis would have been completed two years sooner and been twice as long.

To my Nana and Pop, from whom all things have been made possible. This is for you.

Most importantly, and without reserve, I would like to thank my beautiful wife Veronica, there are not words, but that a day does not pass in which I do not try to find them.

I love you.

Contents

Figures

Tables

1 Introduction

The aim of this thesis is to investigate the optical properties of zinc oxide prepared by a variety of different methods and under a variety of different conditions. Zinc oxide is a wide band gap semiconductor that emits in the UV. It has many potential device applications and it is hoped that the understanding gained in this thesis will contribute in some way to the advancement of this field of research.

1.1 History of Semiconductors

The early days of semiconductor research are an inspiring testament to the efficacy of the scientific method and the power of rigorous observation. Consider, if you will, these three excerpts from cornerstone papers on semiconductors and optoelectronics.

> Very extraordinary
> 316. *Sulphures of Silver-very extraordinary.* At first on piece of glass flask in after, afterwards in tube, fuzed into its place in fire.
> 317. When all was cold conducted a little (by galvanometer) and if quite cold at first conducting power did not increase. But if battery current strong from recent immersion of plates or if sulphuret warmed a little by a lamp-then as contact with poles continued the sulphured continued to increase in conducting power as shewn by the galvanometer, and at last needle jumped into a position perpendicular to that of the coil as if on a sudden the whole electricity of battery had passed; this then continued as long as contact continued. *The heat rose as the conducting power increased* (a curious fact), no other source of heat than the current being present. Yet I do not think it became high enough to fuze the sulphured. The whole passed whilst in the solid state. The hot sulphured seems to conduct as a metal would, and could get sparks with wires at the end and a fine spark with charcoal.
> 318. The sulphured when hot seems to me very much to resemble the metals in their usual state as to electrical relations, a conductor,
>
> I have lately met with an extraordinary case … which is in direct contrast with the influence of heat upon metallic bodies … On applying a lamp … the conducting power rose rapidly with the heat … On removing the lamp and allowing the heat to fall, the effects were reversed.

Excerpt from the diary of Michael Faraday and the subsequent paper in 1833, detailing the first observation of semiconductor behaviour[1]

> On the conduction of power
> through sulphur metals
> With a large quantity of natural and artificial metallic sulfides and greatly varying pieces, the most perfectly formed crystals that I could find, as well as coarse samples, I discovered that their resistance varied with the direction, intensity and duration of the current. The differences amount up to 30% of the total amount.

Braun investigates rectifying diode behaviour, 1874, initiates systematic semiconductor research[2]

> A Note on Carborundum
> To the editors of Electrical World:

Sirs:- During an investigation of the unsymetric passage of current through a contact of carborundum and other substances a curious phenomenon was noted. On applying a potential of 10 Volts between two points on a crystal of carborundum, the crystal gave out a yellowish light. Only one or two specimens could be found which gave a bright glow on such a low voltage, but with 110 Volts a large number could be found to glow. In some crystals only edges gave the light and others gave instead of a yellow light green, orange or blue. In all cases tested the glow appears to come from the negative pole, a bright blue-green spark appearing at the positive pole. In a single crystal, if the contact, if contact is made near the centre with the negative pole, and the positive pole is put in contact at any other place, only one section of the crystal will glow and that the same section wherever the positive pole is place.

There seems to be some connection between the above effect and the e.m.f. produced by a junction of carborundum and another conductor when heated by a direct or alternating current; but the connection may be only secondary as an obvious explanation of the e.m.f. effect is the thermoelectronic one. The writer would be glad of references to any published account of an investigation of this or any allied phenomena.

New York, N. Y. H. J. Round.

Round; *Electrical World* 1907, reporting the first observation of electroluminescence from a rectifying diode.[3]

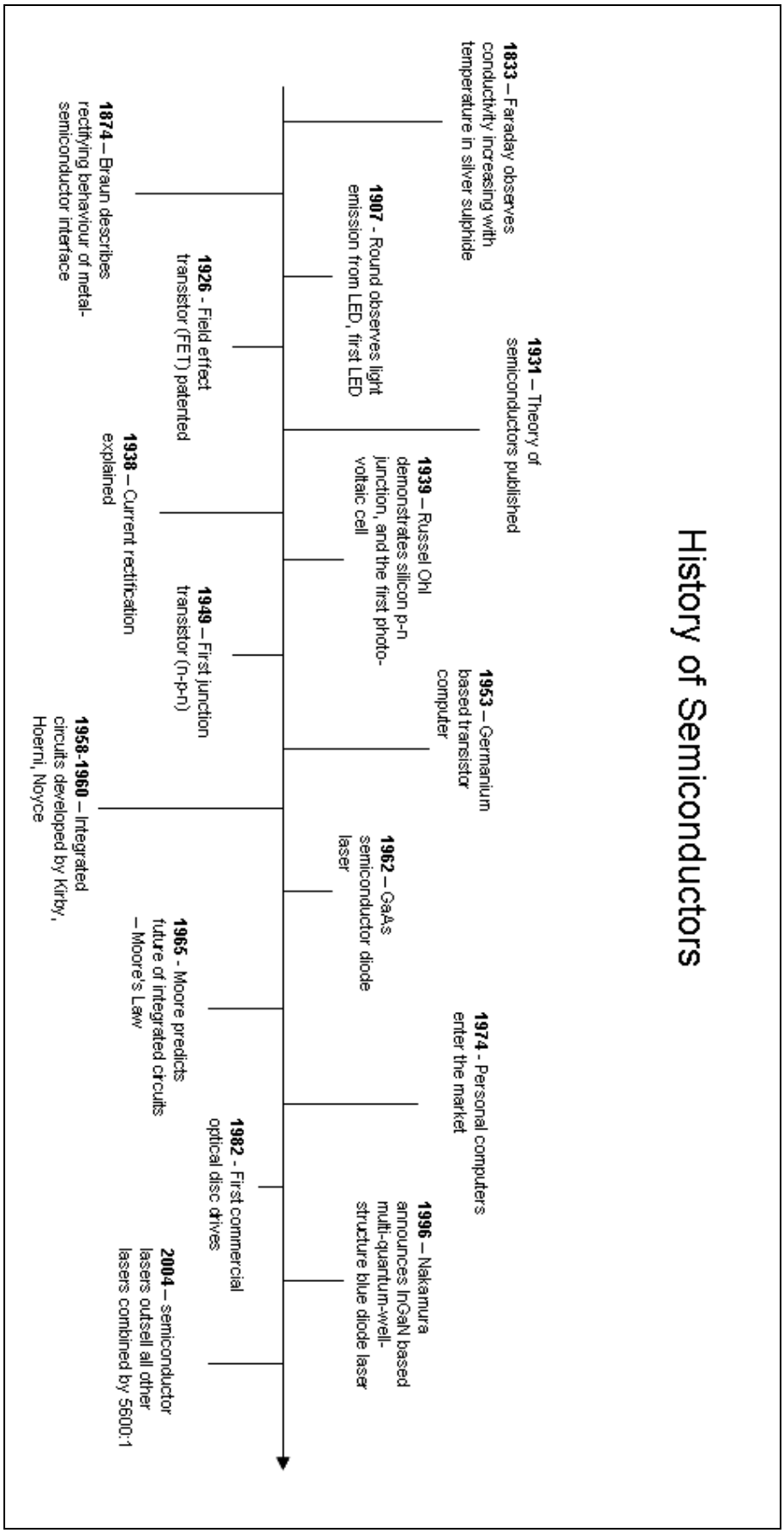

Figure 1-1 Timeline history of semiconductors

The impact that semiconductors have had on our society can not be denied. The development of the silicon microchip and the subsequent ability to process large amounts of data rapidly have revolutionised the way we interact, play and do business. Less obvious, but of growing importance, is the role of semiconductors in lighting. In an increasingly environmentally conscious world, energy savings are being sought wherever possible and lighting is an area which has been plagued by inefficiency since the inception of the incandescent bulb. Attempts have recently been made to supplant the incandescent with compact fluorescent bulbs. An 80% reduction in power consumption for the equivalent incandescent luminescence illustrated their potential, however their large size, slow start-up, and the 5 grams of mercury per bulb limit the overall appeal.

With an even more impressive 85% reduction in power consumption for the equivalent incandescent output, and sharing none of the drawbacks of the compact fluorescent bulbs, LED lighting appears to be the solution. Predicted lifetimes of 20 years, no moving parts and limited thermal output mean that LED's truly do have the potential to revolutionise the lighting industry.

However while the performance of the new technology is there, the pricing is not. For this reason, research continues to advance in improving the design and efficiency of the technology. One of the largest barriers to be overcome is filling in the blue/UV part of the spectrum. While cheap reliable LED lighting solutions exist for the green and red part of the spectrum, the blue/UV region still remains problematic.

One of the chief sources of human produced greenhouse emissions is from the generation of electrical power. Despite the growth of nuclear power generation, which has problems of its own, the vast majority of the worlds power is produced by a combination of coal, oil and natural gas. In addition to the environmental impact of these production methods, increasing competition for finite, non renewable resources has negative consequences for global political stability.

For these two reasons, alternative sources of power generation are being sought worldwide.

With approximately 4 billion years of remaining fuel, the sun offers an excellent source of power, readily available to large parts of the world. Tapping that power

however has proved to be non-trivial. While solar cell technology has been around for close to 60 years it has suffered consistently from poor cost effectiveness. While that figure has gradually been improving, due to both improvements in cell technology and increases in the cost of fossil fuels, much work remains to be done.

Optical storage disks based on semiconductor lasers have been around for 30 years now and over that time their storage density has increased considerably.

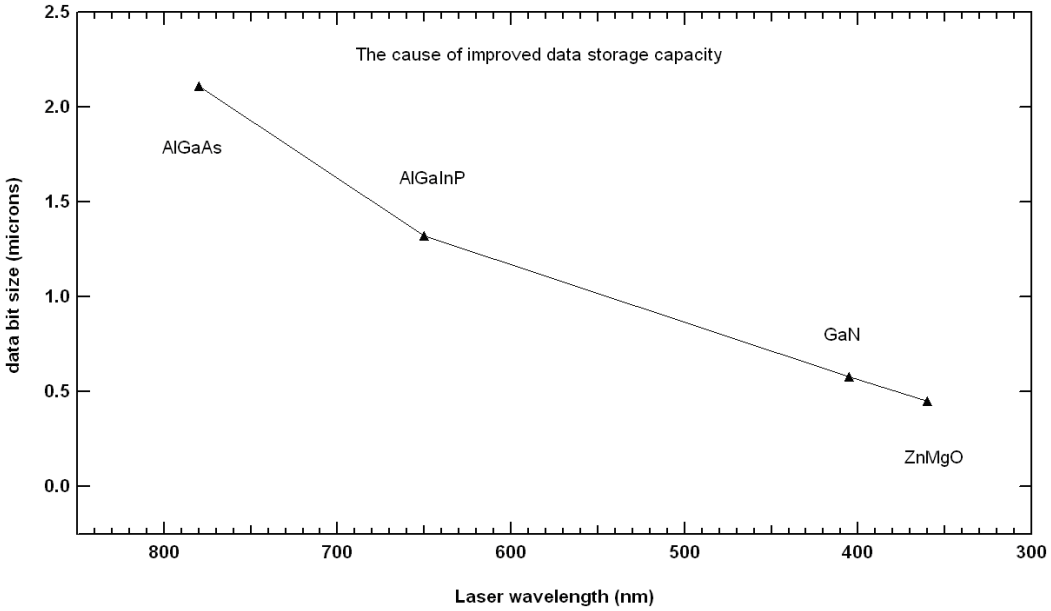

Figure 1-2 The potential role of ZnMgO in improving digital data storage capacity

This increase is largely the result of a steady reduction in the wavelength of the semiconductor lasers used to read the data from the disk, as shown in Figure 1-2.
The smallest size “data-bit” capable of being read by the laser is limited by the lasers wavelength, decreasing the laser wavelength allows smaller bits which in turns allows for increased data density on the disk. Currently Blue-Ray players use lasers with a wavelength of 405 nm to read data bits that are 580 nm in size. The development of a true UV laser would allow for an even greater reduction in bit size and a subsequent increase in storage capacity.

A side effect of advances in biology and the physical sciences has been a comparable advance in the sophistication of biological and chemical weapons. With the spectre of terrorism on the rise and increasingly in the public eye, law enforcement and national security begin to take on increased public significance. Early detection and improved border security will become ever more dependent on high tech monitoring devices.

Surface Acoustic Wave (SAW) devices have already been successfully used as gas and biological sensors and their use can only be expected to grow in the future.

Many challenges and opportunities of the present and future have been listed. A common thread that joins them all is the potential application of zinc oxide based devices, any one of which provides suitable motivation for further investigation. Zinc oxide is an old, well known material, which has already found many practical uses in the past, including medicine, food, paint, cleaning products and cosmetics. With the right motivation, interest and funding, that list is set to grow further still. Advances in thin film growth technology have opened up a new world of possibilities for zinc oxide ready to be explored and exploited.

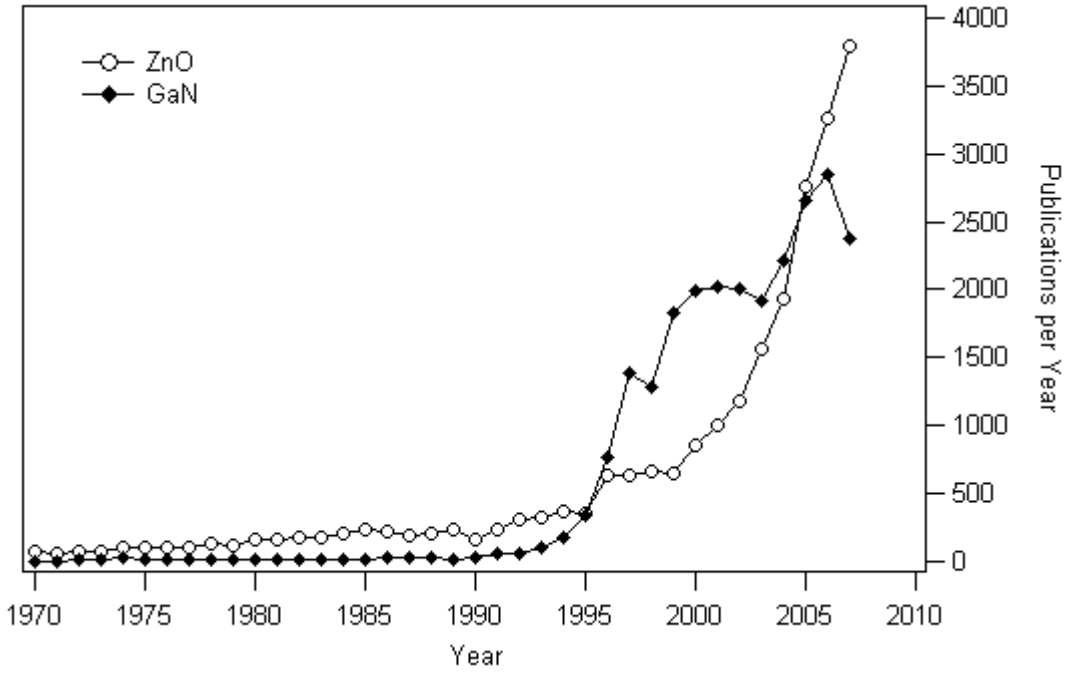

Figure 1-3 Growing interest in ZnO and declining interest in GaN

This is why, despite the many difficulties along the way, global interest in ZnO continues to increase.

Figure 1-3 shows the rate at which interest in ZnO is increasing, even as interest in the primary alternative material (GaN) declines.

1.2 Theory of semiconductors

The electrons of a single isolated atom occupy discrete atomic orbitals (1s, 2s, 2p, 3s etc). Each orbital has a discrete energy that depends on the properties of the atom. The electrons position in space is described by its wave function.

The Coulomb potential (V) for the valence electron is negative and inversely proportional to the distance of the electron from the atom.

$$V(r) = -k\frac{q}{r}$$

The potential describes a well, asymptotic around r = 0. The atomic orbitals occupy discrete levels within the well, the discrete levels are the Eigen energies of the solution to the time independent Schrödinger equation in a finite potential well.

When two identical atoms are bought into close proximity the wave functions of the electrons in the outer (valence) orbitals may overlap. The Pauli exclusion principle holds that no two identical fermions may occupy the same point in space at the same time. The corresponding energy levels in each atom are split (by atomic interactions), such that the exclusion principle is not violated by the overlapping wave functions.

Coupling a third atom to the system induces an additional splitting of each overlapping energy level. As a rule, each energy level is split into n sublevels for a given number of n atoms, resulting in a “band” of n closely spaced energy levels.

Since each sublevel has the same origin the spacing between them is very small, sufficiently small that an electron may move freely between sublevels within a band through a simple exchange of energy with the lattice (phonons), or through the emission of low frequency electromagnetic radiation.

Each energy band can be shown to have a density of states that describes the number of electron states in a given energy range.

The gap between the parent energy levels in the outer shell of the atoms is typically a few eV, this follows through to the many atom scenario although that spacing will vary depending on the broadening of each band (as described by the density of states) and the influence of the Coulomb interaction with neighbouring atoms.

Due to their homogeneity, atoms of the same type that coalesce into a solid will tend to arrange themselves in a periodic lattice structure that represents an energetically favourable configuration. Thus, for a sufficiently large number of atoms, an electron will observe a series of overlapping *periodic* wave functions extending semi-infinitely in all directions. Since we are able to calculate its energy exactly, its position must be completely unknown and thus extends through the lattice.

Electrons will tend to seek the lowest energy state available to them and for this reason, if we ignore the effects of thermal energy, they will tend to fill a band from the bottom up. The level to which the electrons fill up is called the Fermi level and at T = 0K there is 100% occupancy below, and 0% occupancy above.

A material with a fully occupied band and a large spacing between the occupied band and the next available band will be unable to conduct an electrical current. In order for there to be current, charge (electrons) must move, for charge to move it must be given energy.

In the case of the filled band, the energy of the electron plus the energy imparted by an applied e.m.f. would promote the electron to an already occupied energy level within the band, or to a level within the forbidden zone above the band (which we recall as a consequence of solving the time independent Schrödinger equation for an electron in a finite potential). Thus no conduction can occur and the material is an insulator. In certain cases, if the gap between the valence and conduction band is sufficiently small, enough electrons may gain enough energy to jump across the gap and therefore be available for conduction, this subset of materials are called “semi-conductors”. In such a material introducing additional charge carriers through doping can dramatically increase conductivity.

On the other hand, a material with a half filled band will conduct a current as electrons within the half filled band can be given enough energy to promote them to an unoccupied level within the band. This type of material is considered a metal, and is highly conductive.

A third alternative is for a fully occupied band to overlap with an empty band, in this case the available states in the empty band are close enough to be occupied by conducting electrons. This material is also a metal, though typically not as conductive as the "half filled band" metals. Figure 1-4 illustrates these scenarios.

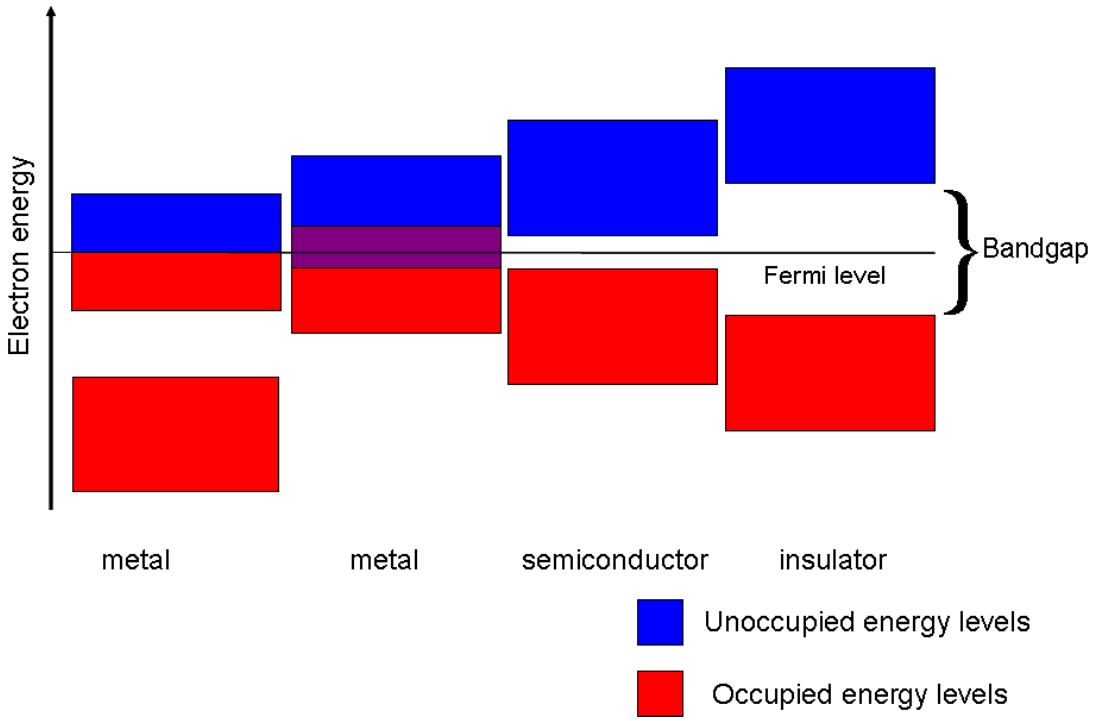

Figure 1-4 Bandgap diagram

The valency of the atom, that is to say whether the atoms have 1, 2, 3, or 4 electrons in the outer atomic orbital, and the number of atoms per unit cell (which reflects the periodicity and structure of the lattice) will determine how many electrons are available to occupy the energy levels of the bands.

Electrons can have spin up, or spin down and as a result there may be two electrons per energy level without violating the Pauli exclusion principle. An energy band may contain 2N electrons, where N is the number of unit cells in the lattice.

An element with an odd number of valence electrons will always be a metal, as the highest occupied band will always be partially filled.

An element with an even number of valence electrons will be a metal if the valence band overlaps with a higher unoccupied band, otherwise it will be an insulator.

1.3 Properties of ZnO

1.3.1 General Properties

Zinc oxide is a group II-VI semiconductor that most commonly exhibits wurtzite structure in its unstrained phase, . It belongs to the C^4_{6v} space group, also known as $P6_3mc$. At pressures above 8 GPa[4, 5] it undergoes a phase change to rocksalt structure, It has also been shown to grow in zincblend phase as a thin film on GaAs substrates[6].
This thesis will deal exclusively with the wurtzite phase of growth.

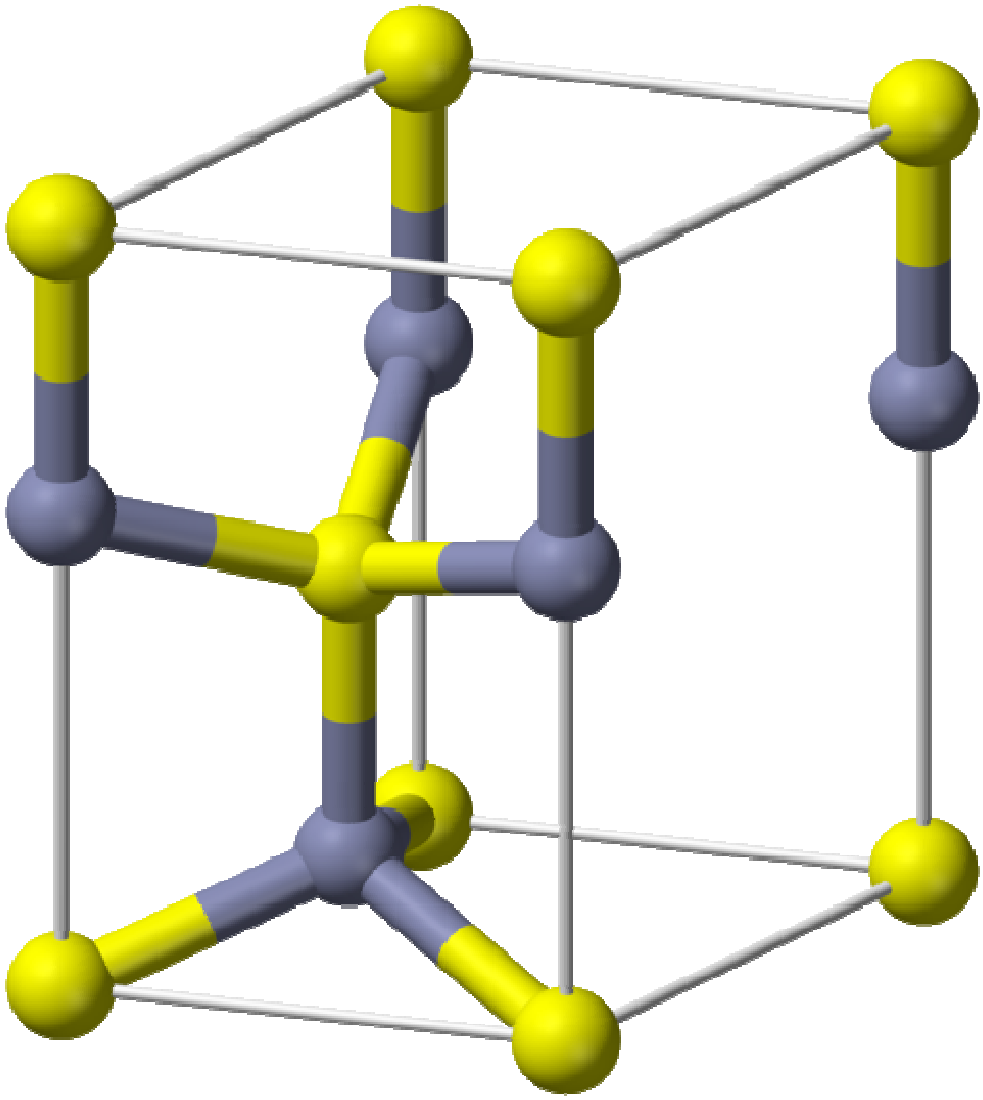

Figure 1-5 Unit cell of wurtzite ZnO

Figure 1-5 shows the unit cell. There are 4 atoms per unit cell.

Wurtzite crystals can be cleaved cleanly along several different planes. The c-plane (0001) intercepts only the z axis and in the case of zinc oxide produces polar surfaces as a consequence of the lack of inversion symmetry along the c axis.

There are also three non-polar cuts. a-plane (11-20) and m-plane (1-100) which intercept only the x/y axis and r-plane which intercepts all three and can be represented equivalently as (1-102), (1102), (01-12), (1012) or (10-12).

It is almost impossible to talk about ZnO as a semiconductor without also mentioning GaN. Many devices today already make use of GaN as a blue/UV light emitter, and with the cost, in both time and money, of developing new materials as high as it is, it

would not be unreasonable to question the value of additional research into ZnO. Table 1-1 shows that the crystal structure, lattice parameters, bandgap, melting point and density are all remarkably similar. Why then are alternative materials being sought even as the technology behind fabricating GaN devices is finally being perfected?

Properties	ZnO	GaN
Preferred phase	wurtzite	wurtzite
lattice parameters	a = 3.250 Å, c = 5.207 Å.	a = 3.189 Å, c = 5.185 Å.
bandgap	3.37 eV @ 300K	3.4 eV @ 300K
melting point	1975 C	>2500 C, decomposes to Ga & N_2
Density (solid)	5.6 g/cm^3	6.15 g/cm^3
Exciton binding energy	60 meV	25 meV

Table 1-1 Properties of ZnO and GaN

The exciton binding energy marks a key point of difference between the two materials. This binding energy is an indication of the strength of the bond between an electron-hole pair (exciton). The stronger the bond, the less likely the pair is to be dissociated by thermal energy or other effects. The spatial proximity of the electron-hole pair bound as an exciton greatly enhances the probability of the electron and hole recombining, and thus improves the probability of a photon being emitted. For opto-electronic devices this efficiency is key to their success or failure. Room temperature is equivalent to 25 meV, compared to the GaN exciton binding energy of 25 meV. Therefore the probability of a GaN exciton being dissociated by thermal energy at room temperature is undesirably high. This places a hard limit on the efficiency of future GaN based opto-electronic devices. ZnO on the other hand has an exciton binding energy of 60 meV, considerably higher than that of room temperature. This means that ZnO excitons will remain bound at much higher temperatures than GaN and in doing so, offer the potential for greatly improved efficiency over GaN.

For comparison, we calculate the surviving population of excitons at room temperature as a fraction of the total number of excitons at 0 K. where N_0 is the number of excitons at 0 K, T is the temperature and k is the Boltzmann constant.

$$N(T) = N_0(1 - e^{-\left(\frac{E_b}{kT}\right)})$$

kT at 300K = 25.8 meV
E_{bGaN} = 25 meV
E_{bZnO} = 60 meV

at 300 K (room temp) the % of excitons that have been thermalised is:
GaN 38%
ZnO 10%

Since a thermalised exciton is far less likely to recombine to produce a photon, this clearly shows why ZnO may be the preferred choice for future opto-electronic devices.

Additional advantages include an amenability to wet and dry etching[7-9] which constitutes an important part of process engineering. Zinc is also considerably more abundant than gallium which is a factor in the cost. It has been experimentally shown to be resistant to radiation damage which has positive implications for space applications.

The band gap of ZnO can be tuned via divalent substitution on the zinc site. Cadmium substitution can lower the bandgap to 3.0 eV[10-12] while magnesium alloying can be used to raise the bandgap up to 4 eV[13-15].

Another key feature of zinc oxide is its classification as a direct band-gap semiconductor. This allows direct electron-hole recombination without requiring a momentum exchange, usually via phonon production. This greatly enhances the optical efficiency of the material and sets it apart from indirect semi-conductors such as silicon.

1.3.2 Band Structure

A complete understanding of the energy band structure of zinc oxide is important, in order to properly utilise the material in various device applications.

The band structure of ZnO was first calculated in 1969 using Greens function[7] and followed up soon after with experimental results from x-ray induced photo-emission spectroscopy and UV photoemission measurements. The results were controversial and remained contradictory for many years[17-19]. More recently, advances in the computational power provided by computers has allowed for the most detailed calculation of the band structure of ZnO to date, using the linear-muffin-tin-orbital method[8].

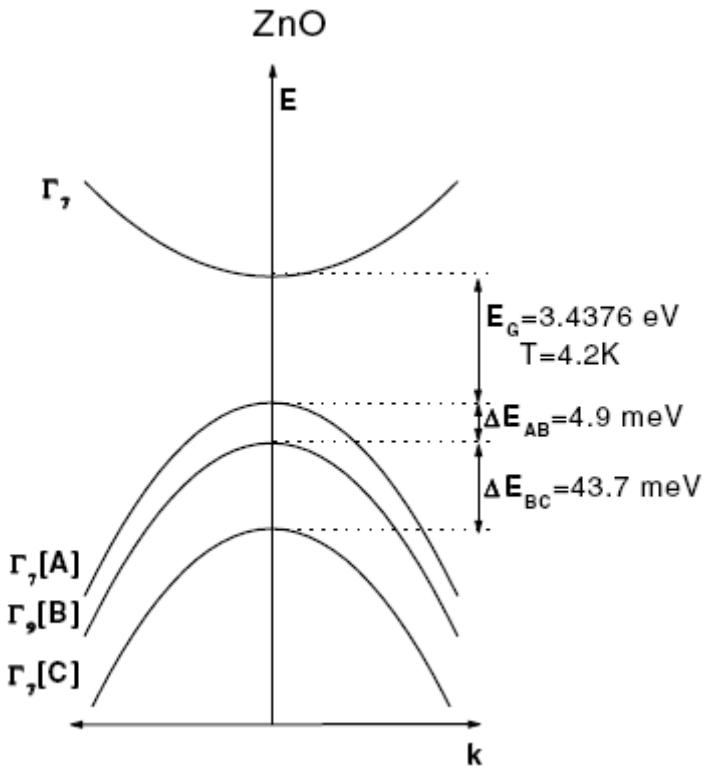

Figure 1-6 ZnO band structure diagram

The valence band of zinc oxide shown in Figure 1-6 is split by the crystal field and spin orbit interactions into three levels labelled A, B and C. The symmetry of the upper valence band (A) is the subject of much controversy[9-11]. While common opinion held for a long time that the upper valence band held Γ_7 symmetry, based on polarisation results of the free exciton, more recent magneto-optical results can be interpreted as showing Γ_9 symmetry however these results are further contradicted by a complexified interpretation of the results. The consequences of this confusion are a

reduced understanding of the various theoretically calculated transitions and greatly reduced confidence in the identification of the various optical emissions observed in the sample.

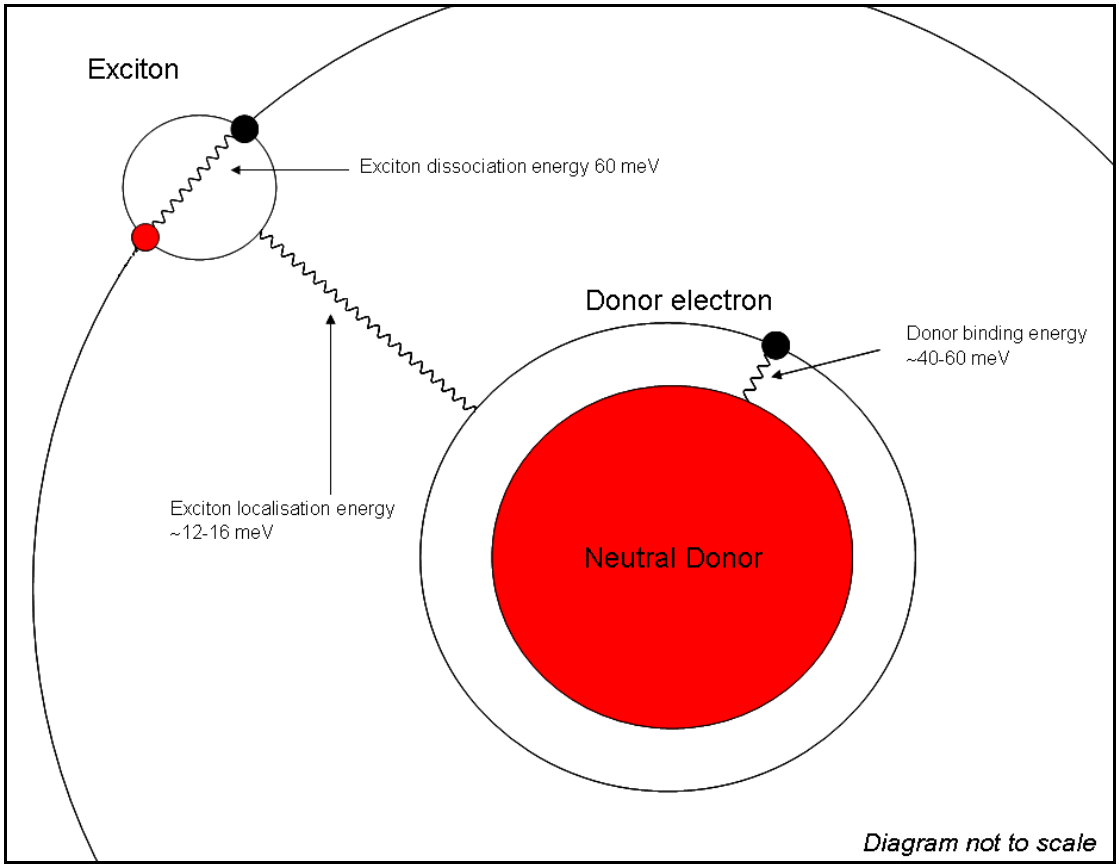

Figure 1-7 Representation of exciton bound to neutral donor

The PL spectrum of ZnO contains many unique and interesting features. To help visualise the various mechanisms by which the emission peaks are generated a diagram has been constructed to facilitate understanding, Figure 1-7. A dominant source of emission is from the recombination of free excitons, in which the photoemission is observed at an energy equal to the bandgap of the material, less the binding energy of the electron and the hole which comprise the exciton (the dissociation energy), most commonly referred to as F_X.

Another dominant emission is from an exciton weakly bound to a neutral donor. The photoemission is observed at an energy equivalent to the bandgap, less the exciton dissociation energy, less the binding energy of the exciton to the neutral donor (the localisation energy), this transition is most commonly notated as D^0X, an exciton bound

to a neutral acceptor would be referred to as A^0X. This localisation can be further modified in several different ways.

When bound to a donor the exciton can be loosely treated as a simple hydrogen atom model with the donor representing the nucleus and the exciton representing the bound charge. For the exciton in its ground state orbital around the donor, it's recombination is the previously mentioned neutral donor bound exciton. However if the exciton is excited to its second orbital energy level (and as such the localisation energy is reduced) the recombination occurs at a slightly higher energy. This is traditionally referred to as the Rotator state (R) and appears at an energy slightly below that of the free exciton emission.

Another transition commonly observed in high quality material is the two electron satellite (TES). In this instance the donor electron is excited to a higher orbital energy level, in the process increasing the binding energy of the exciton-donor atom. This has the effect of increasing the localisation energy and thus decreasing the energy of the observed emission by an amount equal to the energy difference between the donor electron in it's ground and first excited states. An observation of this transition is useful in determining the binding energy of the donor electron, which can be calculated approximately as 4/3 the energy difference between D^0X and the TES[9].

All of these excitons are typically ascribed to an electron in the conduction band bound by a mutual Coulomb attraction to a hole in the upper valence band (A) however it is also possible for a relatively stable exciton to form between an electron in the conduction band and a hole in the B valence band. Unless otherwise specified it assumed that the previously mentioned notations refer to the A exciton, however in the case where both A and B excitons are observed, the notations are identified with a subscript $D^0X_{A,B}$ depending on the case.

1.3.3 Review Papers

The most significant applications of ZnO include Blue/UV solid state optical devices such as white light LED's, thin film transparent conducting oxides as the front contact for improved efficiency solar cells, conductive gas sensors, and surface acoustical wave (SAW) devices that make use of ZnO's piezoelasticity.

ZnO has been produced using a large number of different methods. Bulk crystals can be grown using Melt, hydrothermal and vapour phase growth techniques.
Thin films have been grown by pulsed laser deposition, sputtering, molecular beam epitaxy, metalorganic chemical vapour deposition, chemical spray pyrolosis, thermal oxidation of zinc, sol-gel, and arc discharge. Each of the methods offers various benefits over the others, whether it be price, speed, quality or scalability. For this reason no single method of growth should be discounted.
The chief impediment to large scale implementation of ZnO photonic devices is the absence of a repeatable transferable method of producing p-type ZnO. Although an increasing number of research groups have successfully grown p-type material of their own[12-14], it has tended to be short lived, or non repeatable.

A number of excellent review papers have been published on various aspects of ZnO growth, characterisation and processing.

Epitaxial growth of ZnO films: Triboulet, Perriere 2003[15]
Recent progress in processing and properties of ZnO: Pearton et al.2005[16]
Bound exciton and Donor-Acceptor pair recombinations in ZnO: B. K. Meyer et al. 2004[9]
A comprehensive review of ZnO and related devices: U. Ozgur et al. 2005[17]
The future of ZnO light emitters: Look et al. 2004[18]

1.4 Growth and Treatment of zinc oxide - Background

1.4.1 Melt growth of single crystal bulk

When growing high quality bulk crystals the best results are obtained by growing from high purity melt. This method of growth requires a crucible in which to contain the melt as it cools. For zinc oxide, due to its high melting temperature (1975 ^{o}C) and high vapour pressure, finding a suitable crucible is problematic.
Skull melt is one means of working around the issue. In skull melt, also known as cold crucible, the melt is contained in a thin solid shell of the same composition as the growth material. However this growth method results in a large temperature gradient

from the shell (which must be kept cold and solid) through to the melt which must be kept hot and liquid. This large thermal gradient results in a higher concentration of dislocation defects and limits the maximum size of the crystals.

Recent advances have led to the development of iridium crucibles which are capable of withstanding the high melt temperature of ZnO under certain conditions of temperature, pressure and atmosphere.

By eliminating the need for a large temperature gradient between the crucible and the melt, larger crystals of higher quality can be grown, however the high cost of iridium crucibles remains a major obstacle to large scale and cost effective production.

Single crystals as large as 30 mm in diameter have been grown with X-ray rocking widths as low as 1 arc minute.

1.4.2 Hydrothermal growth of single crystal bulk

One method of overcoming the difficulty of growing single crystal bulk from a melt at 1975 ^{o}C is hydrothermal growth. In this growth regime zinc oxide is dissolved into a high pressure “mineraliser” solution, typically a mixture of KOH, LiOH and H_2O_2. A seed crystal is immersed in the solution and a thermal gradient is used to drive a convection current delivering ZnO enriched solution to the seeds. Each ZnO seed acts as a nucleation site for further growth. The growth rate is typically low, in the order of .1 mm per day, while contaminant H and Li incorporation into the crystal is high.

However despite these limitations extremely high quality single crystals have been grown with very low dislocation densities.

Production of 50 mm diameter boules is possible and X-ray rocking widths less than 45 arc seconds are possible[19]. This method of growth currently produces the highest quality crystals and will be the source for most of the bulk crystals studied in this thesis.

1.4.3 Growth of zinc oxide by Molecular Beam Epitaxy

Molecular beam epitaxy (MBE) is a method of growing epitaxial films first pioneered in the 1970’s[20]. Growth is carried out in an ultra high vacuum environment, which minimises the potential for contamination of films. Growth occurs when diffuse molecules or atoms from a material source (effusion cell) are directed at a substrate,

Figure 1-8. Interactions between the substrate and the incident atom result in an adatom with a given mobility. Growth occurs as adatoms present on the substrate surface begin to nucleate around energetically favourable sites and in energetically favourable configurations. Growth may be either two dimensional (true epitaxial growth) or three dimensional (island nucleation and cluster formation). Several in-situ methods of characterisation are available to facilitate observation of film growth as it occurs. Auger electron spectroscopy, scanning electron microscopy and reflection high energy electron diffraction (RHEED) allow for observation of growth mechanisms on an atomic scale. The disadvantages inherent in MBE growth include slow growth rate, low scalability and high cost.

Growth of zinc oxide by MBE was first reported in 1996[21] and since then has been performed using a number of different MBE techniques including plasma assisted MBE, electron cyclotron resonance-assisted MBE, metalorganic MBE and Laser assisted MBE.

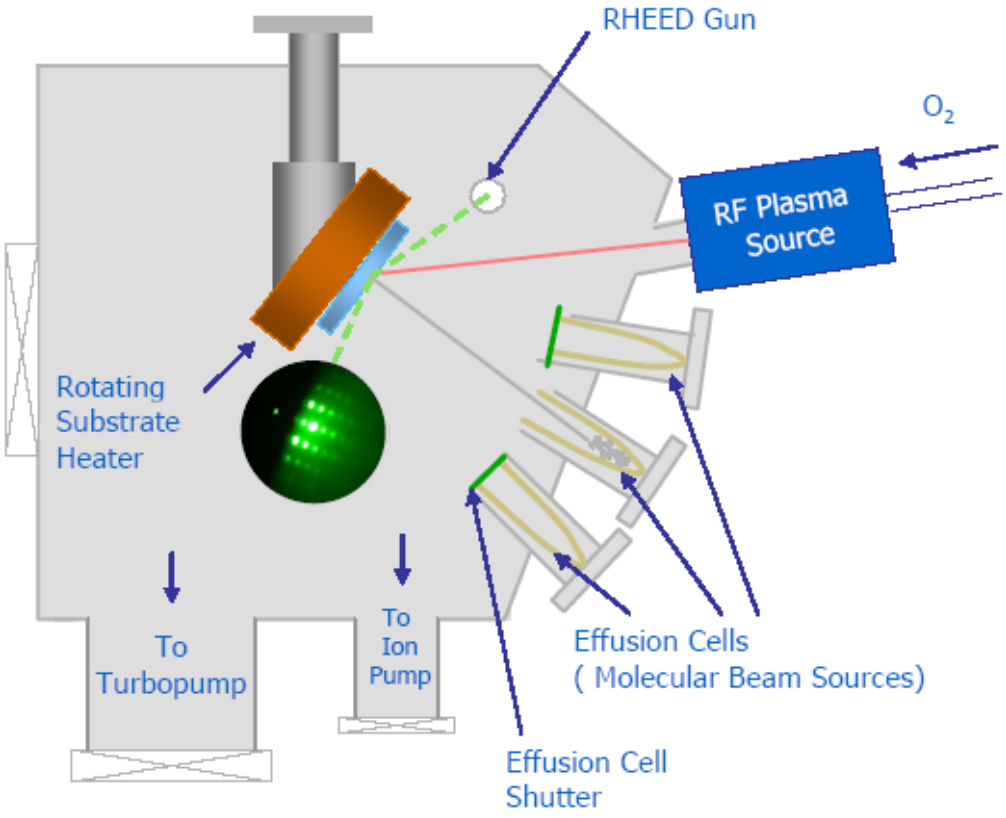

Figure 1-8 MBE growth chamber schematic

Due to the large role that the substrate plays in MBE growth, choosing a suitable material is important. In spite of the large mismatch sapphire, as seen in Figure 1-9, has been a popular substrate[21-27]. This is largely due to its low cost, transparency at visible wavelengths, excellent uniformity over large areas, and hexagonal lattice structure.

The disadvantage of using sapphire as a substrate is the high dislocation density and the mismatch induced strain that is incurred during growth.

The lattice mismatch can be reduced from 32% (tensile strain) when the a-axes of the Zn and Al lattices coincide, to 18% (compressive strain) by applying a rotation of 30^{o} or 90^{o} to allow the Zn and O lattices to coincide, see Figure 1-9. The two rotations give rise to crystal domains which can negatively impact the films electrical and optical properties.

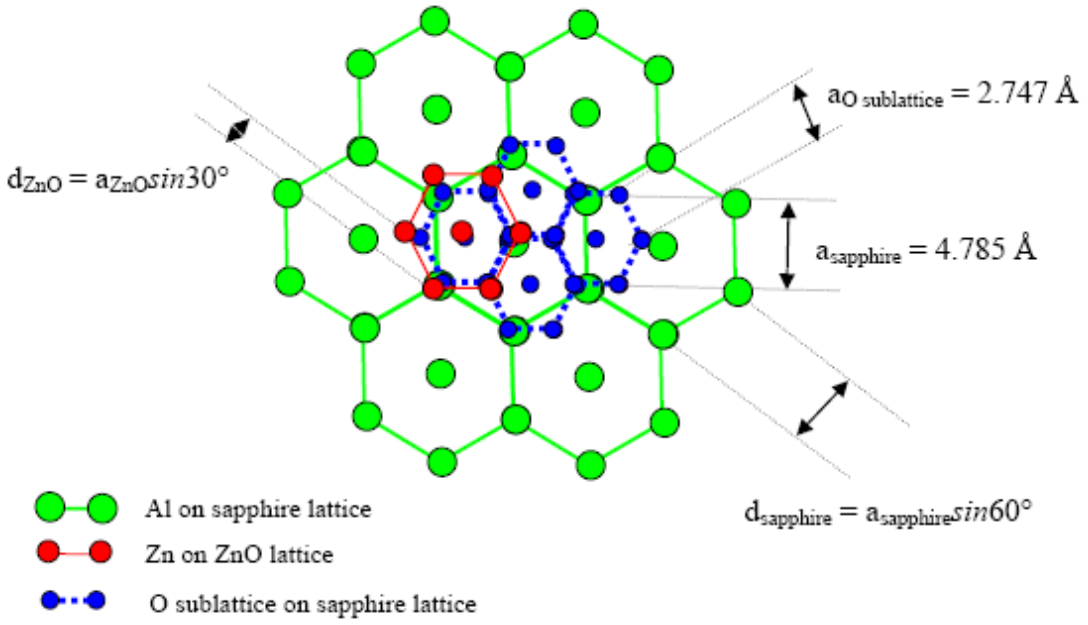

Figure 1-9 ZnO-Sapphire lattice mismatch

Recent publications on MBE growth have focused on the use of various buffer layers and alternative substrates in an attempt to mitigate substrate induced strain. These include MgO[28-30] and GaN[31-33] buffer layers (ironically the first MBE growth of ZnO was for use as a buffer layer for GaN), Pre-growth nitridation of the sapphire substrate and low temperature ZnO precursor buffer layers[34].

Other efforts include sapphire cleaved at an offset of 2.87^{o}[35] from the c-plane and growth on a-plane sapphire[36, 37].

Alternative substrates have been explored such as 6H-SiC[21, 38], GaAs[39], Silicon[34, 40], CaF_2, and more recently, single crystal bulk ZnO[41].

In order to grow stoichiometric films, atomic oxygen must be provided. Oxygen typically exists as a diatomic molecule, with a molecular bond sufficiently strong as to prevent dissociation by thermal cracking. This has lead to the introduction of several alternative methods for the provision of atomic oxygen. Radio frequency plasma assisted (radical source) MBE has been the preferred method, however electron cyclotron resonance and ozone sources have also been trialled producing results comparable to that of PAMBE[42].

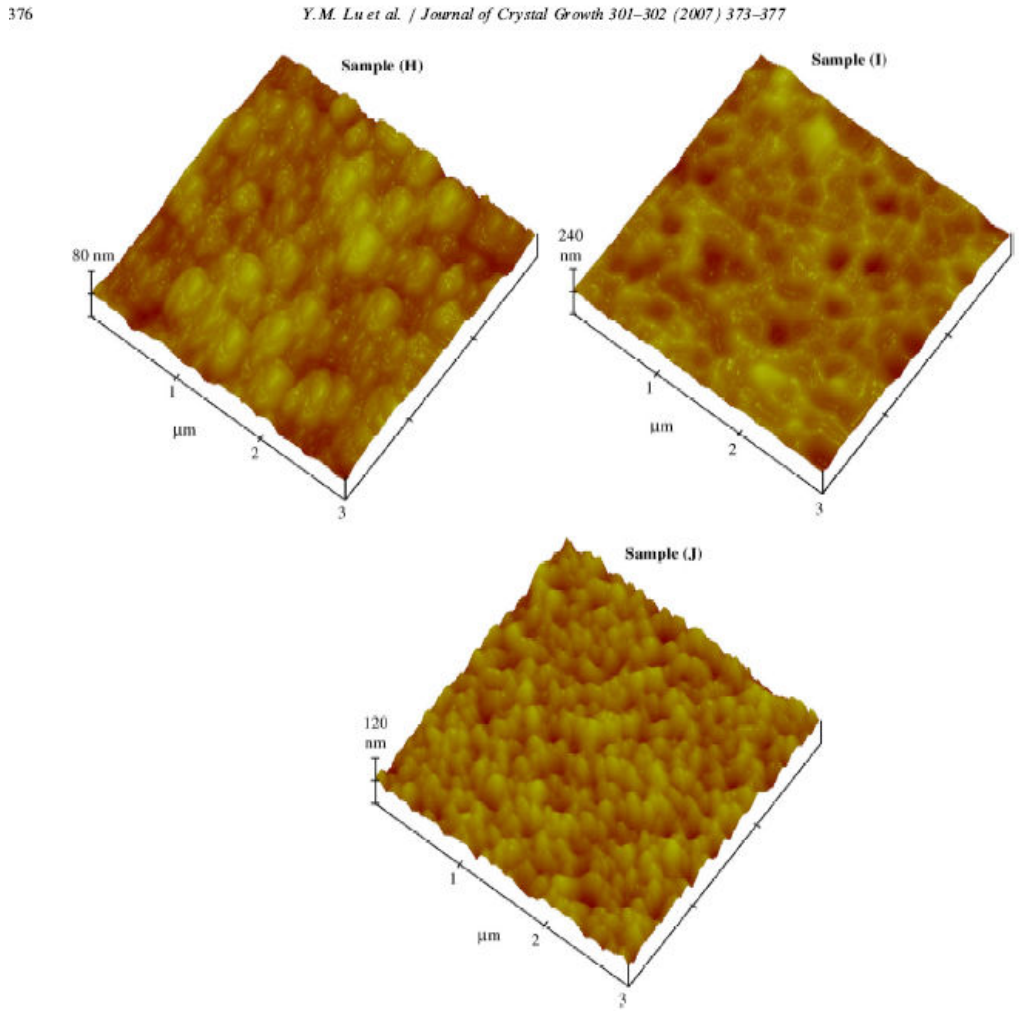

Figure 1-10 Dependence of film morphology on growth flux[34]

Figure 1-10 shows the surface morphology of a zinc rich, oxygen rich and stoichiometric films.

The quality of the film can also be influenced outside of the chamber conditions. Prior to growth, the substrate surface is usually prepared using a combination of chemical and thermal heating, additional treatment may include cleaning under a gentle flow of oxygen or argon gas, this has the effect of reducing surface particulates which may act as nucleation sites or film contaminants. To further improve film quality post growth annealing at higher temperatures is often utilised to improve the structural, optical and electrical properties.

MBE grown ZnO films can vary considerably in surface morphology, displaying columnar growth, hexagonal island formation, “brain” like structures, porous filaments and nano rods and electrical properties include carrier concentrations ranging from n = 10^{16} to 10^{20} cm^{-3} and mobilities up to $\mu = 260$ cm^2/Vs

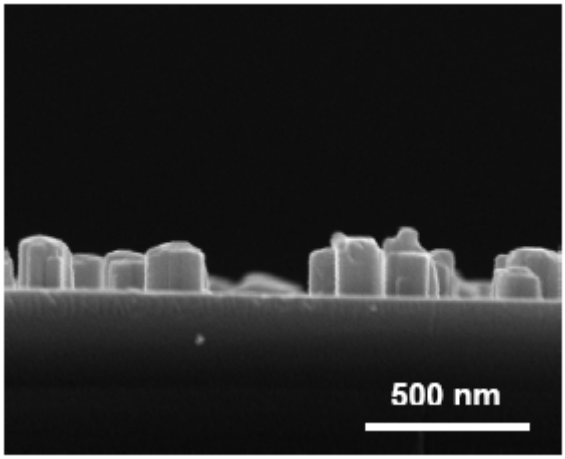

Figure 1-11 Columnar growth of MBE ZnO thin films - SEM
An example of commonly observed columnar growth in an MBE zinc oxide film grown locally is displayed in Figure 1-11.

1.4.4 Growth by DC and RF sputtering

Sputtering is a relatively cheap and quick method of thin film production that has the additional advantage of being largely scalable, areas of up to several square meters in a single deposition are feasible[43] with broad implications for applications such as transparent conducting layers on large scale solar arrays, something that cannot be achieved by alternative methods such as PLD or MBE.

Sputtered films typically display a high degree of polycrystallinity and surface roughness. They possess high resistivity and weak PL emission. All of these properties can be manipulated both during growth, and in post-growth treatment.

Before the production of piezo electric and optical devices can begin it is first important to determine the optimum conditions under which growth occurs. Zinc oxide films can be sputtered either from a metallic zinc film in a reactive oxygen atmosphere, or from a ZnO target (usually the result of pressed, sintered ZnO powder). The first method is performed by simple DC sputtering and can be enhanced further by using a magnetron configuration and a reactive oxygen atmosphere. The advantage of DC sputtering is the rapid growth rate and the ease of obtaining high purity zinc targets.

The second method, which makes use of a non conducting zinc oxide target, can only be effectively sputtered using the RF setup in which the anode-cathode arrangement of the substrate-target is rapidly swapped at a radio frequency of approximately 50k Hz to avoid charge build up and to maintain target discharge. Magnetic containment of the plasma near the target surface ensures a net transfer of material from the target to the substrate. This method improves stoichiometric growth by ensuring the correct concentrations of zinc and oxygen atoms in the growth chamber.

In this thesis films grown by both methods will be compared and contrasted in order to best determine the optimum growth conditions for both piezo-electric and optical properties.

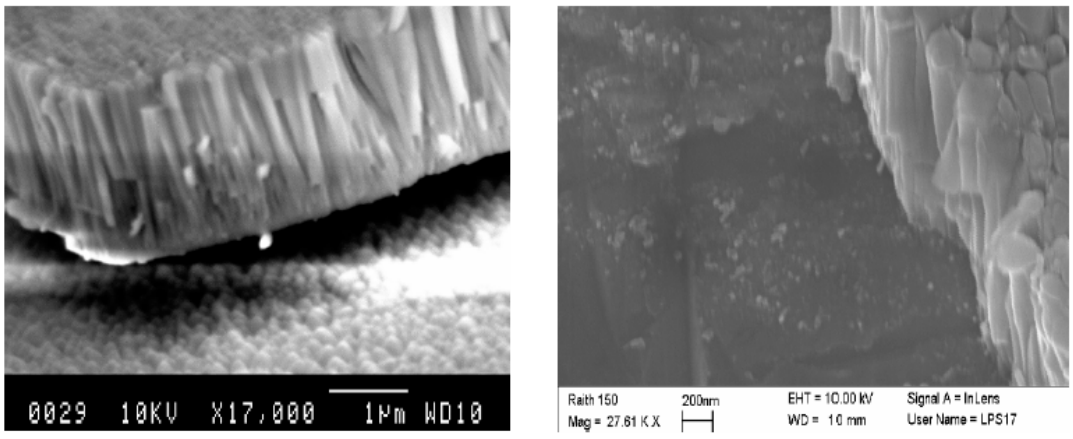

Figure 1-12 Columns combining to form films in sputtered ZnO thin films - SEM

Sputtered films typically display columnar growth as can be seen in the SEM images shown in Figure 1-12 of sputtered ZnO films grown locally by Leo Schuler[43]. Crystal alignment can vary depending on the substrate or growth conditions, though typically growth will occur with the c-axis aligned normal to the substrate surface.
The photoluminescence is typically dominated by a near band edge broad violet/UV emission between 3.2 and 3.3 eV which are assigned to excitonic transitions. The large line width is due to the lack of film homogeneity, itself a result of inhomogeneous strain and a high concentration of defects. Sputtered zinc oxide has characteristically high resistivity which is likely a result of the many domain boundaries inherent to a highly polycrystalline film. This high resistivity is a requirement for constructing piezo-electric devices and makes sputtered ZnO an excellent choice for SAW based devices.

Sputtered films are typically transparent which makes them an attractive choice for opto-electronic devices. The combination of piezo-electricity and optical transmission/emission open up a potentially useful range of opto-mechanical devices.

1.4.5 Reactive Ion Etching (RIE)

RIE is a technique for patterning and micro processing of thin films and substrates. Unlike wet etching, it produces no liquid waste. It is easily scalable and allows for a high degree of control over the etching process.

1.5 Characterisation techniques

1.5.1 Photoluminescence spectroscopy

Much of the attention devoted to zinc oxide relates to its optical luminescence. For this reason a reliable quantitative measurement of those optical properties is required. Photoluminescence spectroscopy is a non destructive method of indirectly observing the semiconductor band structure and quantifying the peak emission energies (which relates directly to the colour). It also provides a qualitative indication of crystal quality to compliment the picture provided by XRD.

In any given semiconductor, photons with an energy greater than that of the bandgap, may be used to excite electrons from the valence band into the mostly empty conduction band. In the case of photoluminescence (PL) a laser is the primary means of achieving this. Electrons in an excited state always seek to return to their lowest energy state, in this case the ground state is at the top of the valence band. The question of what happens to the energy lost when transitioning between the conduction band and the valence band, is answered in several parts. In semiconductors with a direct bandgap and few mid gap energy states, a favourable outcome is the production of a photon, where the energy of the photon corresponds to the bandgap of the semiconductor, however energy may also be lost through phonons (vibrations) in the lattice. In a perfect semiconductor, consisting of an infinitely homogenous and isotropic lattice, every emitted photon would exhibit the exact same characteristic energy and the PL

spectrum would consist of a single defined wavelength. However the introduction of localised deformations or stresses to the lattice, as well as the presence of point defects or foreign atoms will often serve to disrupt the homogeneity and isotropy of the crystal. This often results in either the introduction of new energy states that may fall within the forbidden energy range between the valence and the conduction band, or the creation of a broadened PL signature due to the macro scale laser sampling of nano/micro scale deformations in the lattice. In this way, a study of the PL spectrum can offer many insights into the nature of the material

Experimental procedure: The PL of a semiconductor is largely dependent on the temperature due to the thermal expansion/contraction of the lattice and changes in the electron-phonon interaction. For this reason PL measurements are typically made in a tightly temperature controlled regime.

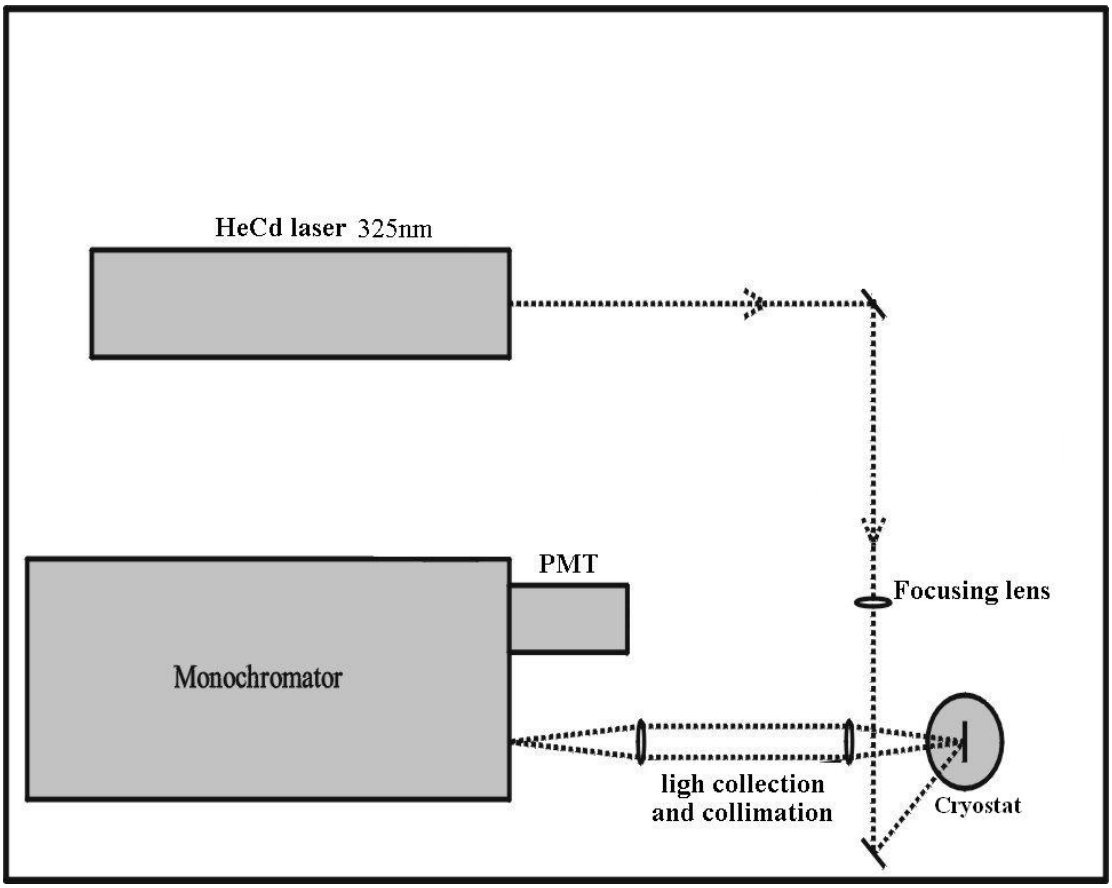

Figure 1-13 Experimental PL setup

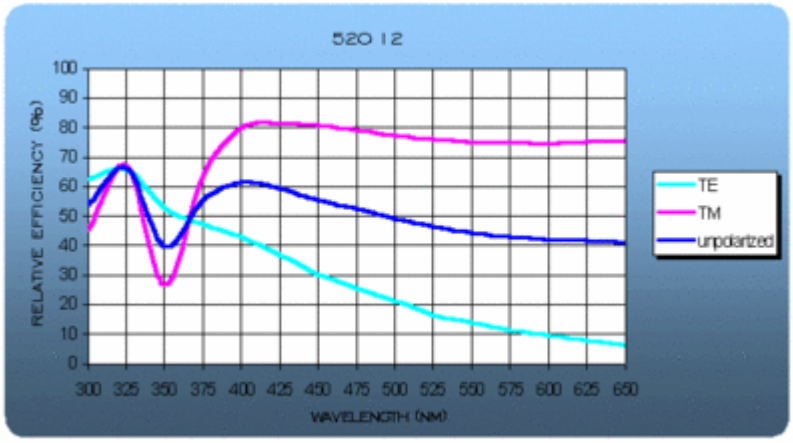

Figure 1-14 Spectrometer grating response curve

A 30 mW Kimmon Koha Co. 325 nm helium cadmium (HeCd) laser is focused on to a sample contained within the cryostat in a configuration illustrated in Figure 1-13. The sample is affixed to a copper finger cooled by liquid helium being passed over the back side. Heating is provided by an Oxford Instruments Intelligent Temperature Controller, and is stable to within 0.1 degrees Kelvin. The temperature can be controlled over the range 4-400 K.

The emitted PL is collected and collimated by a short focal length lens and then focused in to a spex1700 spectrometer by a longer focal length lens with an f-number matched to that of the spectrometer. The diffracted spectrum is scanned through by rotating the diffraction grating using a micro-stepper controller and the light intensity at each wavelength is integrated over a fixed timescale by a Research Inc photomultiplier tube (PMT) operating at 1800 V. For each wavelength, the integrated intensity is recorded in a spreadsheet for post acquisition analysis. The efficiency curve of the grating used for the high resolution bulk ZnO PL scans is show in Figure 1-14.

There are several parameters which can influence the photoluminescence. These include the temperature of the semiconductor sample, the excitation power and the excitation wavelength.

Photoluminescence is performed using excitation photons with an energy greater than that of the band gap. At these energies semiconductors are opaque and in the case of ZnO, using an excitation energy of 3.8 eV (HeCd laser), almost all of the laser energy is absorbed within the top 40 nm as has been shown by Jeong et al[44] in ellipsometry measurements. For this reason PL is regarded as a surface sensitive experiment as all excitation and photo emission occurs in the topmost volume of the film.

Characterising the effect of temperature on the PL can offer insights into the nature of the electronic bands and the transitions between them. The temperature dependence of the intensity can be used to establish "activation energies" for various transitions under circumstances where the emission intensities can be readily determined. Unfortunately for zinc oxide which has many overlapping transitions in a narrow energy range near the band edge, this technique is of limited use due to the difficulty in resolving individual peaks, most results obtained will be an average activation energy for a number of different transitions. Much work has also gone into quantifying the effect of temperature on the bandgap energy. In 1967 Varshni[45] established a now famous empirical fit for the behaviour of the bandgap across a range of temperatures

$$E(T) = E(0) - \frac{\alpha T^2}{\beta + T} \quad \text{(The Varshni fit)}$$

However in the last decade efforts have intensified to establish a relationship between the data fits, and the samples physical parameters, indicating a link between the temperature dependence of the band gap and the Debye temperature of the material.
It is also increasingly being noted[46] that the model is frequently applied in temperature domains to which it is not well suited, namely in the temperature range much less than the Debye temperature and to temperature sets <300K. This misuse of the model is being blamed for the wide variation in reported value for the parameters α and β.

A modified version has been proposed[47] to improve the numerical fitting

$$E(T) = E(0) - \frac{\alpha T^4}{(\beta + T)^3} \quad \text{(Fernandez model)}$$

However, while the numerical fitting was improved, the relationship has still proved to be unsatisfactory in providing a clear link between α the $T \longrightarrow \infty$ limit of the gap entropy and β with the Debye temperature or any other feature of the phonon energy spectrum.

A more fundamental model has been proposed by Manoogian and Woolley[48]

$$E(T) = E(0) + UT^{s} + V\Theta[\coth(\frac{\Theta}{2T}) - 1] \quad \text{(Manoogian model)}$$

The equation is composed of 3 parts (i) the T = 0K energy intercept, (ii) UT^{s} the lattice dilation, and (iii) the electron-phonon interaction. Due to the large number of parameters in the Manoogian model, a close fit to the measured data is easily attainable. However without being able to assign fixed values to at least two of the parameters, a wide range of values exist that still allow for a close fit to the data and the end result is a low chi-squared value but large uncertainties in the value of each. A theoretical calculation of the lattice dilation term U exists that should allow us to set reasonable limits on the values of the other parameters. For the case of $s \approx 1$ (linear expansion of the lattice with temperature) we can use the equation $U \approx 3B(\frac{\partial E_g}{\partial P})\langle \alpha_L \rangle$ to approximate U, where B is the bulk modulus, $\frac{\partial E_g}{\partial P}$ is the band gap coefficient of pressure and $\langle \alpha_L \rangle$ is the mean thermal expansion coefficient. The coefficient V is a measure of the rate of change of E_g with temperature $(\frac{dE_g}{dT})$ as $T \to \infty$. The remaining coefficient Θ is a measure of the effective phonon temperature. The usefulness of the coefficient Θ is that it can be related to the Debye temperature Θ_D by the simple ratio $\Theta_D = \frac{4}{3}\Theta$.[49, 50]

It will be shown later that using this method allows us to maintain a close fit to the data, yet place significant constraints on the uncertainty of the remaining coefficients.

The fourth and final model to be discussed in this thesis is a simplification of the manoogian model that ignores the influence of lattice dilation on the semiconductor band gap. It is simplified further by using the identity

$$\coth(\frac{x}{2}) - 1 = \frac{2}{e^{(x)} - 1}$$

Where $x = \frac{\Theta}{T}$ for the region $\frac{\Theta}{T} < \frac{1}{2}$

resulting in an equation of the form

$$E(T) = E(0) - \frac{\alpha\Theta}{e^{(\frac{\Theta}{T})} - 1} \qquad \text{(Bose-Einstein model)}$$

Which is equivalent to the Bose-Einstein model proposed by Vina et al[51].

In this case, $\alpha = \frac{1}{2}V$, where V is that of the Manoogian model and Θ is once again a measure of the effective phonon temperature, though in this model the effective temperature is supposedly related to the Debye temperature by $\Theta_D = \frac{3}{2}\Theta$.

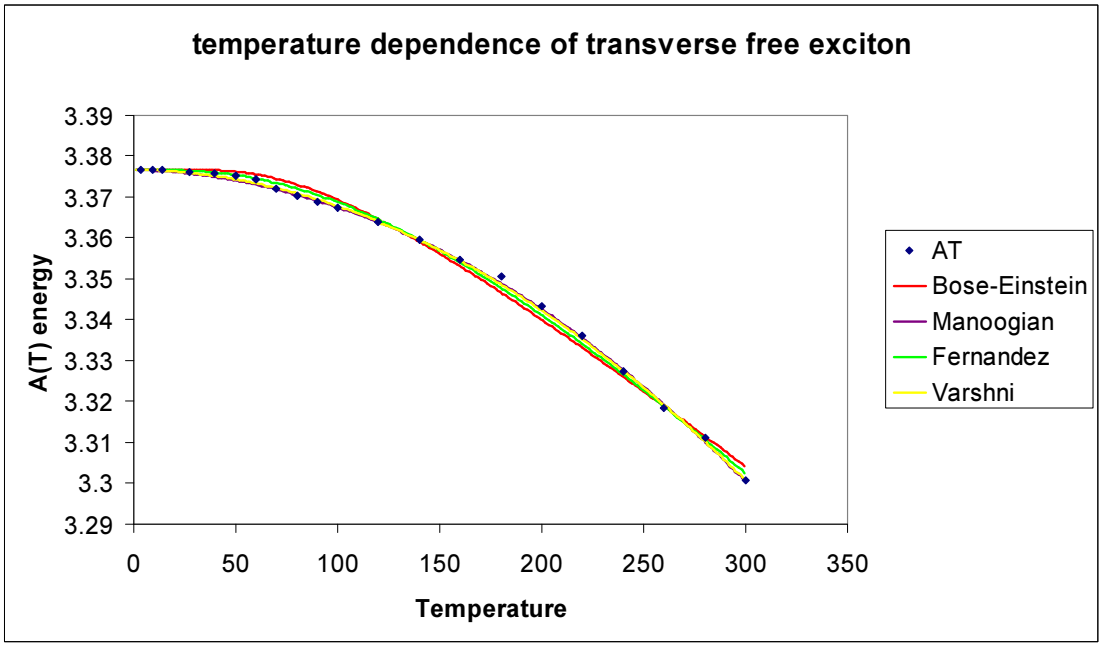

Figure 1-15 Comparing fitting methods

It has also been shown by Passler et al[46] that the Vaarshni model fails to provide satisfactory fits in the cryogenic region. While initial assessment by the author suggested that the Bose-Einstein model might prove superior than the previously listed models, due to either tighter constraints on the coefficients when performing a least squares fit, or a more clear link between the coefficients and the physical properties of the samples, subsequent familiarity with the Manoogian model has allowed for increasingly effective modelling of the collected data.

With the advent of modern computing, precise data fitting to the temperature dependence of the PL intensity is easily possible. The PL intensity can be modelled by the fit to the Arrhenius equation:

$$I(T) = \frac{I(0)}{1 + Ae^{-\frac{E_A}{kT}} + Be^{-\frac{E_B}{kT}} + \ldots}$$

Where the number of exponential terms on the denominator corresponds to the number of non radiative decay paths of the transition and the energy terms E_A, E_B etc correspond to the respective activation energies. For the simplest scenario only a single activation is required however empirical fits show significant improvements with a second decay term. Care must still be taken to ensure that the fits remain physically meaningful.

Prior to easy access to computing tools the activation could be obtained by determining the gradient of a ln(I) vs 1/T plot for the high temperature data. From this gradient the activation energy could be obtained, however this method is at best an approximation of the true value and will be used only as a measure of comparison in this thesis.

The power of the excitation laser influences the emission intensities and positions of the various near band edge PL features in different ways. Schmidt et al[52] produce an excellent model for the power dependence of the free excitons, donor and acceptor bound excitons, free to bound transitions and donor-acceptor pair transitions, all features common to the near band edge region. The transition intensity is shown to be governed by an $I \sim L^k$ law, where I is the intensity of the emission, L is the intensity of the excitation laser and k is a co-efficient. For free and bound excitons k is shown to be $1 < k < 2$ and for donor acceptor pairs is shown to be < 1.

1.5.2 Topography- SEM and AFM

Scanning electron microscopy (SEM) is a non contact, non destructive technique for imaging surface topography. In the primary mode "secondary electron imaging" an electron beam is rastered across the surface of the sample. The emission of secondary electrons produced by inelastic scattering of the incident electrons is detected. The image is formed from a two dimensional density distribution of detected electrons. This technique is useful for producing relatively quick qualitative impressions of the surface. The resolution of an SEM machine is typically in the order of 10 nm.

Atomic force microscopy (AFM) is another means of investigating the surface topography of a sample. In this type of the measurement a cantilever with a sharp tip is scanned across the surface. Monitoring a laser beam reflected from the tip of the cantilever will indicate deflections caused by interactions between the probe and the surface. This type of measurement is very useful for obtaining precise measurements of surface roughness and morphology. It has a resolution of better than 1 nm. One disadvantage of AFM scanning is the limited field of view. It is typically restricted to a few μm in height variation and a few hundred μm translation in the plane of the image, SEM on the other hand can scan images in the order of millimetres.

1.5.3 Crystallography –X-ray diffraction analysis

As has previously been discussed, much of semiconductor theory is based on the assumption of an infinite homogeneous periodic crystal lattice. The "quality" of a semiconductor crystal or film is determined by how closely it conforms to this ideal. A qualitative measurement of this can be obtained by X-ray diffraction measurements (XRD). In the analysis of a thin film a monochromatic X-ray beam is directed at the sample and a detector is placed at the opposite angle of incidence. Altering the angle of incidence and measuring the reflected intensity results in angles of peak reflection intensity that can then be used to form the diffraction pattern.

Braggs law for an EM wave incident on a lattice states

$$n\lambda = 2d\sin\theta$$

Where n is the order of refraction, λ is the wavelength of the incident X-rays, d is the spacing between atomic planes in the lattice and θ is the angle of incidence.

A plot of the diffraction pattern for a crystal as a function of the incident angle will result in a spectrum characteristic of the crystal structure. The angular position of the peaks will give an indication of the lattice parameters while the width (rocking curve) of the peaks will give an indication of the uniformity of the crystal, where the width of the peak is roughly proportional to the defect density. A change in the lattice parameter from that expected usually indicates either compressive or tensile strain in the crystal.

1.5.4 Stoichiometry –Rutherford backscattering

Rutherford backscattering spectroscopy (RBS), otherwise known as High-energy ion scattering (HEIS) is a tool for determining the elemental composition of a material.
A beam of high energy ions (usually He^{++}, 1 MeV) is directed at the sample and a measurement of the angular and energy distribution of back scattered ions is made.
The detection is performed by an array of silicon surface barrier detectors. A detector element is composed of a contacted p-n junction. A high energy ion passing through the detector element generates a trail of electron-hole pairs. The internal electric field generated by the p-n junction separates them and produces a current. The size of the current is proportional to the energy of the incident ion and the placement of the element relative to the incident ion beam determines the angle. By this method the energy and angular distributions of the back scattered ions can be quantified and compared to the profiles of known target atoms, from which the stoichiometry can be determined.

1.5.5 Electrical properties – Hall measurements

Electrical characterisation of the samples is carried out by Hall effect measurements. This experimental technique makes use of the effect of a magnetic field on a moving charge (Lorentz force). It is capable of determining the carrier type (p or n), carrier concentration, mobility, and resistivity of the sample. Ohmic contacts were arranged according to the Van der Pauw geometry. Care must be taken to ensure that thin films are electrically isolated by growing on an insulating substrate to avoid mixed results.

1.5.6 Experimental consideration – post growth annealing

Post growth annealing of the films in annealing experiments is carried out in one of 3 quartz tubes capable of generating and maintaining a temperature up to 1200 ^{o}C. The tubes can be supplied with a selection of atmospheres which include oxygen, nitrogen, hydrogen, as well as vacuum.

Particular substrate types proved prone to cracking during and after annealing, care was taken during removal from the furnace to minimise sample damage. Cooling typically took several hours and in select cases samples were left to cool overnight.

2 The optical investigation and characterisation of bulk zinc oxide

The typical application of a new semiconductor usually involves thin films of epitaxial material, however the vast number of growth methods and growth parameters contribute to a bewildering array of properties and characteristics. In this chapter the photoluminescence of bulk zinc oxide is studied in detail with the intention of gaining a fuller understanding of this important material in order to better interpret the results obtained in the future from high quality thin films.

This chapter will also deal with the identification and cataloguing of the near band-edge and deep level transitions and attempt a reconciliation between the various competing models of several different research groups. The results will be compared and contrasted with each other, and with results obtained locally.

2.1 Near band edge photoluminescence

The PL spectrum of the near band edge (NBE) region in high quality bulk samples is typified by a combination of free excitons, donor bound excitons and their two electron satellites, along with the LO phonon modes of these transitions. The nature of these peaks has been a subject of much controversy over the last several decades and still remains an area of contention between research groups. The measured energies of several supposedly identical peaks can vary markedly from researcher to researcher, this ambiguity is both a source of frustration and constant revelation.

Care will be taken to outline the methodology by which measurements will be made with a precision of better than 0.5 meV across the range of the near band edge PL and better than 0.3 meV across the neutral bound exciton subsection. Maintaining high precision is paramount in producing a meaningful catalogue of emission peaks whose line widths are often <1.0 meV.

2.1.1 Calibration of the spectrometer in the near band edge region

Any accurate identification of the numerous transitions near the band edge first requires a detailed characterization of the precision of the equipment to be used in the acquisition of data. A Spex1700 monochrometer fitted with a 1200 mm/l grating was used to affect the diffraction of the PL emission for data collection. The spectrometer has a minimum step size of 0.001 nm and spectral range from 0-750 nm when using a 1200 mm/l grating. The PL emission was detected using a water cooled photomultiplier tube. The performance of the spectrometer in the NBE region can be seen in Figure 2-1

The black vertical lines represent known atomic transitions of the three elements used for calibration purposes. The coloured lines represent the measured spectral emissions of the three calibration lamps used for the purpose. There is a clear discrepancy between the observed emissions peaks and the expected values. However applying a small constant correction factor of -0.232 nm to the wavelengths of the observed peaks shows an excellent agreement between the measured and expected transitions, as seen in Figure 2-2. The application of such a calibration offset is routine in spectroscopy and the value often has to change due to laboratory environmental factors, mainly temperature.

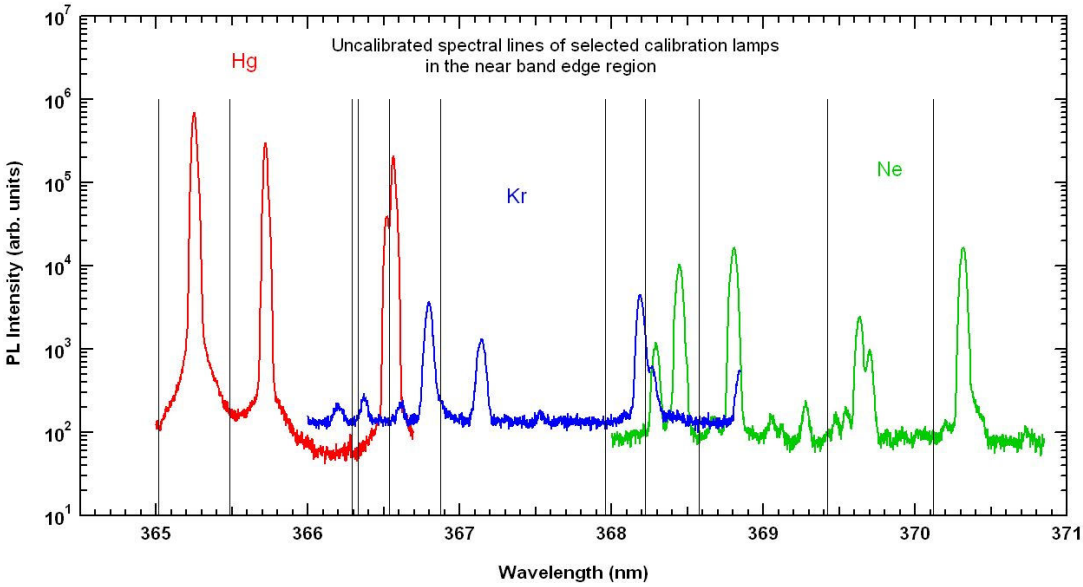

Figure 2-1 High resolution spectrometer scan pre-calibration

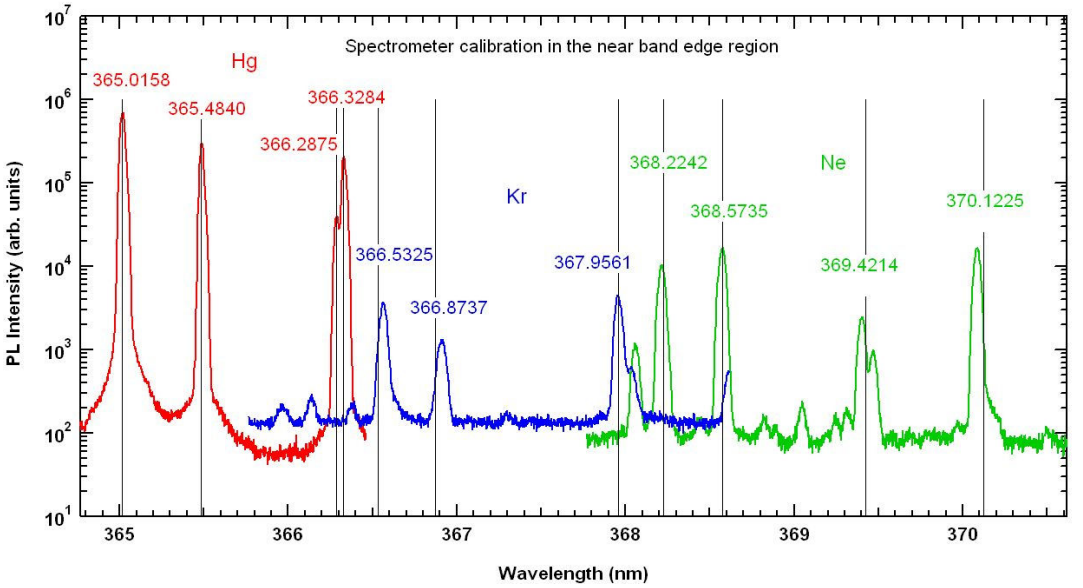

Figure 2-2 High resolution spectrometer scan post-calibration

In Figure 2-3 we see the measured separation ($\Delta\lambda$) between the calibrated emission lines and their accepted literature values. The fitted line (in red) indicates that a component of the spectrometers miscalibration is wavelength dependent. However over the range of the region in which the narrowest emission lines are observed this does not exceed 0.03 nm (0.3 meV at this wavelength) and this shall be used as a lower limit on

the certainty of the measurements made as it represents a fundamental limit of the experimental equipment.

It is also important to note that over the region of prime interest (368 – 370 nm) the spectrometer offers an excellent degree of uniformity which provides cause for a good degree of confidence in the accuracy of measurements made over this region.

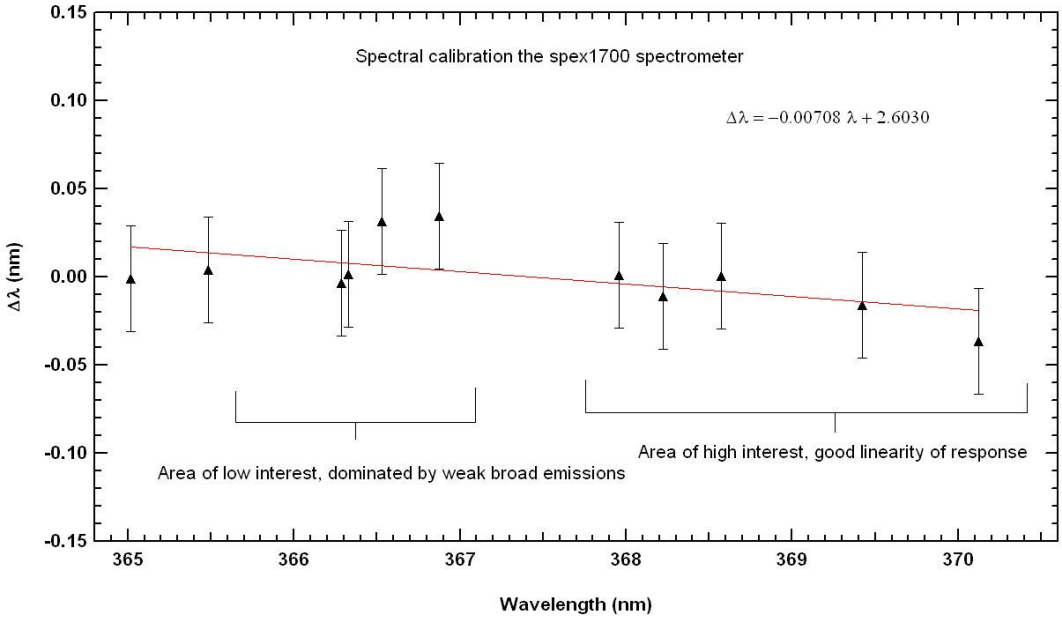

Figure 2-3 Spectrometer variance across region of interest

Another important aspect in determining the reliability of a measurement is the ability of the spectrometer to accurately reproduce the same range of mechanical motion for two separate measurements with the same scanning parameters. It can be observed in Figure 2-4 that the mechanical reliability of the spectrometer is in the order of ±0.1 meV for each scan. Therefore in conclusion we are able to claim an absolute accuracy of ±0.4 meV for line positions and an accuracy of 0.03 meV for line separation.

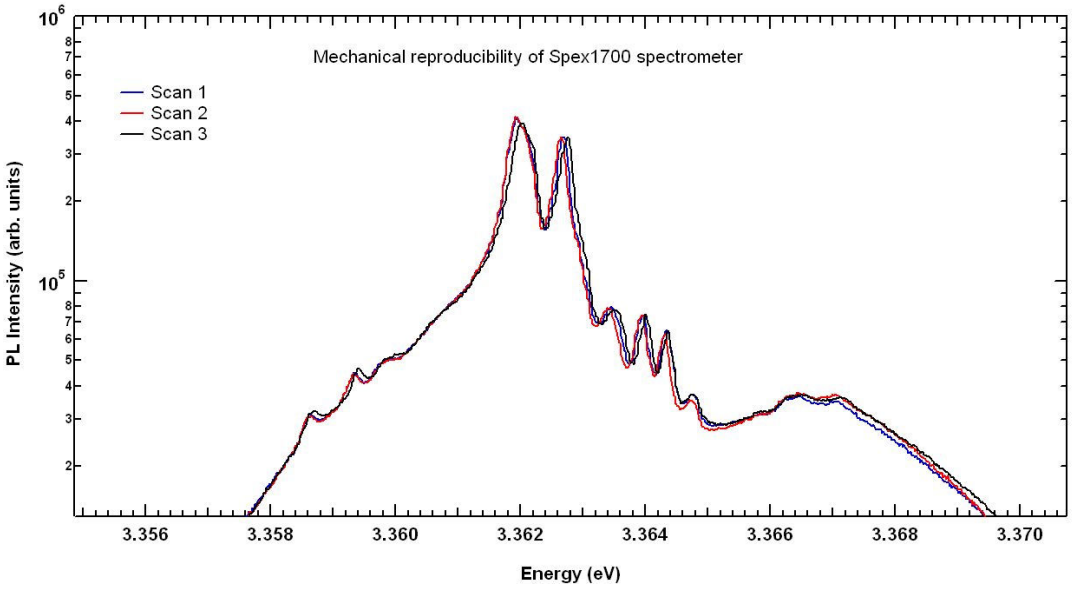

Figure 2-4 Mechanical reproducibility of Spex1700 spectrometer

2.1.2 Free excitons

As discussed previously, the valence band of wurtzite zinc oxide is split into three bands (A, B, C) through spin orbit and crystal field interactions. Although a better study of these bands can be obtained through reflection and transmission experiments, it is still possible to observe several of the features by their photoluminescence. Figure 2-5 shows the region of the spectrum in which some of these excitons can be observed.

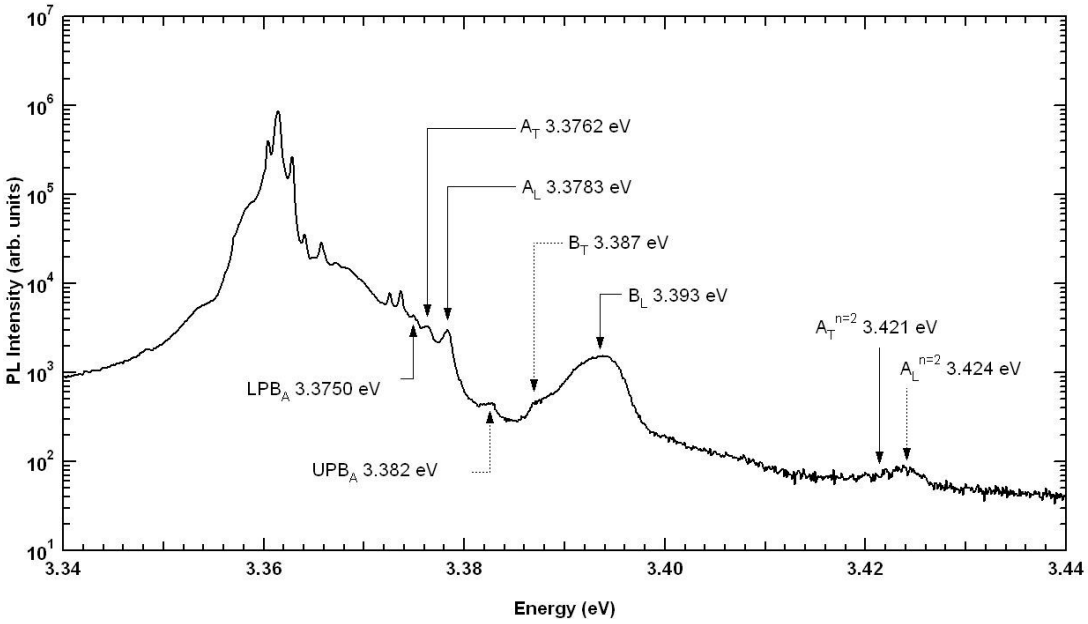

Figure 2-5 Band edge 4K PL – free exciton features

Temperature dependent PL measurements were performed to identify the free exciton A_T and A_L lines whose luminescence comes to dominate the PL spectrum as the temperature is increased. Once the free exciton peaks have been identified, calibration can be verified to reasonable degree by comparing to transition energies listed in published literature. Excitonic transitions for the A and B bands are clearly visible as well as the $A_{n=2}$ recombination for the exciton in its first excited state. Although this transition has an energy similar to that of the $C_{n=1}$ transition the C exciton is not thought to observable in the experimental configuration used, with the excitation source electric field vector perpendicular to the C-axis. Observing the C exciton would require a configuration with the E-vector of the polarised laser lying parallel to the C-axis. The longitudinal-transverse splitting $\hbar\omega_{LT}$ of the excitons is a measure of the exciton oscillator strength (*f*) by the relation[53]

$$\hbar\omega_{LT} = (2\pi/\varepsilon)(\hbar e^2/m_0\omega_0)(f/V)$$

where ε is the dielectric constant, m_0 is the free electron mass, V is the volume of the semiconductor and ω_0 is the exciton resonance frequency.

Table 2-1 shows accumulated data for the free excitons observed in reflection and PL experiments[9-11, 49, 54-61]. The spread in data is the result of several factors including sample to sample variation, miscalibration of the experimental data and misidentification of peaks. Additionally the peaks are sensitive to both the polarisation of the excitation source and the polarisation sensitivity of the spectrometer which partially explains the observance of peaks in some experimental configurations and not others.

		Miller*	Meyer	Reynolds	Chichibu	Hummer	Lagois	Zamfirescu	Collins	Teke	Hamby	Syrbu
	LPB	3.375		3.3743	3.3768					3.374	3.374	
	UPB	3.382		3.3829	3.3783					3.381		
n=1	AT	3.3762	3.3759	3.3775		3.3768	3.3758	3.776	3.3773	3.3757		3.3747
	AL	3.3783	3.3772	3.3793	3.378		3.3776		3.3783	3.3771	3.378	3.3765
n=2	AT	3.421		2.409		3.4227			3.4221	3.4202		3.4234
	AL	3.424		3.4221						3.422		
n=3	AT					3.4309			3.4303			
	AL											
n=1	BT	3.387			3.386	3.3834	3.381	3.3856	3.3838	3.3898	3.385	3.3834
	BL	3.393					3.3912					3.3925
n=2	BT					3.4276		3.429	3.4288			3.429
	BL											
n=3	BT					3.4359						
	BL											
n=1	CT				3.4214	3.4223	3.4198	3.422	3.422			
	CL						3.4317		3.4335			
n=2	CT				3.4679	3.4664			3.47			
	CL											

Table 2-1 Exciton peak energies (eV) in single crystal ZnO

2.1.3 Bound Excitons

The neutral bound exciton region of the PL spectrum offers the greatest amount of information about the nature of the shallow carriers and acceptors, with radiative pathways, within the semi-conductor. Although the PL from high quality bulk crystals should, in theory, be nearly identical, there still remains little consensus as to the identification of the various transitions frequently observed. This section will attempt to reconcile the two main competing models for the donor bound exciton region.

An extensive listing of near band emissions and their energies is provided by Meyer et al[9]

Table 2 Free and bound exciton recombinations and related properties.

line	wavelength (nm)	energy (eV)	localisation energy (meV)	two-electron-satellite separation ($2P_{xy} - 1S$) (meV)	donor binding energy (meV)	chemical identity
A_L*	367.12	3.3772				
A_T*	367.26	3.3759				
I_0	367.63	3.3725	3.4			
I_1	367.71	3.3718	4.1			
I_{1a}	368.13	3.3679	8.0			
I_2**	368.19	3.3674	8.5			
I_3**	368.29	3.3665	9.4			
I_{3a}	368.34	3.3660	9.9			
I_4	368.34	3.3628	13.1	34.1	46.1	H
I_5	368.86	3.3614	14.5			
I_6	368.92	3.3608	15.1	38.8	51.55	Al
I_{6a}	368.96	3.3604	15.5	40.4	53	
I_7	369.01	3.3600	15.9			
I_8	369.03	3.3598	16.1	42.1	54.6	Ga
I_{8a}	369.08	3.3593	16.6			
I_9	369.37	3.3567	19.2	50.6	63.2	In
I_{10}	369.76	3.3531	22.8	60.2	72.6	
I_{11}	370.28	3.3484	27.5			

* A_L and A_T are the longitudinal and transversal free A-exciton states. A_T is the reference for the determination of the bound excition localisation energy.
** I_2 and I_3 are assigned to ionised donor bound exciton recombinations.

Table 2-2 Extract from Meyer paper on band edge PL[9]

An attempt was made to correlate the published transitions with the spectra of bulk zinc oxide samples studied in this thesis.

Although the free A excitons were easily identified from the temperature dependent measurements, the splitting of the A_T and A_L lines clearly did not match that observed by Meyer et al (2.2 versus 1.3 meV for Meyer)[9]. Further measurements of various

other bulk samples showed a wide variation in exciton splitting, ranging from 1.3 to 2.3 meV.

By taking the transitions listed in Table 2-2 and overlaying them on a typical PL spectrum obtained locally, it should be possible to find a degree of similarity between the two. In Figure 2-6 this task is performed. Several of the reference lines listed by Meyer can be shown to overlap neatly with the observed emission spectra of melt grown Cermet Inc bulk, if a small constant shift is allowed. This includes the A_L line which has been identified through temperature dependent experiments, as well as the dominant neutral bound excitons which provide a good fit for the bound exciton lines I_5, I_7 and I_{8a}.

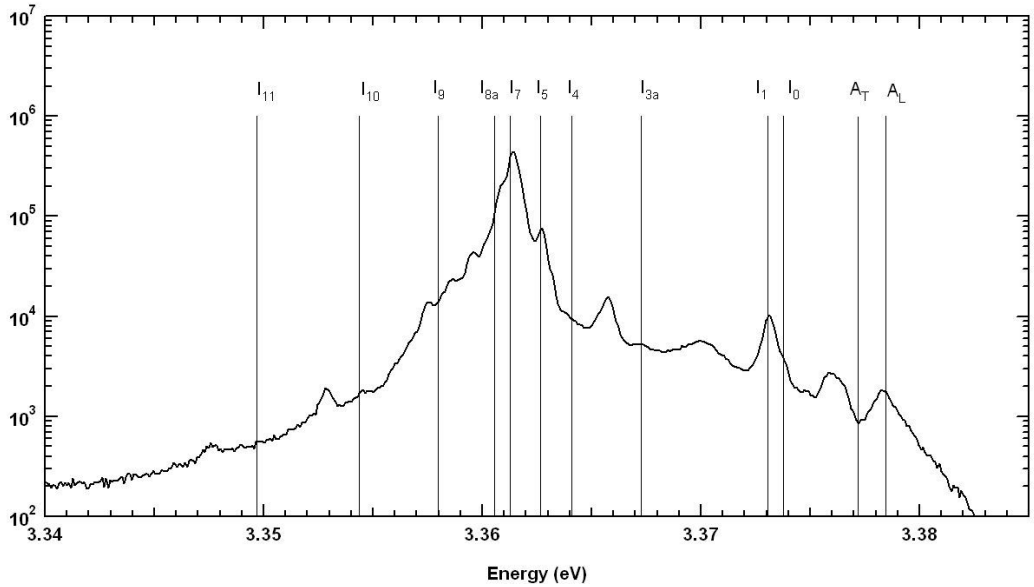

Figure 2-6 Bulk DBE – identification trials -1 - Meyer

However, as can also be observed in Figure 2-7, by applying a slightly different offset another good fit can be obtained for the same dominant bound exciton peaks, this time for I_4, I_5 and I_6, in addition to this a good match can be shown for the free exciton peak A_T.

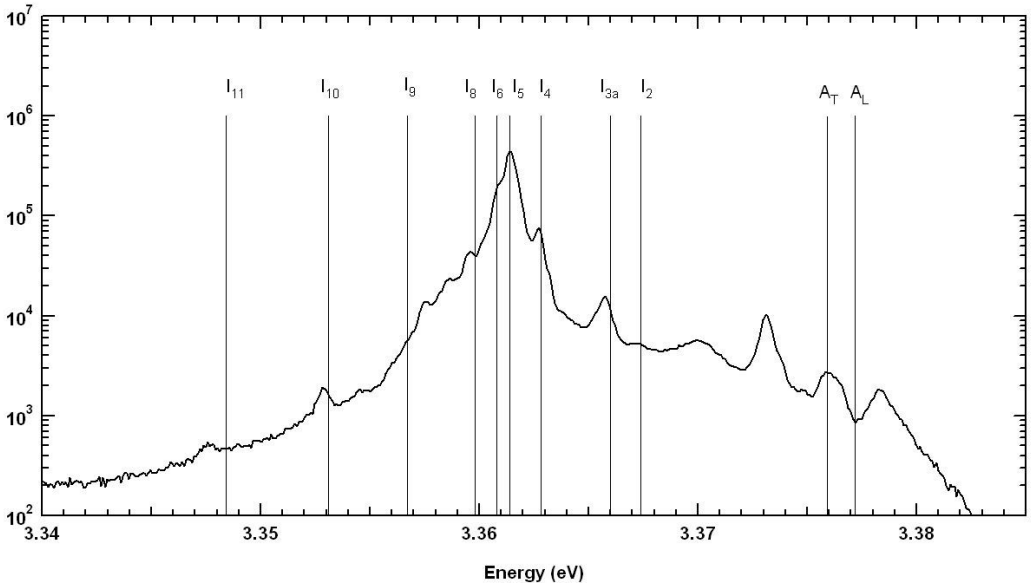

Figure 2-7 Bulk DBE – Identification trials – 2 - Meyer

To further complicate the issue, the neutral donor bound exciton peaks labelled I_5-I_8 all share similar bindings energies and cannot be resolved separately in temperature dependent PL experiments. Given that the difference between the two shifts is potentially less than the minimum experimental error it is important to identify which assignment best matches the data in order for future discussions to be consistent and meaningful.

Using Meyers definition of the localisation energy of each peak as its energy spacing from the A_T free exciton we can measure the localisation energies for the three dominant bound exciton peaks.

		localisation energy (meV)		
peak	peak energy (eV)	Miller	peak	Meyer
peak 1	3.3627	13.2	I4	13.1
peak 2	3.3614	14.5	I5	14.5
peak 3	3.3608	15.1	I6	15.1

Table 2-3 Identification of DBE – observed PL compared with literature

Cross referencing the measured localisation energy obtained from the spectrum with those obtained from Meyer we can clearly show good agreement with peaks I_4, I_5 and I_6 to within 0.1 meV which is within the measurable reproducibility of the second proposed model.

Concerns that the measurement of localisation energy may be arbitrarily dependent on whether A_L or A_T is used as the point of reference can be addressed by comparing two PL spectra with different splittings between A_L and A_T, which has been done in Figure 2-8.

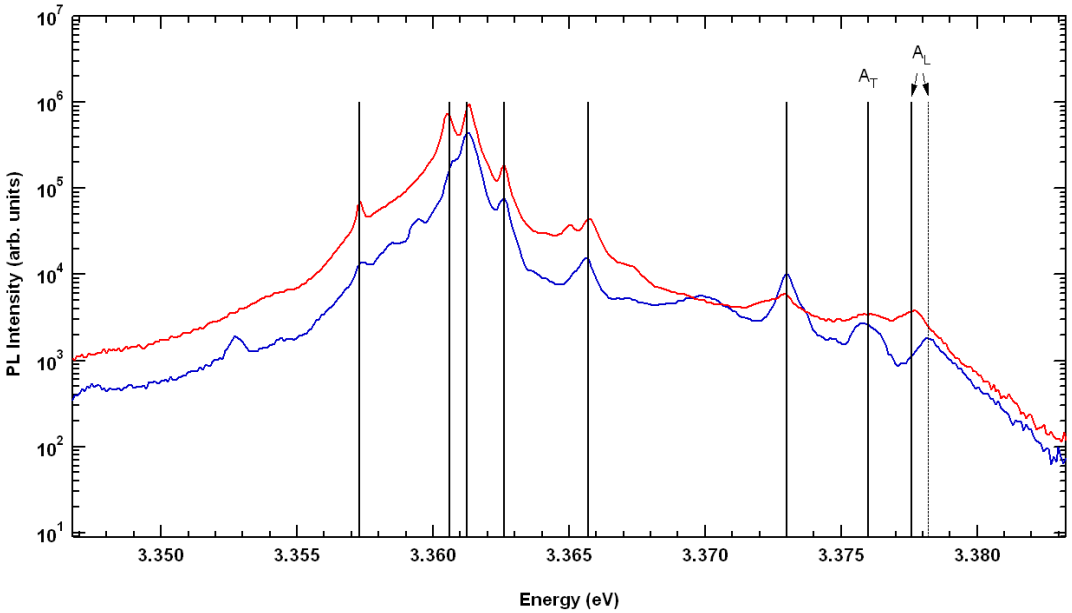

Figure 2-8 Variance in free exciton splitting – 4K PL

As can be observed, the dominant neutral bound excitons are common to both, but the A_L and A_T splitting shows an appreciable difference, it is demonstrated that the localisation energies of the neutral bound excitons are common to the A_T exciton and not the A_L exciton. By this reasoning, the identification of the dominant neutral bound excitons in both the melt grown Cermet Inc and the hydrothermally grown Tokyo Denpa samples used in this thesis can be confidently assigned to the peaks I_4, I_5 and I_6. The difference in position of the A_L emission relative to the rest of the spectrum is the result in variations in the material characteristics of the film which vary somewhat between material growths.

Teke et al[11] have favoured a more descriptive labelling scheme. Neutral acceptor bound excitons are labelled A^0X, neutral donor bound excitons as D^0X and rotator states as R. Each label is further identified by an appropriate subscript to distinguish A exciton transitions from B exciton transitions.

PL measurements of bulk samples produced by Cermet Inc have been performed in this thesis and also by Teke, making correlation of the observed peaks to the assigned labels easy. In Figure 2-9 the labels assigned by Teke have been over-layed with the observed emission spectra of Cermet Inc bulk ZnO crystal, although a small constant offset correction has been applied to account for experimental calibration.

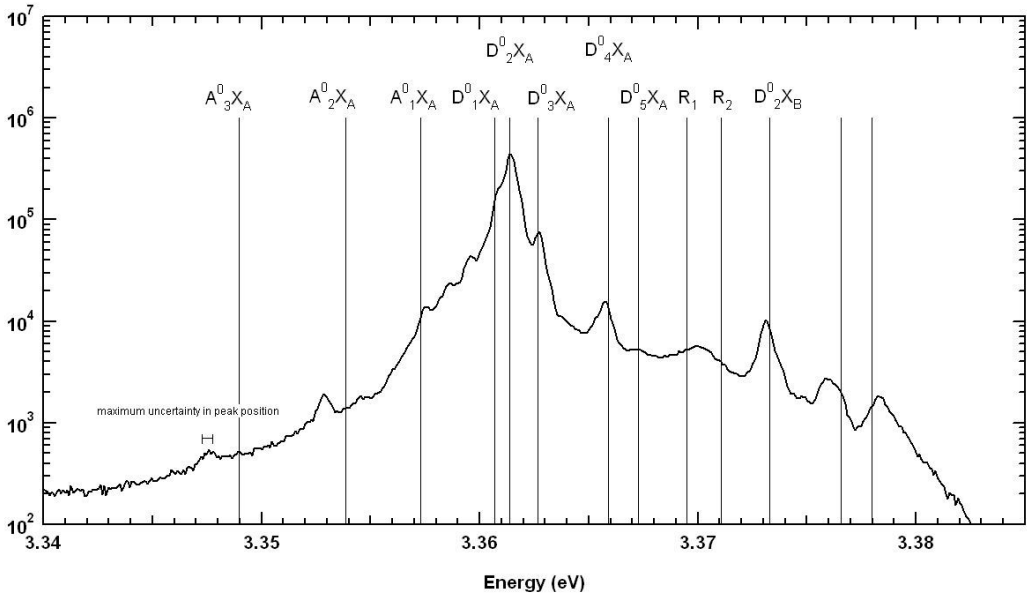

Figure 2-9 – Alternative DBE labelling system - Teke

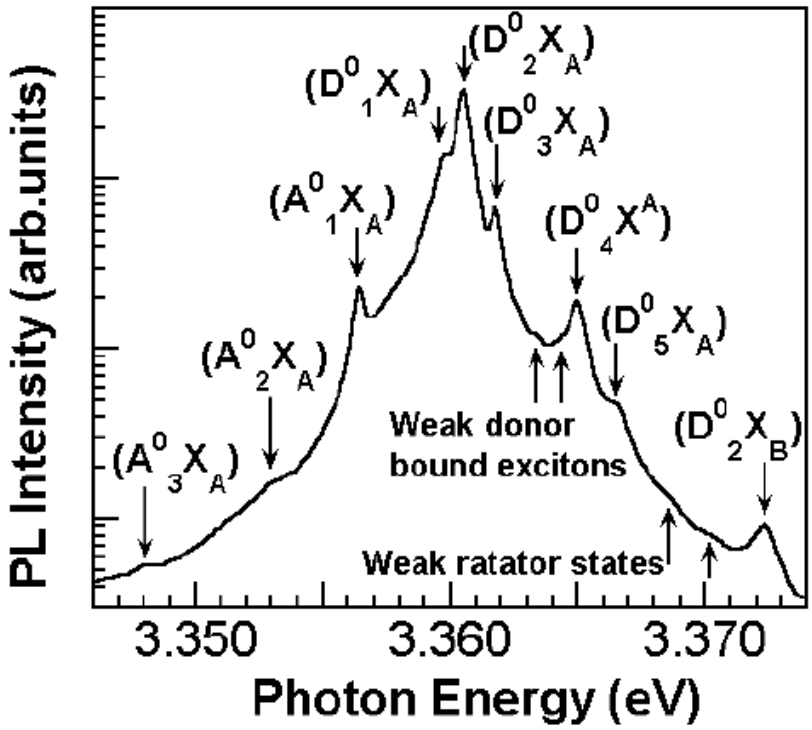

Figure 2-10 Extract from Teke paper on DBE

When comparing Figure 2-9 and Figure 2-10 (Teke), clear similarities in the lineshape can be observed.

Having assigned labels from both identification regimes to many of the observed transitions it is now possible to reconcile the identities of several of the important features of the PL. By doing this we can establish any clear discrepancies either in the calibration of the scans or in the emission energies of the various bulk samples.

Teke	$FX_A(\Gamma_5)$	$FX_A(\Gamma_6)$	$D^0{}_2X_B$		$D^0{}_5X_A$		$D^0{}_4X_A$	$D^0{}_3X_A$	$D^0{}_2X_A$	$D^0{}_1X_A$		$A^0{}_1X_A$	$A^0{}_2X_A$	$A^0{}_3X_A$
Meyer	A_L	A_T	I_0	I_1	I_2	I_3	I_{3a}	I_4	I_5	I_6	I_7	I_8	I_9	I_{10}
										I_{6a}		I_{8a}		

Table 2-4 Correlating peak two identification systems

Table 2-4 shows the correlation between the two labelling schemes used by Teke and Meyer, as can best be determined via calibration and spectral comparisons.

Debate still exists over the accuracy and interpretation of the experimental data used to assign emissions to a specific transition type, however cross referencing between literature papers should now be possible.

2.1.4 Violet region

The PL emission spectrum in the region between 3.30 eV and 3.34 eV is dominated by two features. In all high quality bulk samples the two electron satellite of the neutral donor bound excitons can be observed. In a two electron satellite transition, a donor bound exciton recombines, and in the process excites the valence electron of the donor atom into the first excited state (2s, 2p). This excitation robs the emitted photon of part of its energy, resulting in a red shifted emission peak. The amount by which the energy has been reduced is the difference in energy between the 1s and 2p states of the donor which is ¾ of the donor binding energy (using the hydrogenic effective mass approach) and can be used as a quantitative measure of the binding energies of the various donors.

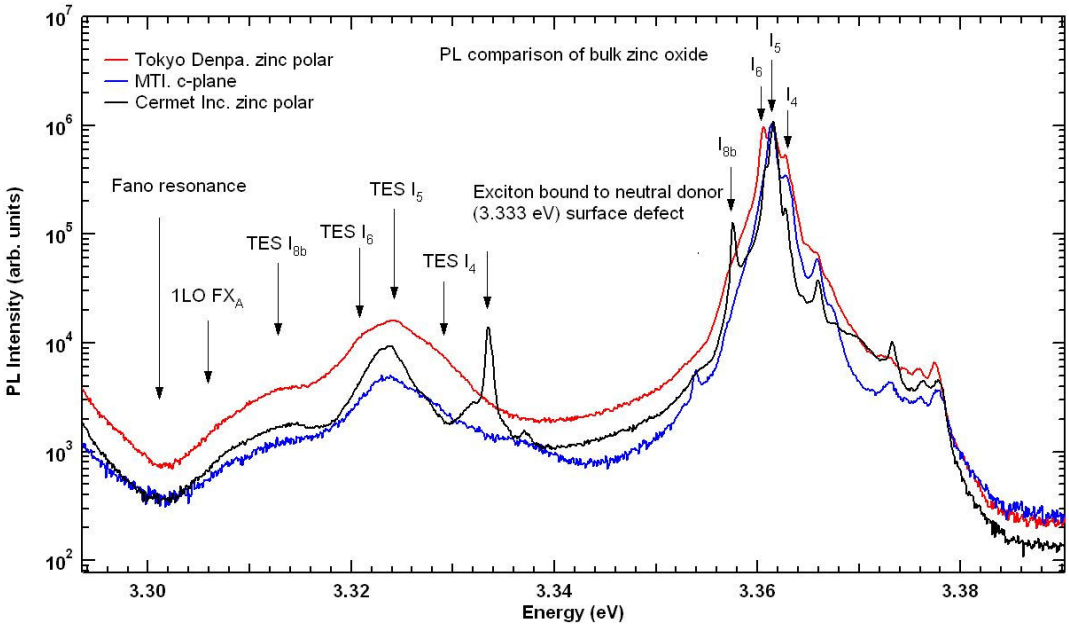

Figure 2-11 NBE – TES region – 4K PL

The sharp emission peak at 3.333 eV has been shown to display bound exciton responses to temperature change similar to the neutral donor bound excitons[9]. Cathodoluminescence has further shown the peak to be strongly associated with surface defects and grain boundaries[62]. The peak is prominent in all Cermet melt growth ZnO crystals, and in hydrothermally grown Tokyo Denpa crystals which have been annealed in oxygen at temperatures about 800 degrees C. The two electron satellites for the

dominant neutral donor bound excitons can be observed and have been labelled as TES I_n, the possible TES of I_8 is also labelled and shall be investigated further on the following page.

Common to all high quality bulk films and to some thin films is what appears to be an absorption dip around 3.30 eV. The line shape is suggestive of Fano resonance. A scenario in which a discrete energy level couples with a continuous background causing a reduction in the peak intensity and a characteristic dip on either the high or low energy side of the transition. In this particular case the coupling is between the first LO phonon of the D^0X and an unknown continuous background, which may be the result of a tail in the density of states from the bandedge. The nature of the Fano coupling in ZnO was confirmed by Xu et al. in 2005[63] and discussed further in 2007[64].

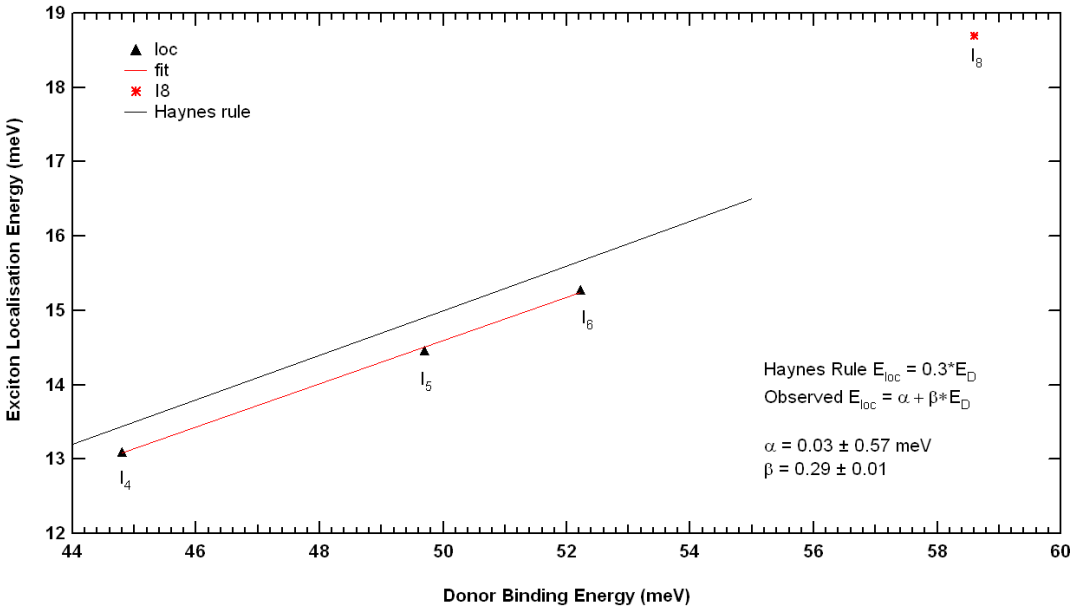

Figure 2-12 Hayne fit of donor binding energies

Localisation Energy	Donor Binding Energy
44.79	13.09
49.74	14.41
52.21	15.26

Table 2-5 TES identification

The TES of the neutral donor bound excitons are observed in the region around 3.324 eV. Identification of the individual transitions can prove difficult. However Haynes rule states that by plotting the localisation energy (the energy difference between A_T and D^0X) against the donor binding energy [(4/3)*(E_{1s} - E_{2p})] the energies should fall on a

straight line of slope 0.3 that intercepts the origin. Figure 2-12 shows the measured experimental data with a straight line fit compared to the expected Haynes rule fit. The slope and fit indicate that ZnO does in fact closely follow Haynes rule, contrary to earlier suggestion by Look et al[65] and suggest that the 3.3332 eV peak identified by them as a TES transition that violates Haynes rule is in fact a surface defect donor bound exciton and not a TES transition.

2.1.5 LO phonon region

The PL spectrum in the range from 3.0 eV to 3.3 eV is dominated by the LO phonon replicas of the near band edge features. The spacing of 72 meV is consistent with that found in literature. In Figure 2-13 the LO phonon peaks in this range have been associated with their corresponding parent transition.

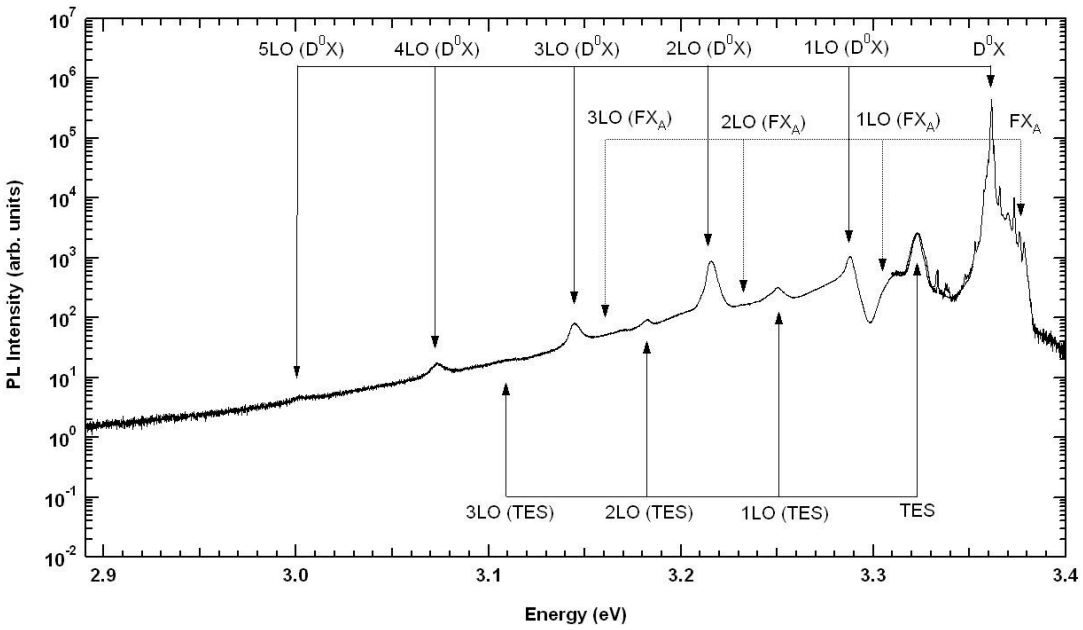

Figure 2-13 NBE – LO phonon region – 4K PL

2.1.6 Donor-Acceptor pair identification in LO phonon region

The 2LO (D^0X) peak at 3.217 eV has been designated as a donor-acceptor pair recombination by both Teke et al and Meyer et al due its position in the spectrum. Power dependent measurements have been carried out in this work to determine the veracity of this claim.

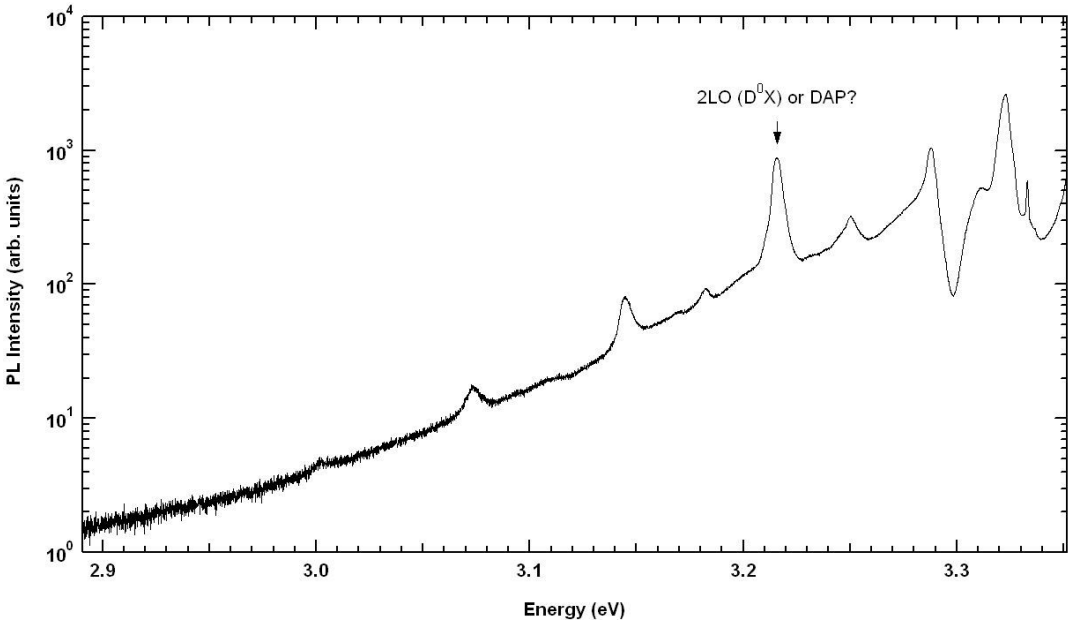

Figure 2-14 DAP identification

A series of neutral density filters were used to attenuate the excitation source. The laser intensity incident on the sample was varied over the range 10 W/cm^2 –> 30 mW/cm^2 .

The energy of a DAP transition can be expressed as $E_{DAP} = E_g - E_d - E_a + E(r^{-1})$

That is to say, the energy of the recombination is equal to the energy of the band gap, less the distance of the donor band below the conduction band and the acceptor band above the valence band, as well as a third, radially dependent term which is a measure of the Coulomb attraction between the donor and acceptor which is itself a function of the mean distance between donor-acceptor pairs. The model for DAP transitions suggests that as the intensity of the excitation source increases the concentration of donors and acceptors also increases. As a consequence the mean distance between donor-acceptor pairs is decreased, resulting in an increase in the term $E(r^{-1})$ and a subsequent blue shift of the E_{DAP} transition.

By varying the intensity of the laser over a suitable range, it should be possible to observe a blue shift in the energy of any DAP transitions.

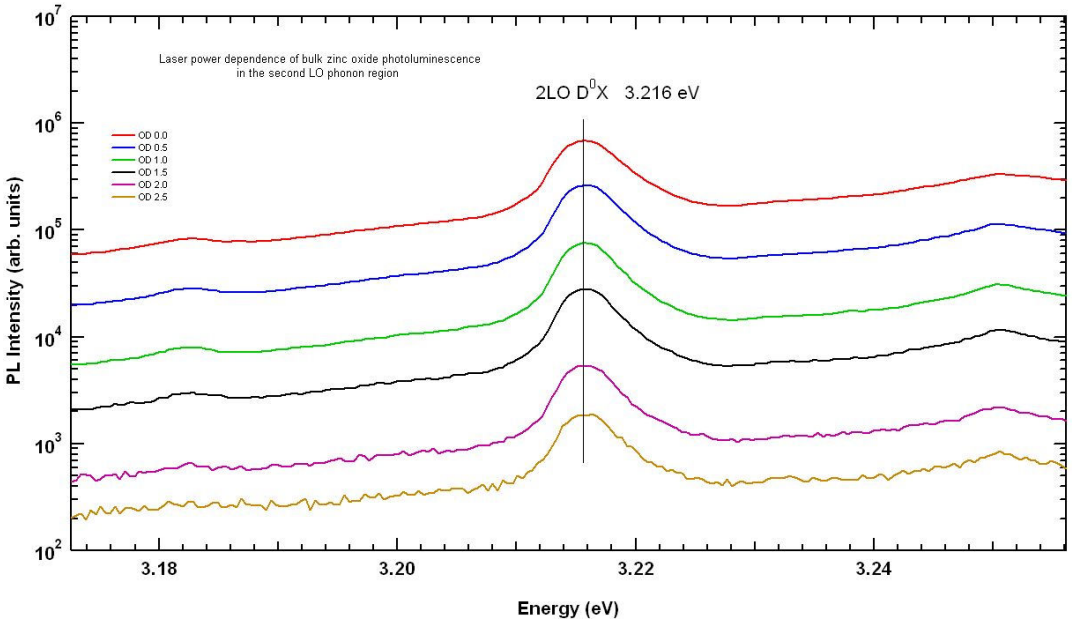

Figure 2-15 Power dependence test of DAP 4K PL

Figure 2-15 shows the result of an experiment performed in such a manner. As can clearly be seen, varying the intensity of the excitation source over a range of almost three orders of magnitude produced no observable shift of the peak, in either direction. Further, tracking the peak intensity of the emission shows that the intensity matches that of the assigned D^0X parent peak within the calculated uncertainty.

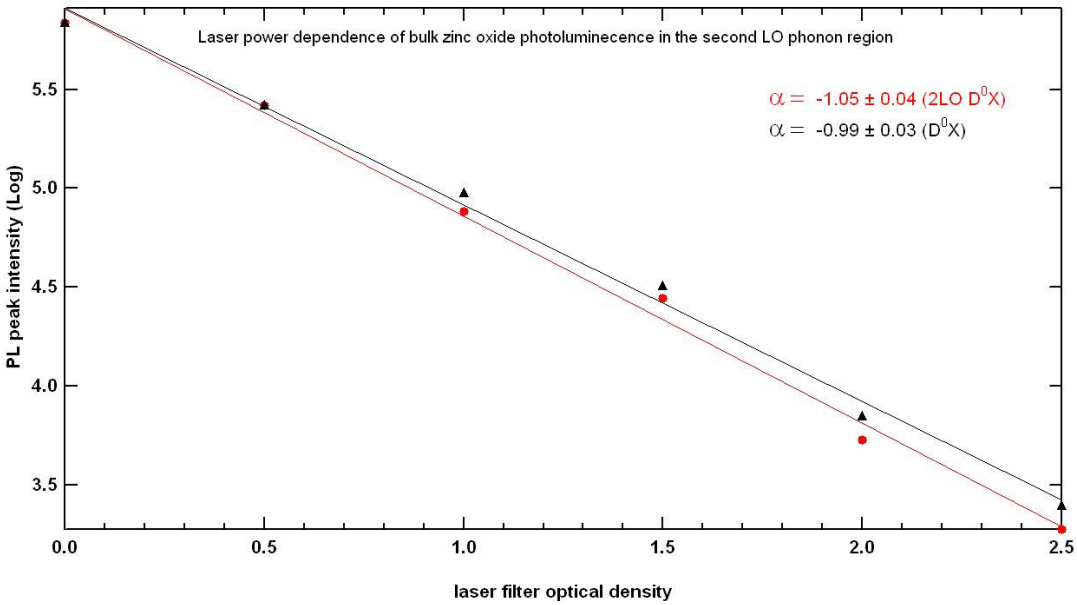

Figure 2-16 Laser power dependence of PL peak intensity

Another signature of DAP transitions is a non-linear response to changes in the excitation intensity. By varying the incident laser power with a series of neutral density filters it is shown in Figure 2-16 that the so-called DAP transition displays a clear linear decrease in intensity with a corresponding decrease in the laser intensity.

Schmidt et al[52] established previously that a DAP transition is expected to display an α coefficient of less than one while a bound exciton is expected to be between one and two..

In addition this intensity relationship closely matches that of the D^0X transition, another strong indication that the peak is actually the 2LO of the D^0X.

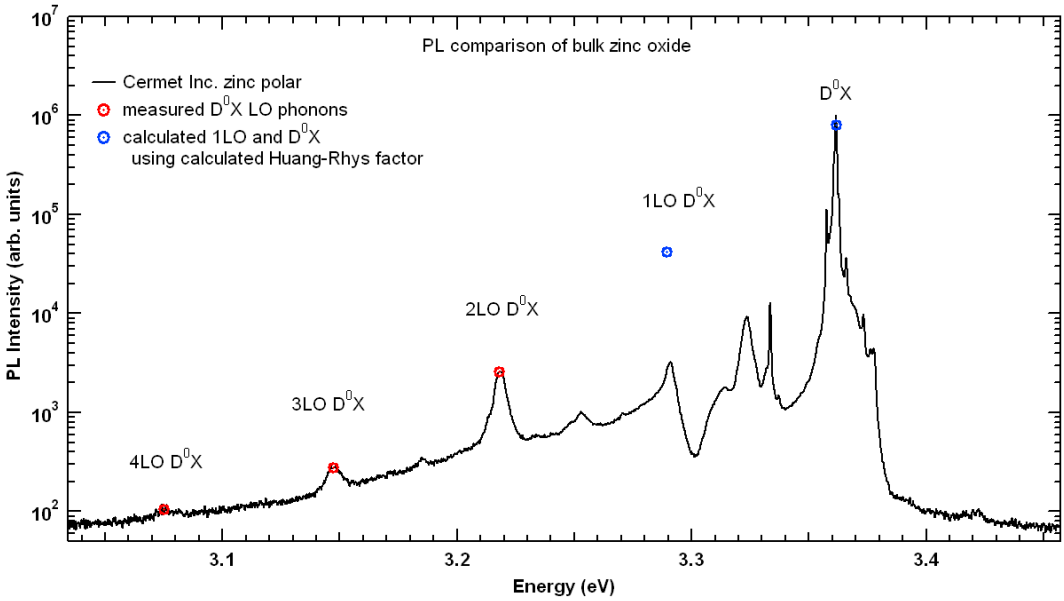

Figure 2-17 Using Huang Rhys factor to predict 1LO and 0LO phonon lines

Using the 2, 3 and 4 LO phonon replicas in Figure 2-17 to calculate the Huang-Rhys factor for the sample allows to calculate the predicted intensity of the 1LO and 0LO phonon peaks.

To a good approximation, the Huang-Rhys factor (S) can be calculated by:

$$S = \frac{I_{0\to1} + 2I_{0\to2} + 3I_{0\to3}}{I_{total}} \text{ [66]}$$

The 1LO phonon clearly shows to be less than the predicted intensity, however this is almost certainly a result of the Fano coupling between the 1LO and the background[63, 64]. The result is a reduction in intensity and an absorption dip on the high or low energy side of the transition, depending on the sign of the Fano parameter. Calculating the intensity back to the zero phonon line shows good agreements between the intensity predicted by the calculated Huang-Rhys factor and the observed PL intensity. This fact provides additional evidence that a DAP model is not required to explain the position and intensity of the emission at 3.218 eV.

2.1.7 Variations in the NBE PL of the two polar faces

The polar nature of c-plane zinc oxide has implications for zinc oxide semiconductor device applications, especially with respect to electrical contacting and the surface-air interface. Although much of the experimental techniques fall outside the scope of this thesis, excellent results have been obtained showing the effect of polarity on surface potentials and morphology[67]. Differences in the optical emission of the two polar faces have been discovered and measured in low carrier concentration, hydrothermally grown, bulk ZnO. Although the practical implications of these differences are yet to be determined, they offer a useful non destructive means of determining which of two opposite faces terminates with zinc, and which terminates with oxygen.

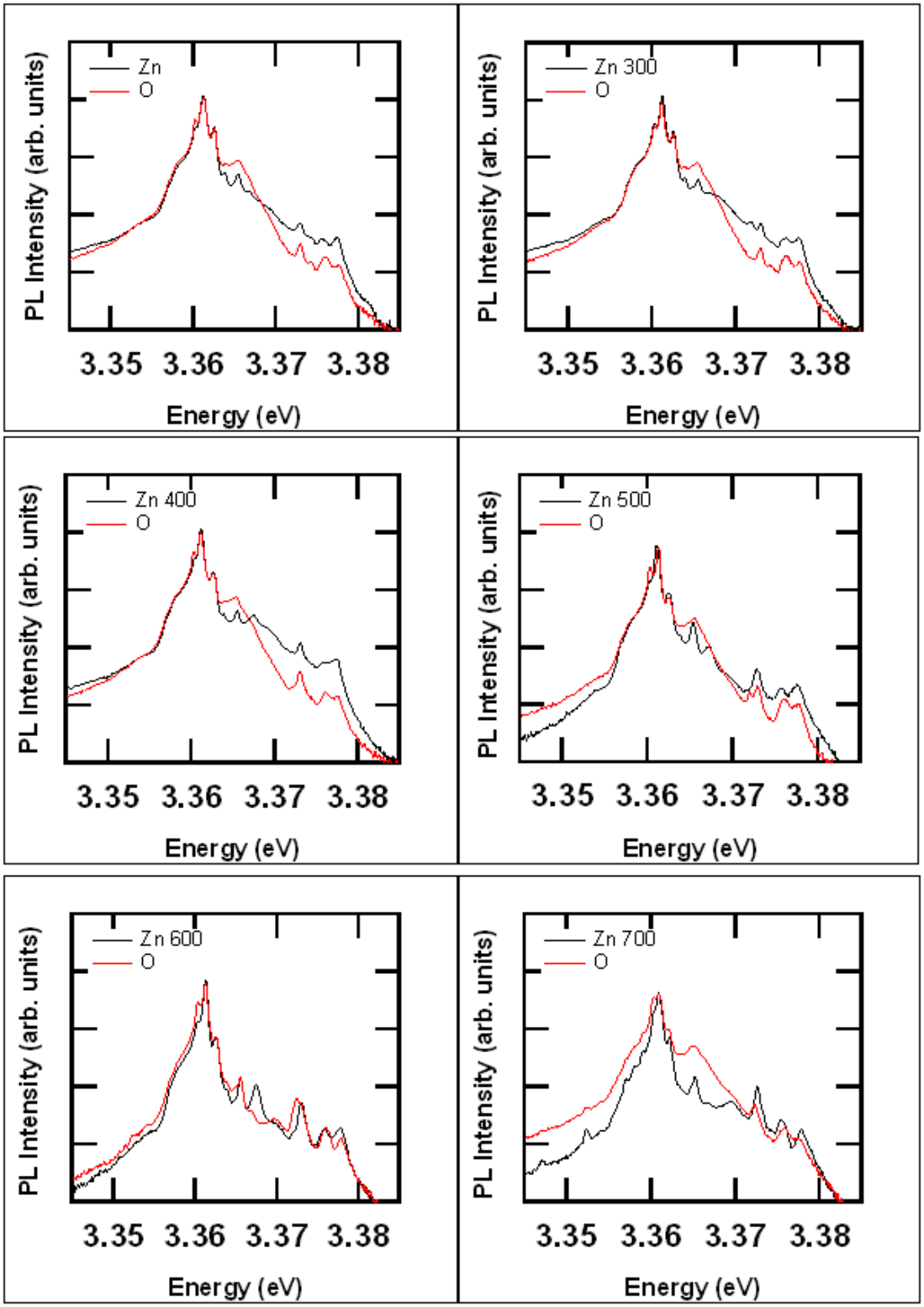

Figure 2-18 Annealing temp dependence of 4K PL of both polar faces

Figure 2-18 shows a narrow range in the near band edge region and illustrates how the PL of the two polar faces differs over a range of annealing temperatures for bulk zinc oxide samples annealed in vacuum.

The results show that in unannealed films the Zn polar face has a significantly stronger PL emission from the A_L and A_T free excitons. This may be as a result of band bending induced by the surface polarity in films with a low intrinsic carrier concentration. The other notable feature is the increased luminescence on the oxygen face from the region of the spectrum typically associated with B-excitons bound to neutral donors, however the relative broadness of the emission compared to the Zn face suggests an alternative cause, occupying the same energy by happenstance.

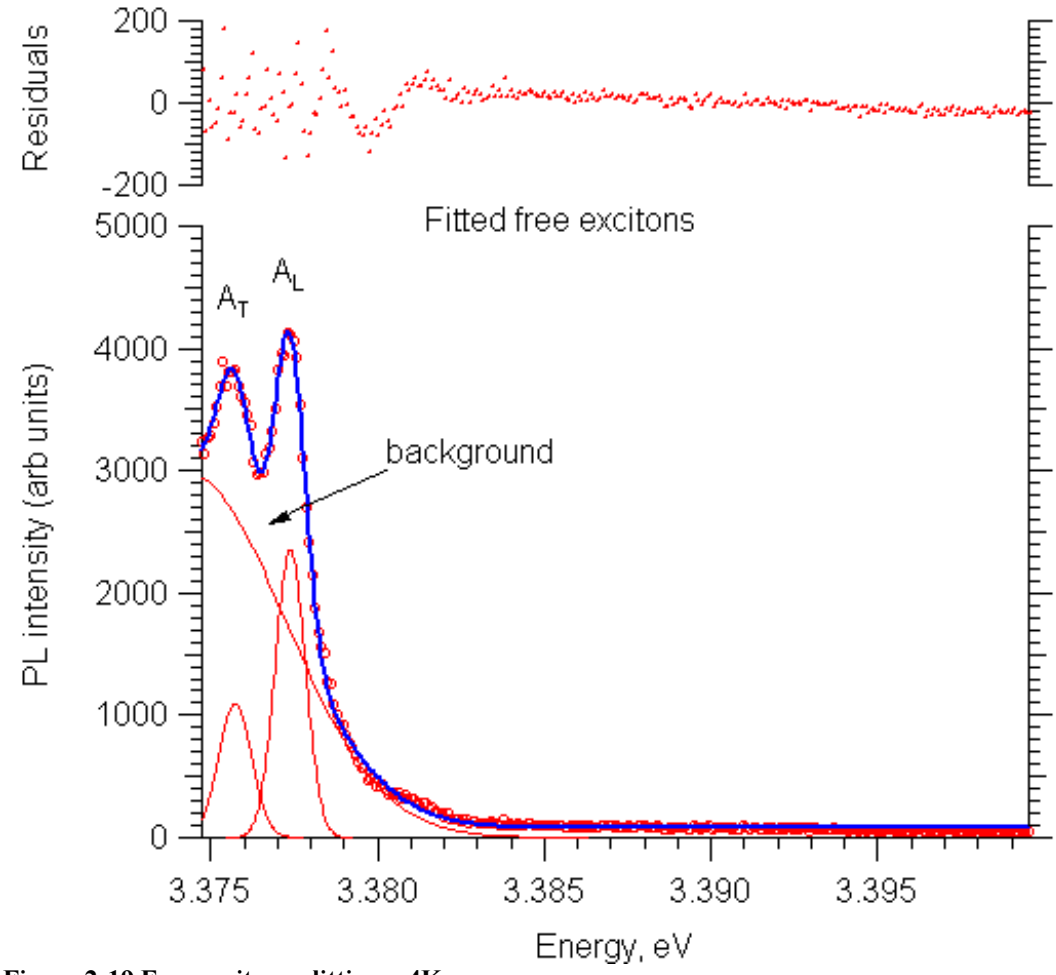

Figure 2-19 Free exciton splitting – 4K

A range of values for the splitting of the A_T and A_L free excitons have been reported[10, 54, 57, 60], often times confusing the identification of individual peaks. At first this discrepancy was assumed to be the result of mechanical and experimental uncertainties in the obtained data. However when a series of best fits are produced for the free exciton data, in order to determine the precise splitting of the peaks, it becomes

apparent that the $A_{T\text{-}L}$ splitting can vary considerably. Even for a single sample that has been cleaved into many pieces which have subsequently been annealed at different temperatures.

Figure 2-19 shows the fitting process by which the peak positions are identified and from which the splitting is obtained. By plotting the measured peak position for each of A_T and A_L on each face, as has been done in Figure 2-20, it possible to demonstrate how the splitting varies as a function of annealing temperature. The "residuals" at the top of the figure represent the variance between the data points and the corresponding Gaussian fit. They may be used to provide a clear visual representation of the quality of a fit.

It is clearly shown that the splitting of the two peaks varies considerably, from 2.4 meV at its maximum when the oxygen face is annealed at 700 ^{o}C, down to 1.2 meV when annealed at 400 ^{o}C. With this in mind it becomes possible to see how confusion may arise in the identification of the individual transitions.

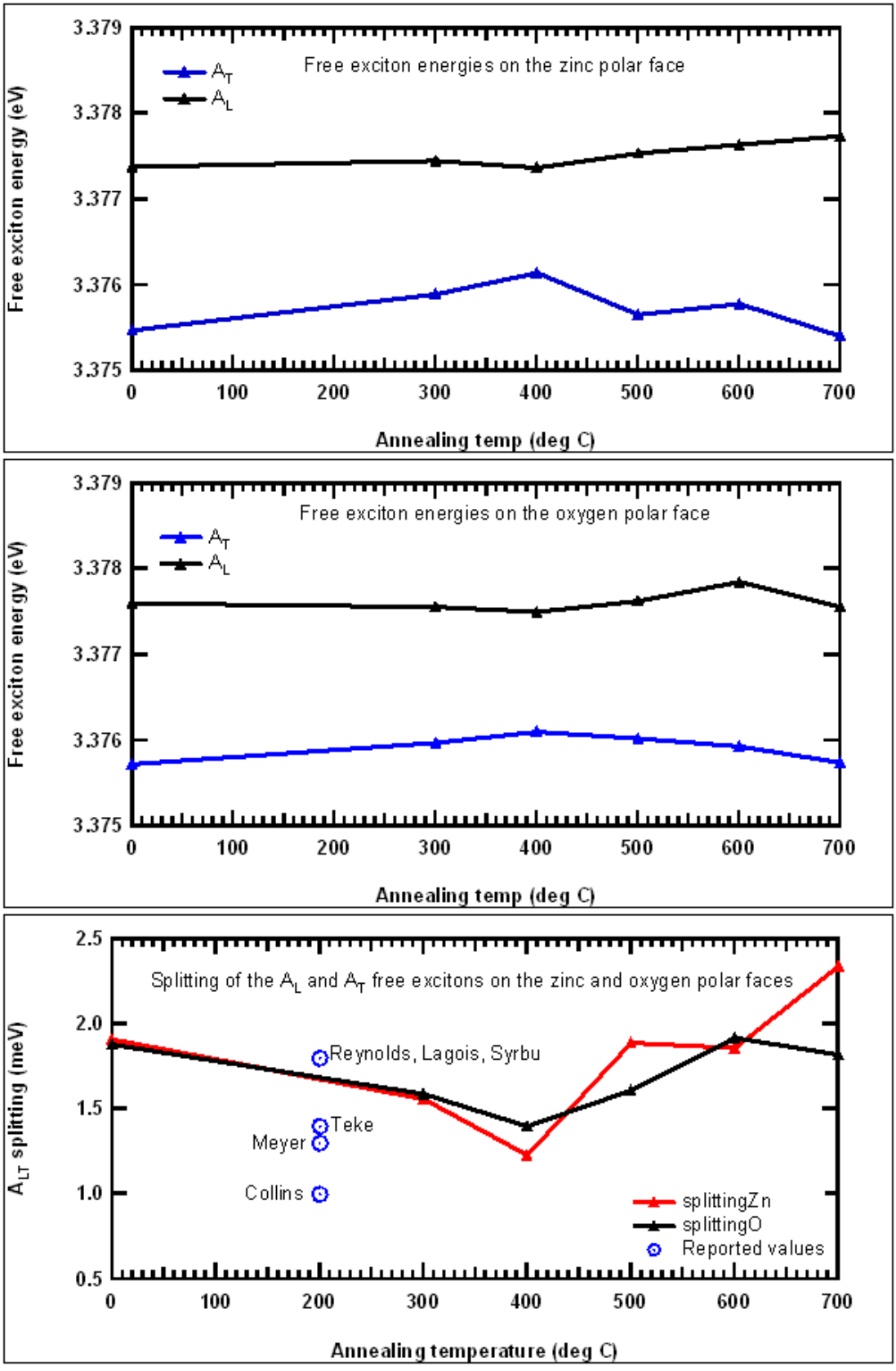

Figure 2-20 Free exciton splitting for Zn and O polar faces, with literature references

2.2 Deep level defects

While bulk zinc oxide PL may be dominated by the near band edge emission, characterising and identifying the deep donors and acceptors that make up the deep level emission is also of great importance in understanding the effect of vacancies, anti-sites, interstitials, and atomic impurities, on the optical and electrical properties of the material.

While the relative width and spacing of these transitions is vastly greater than that of the NBE, and the number of peaks far fewer, confusion still abounds as to their origin.

Emissions extend from 1.7 to 3.0 eV. The nature of many of these transitions is still a subject of debate. For example, Reynolds et al[68] suggest a deep acceptor is involved. Dingle[69] and Garces[70] among others[83, 84] assign the emission to Cu impurities. Vanheusden et al[71] identified an emission at 2.42 eV correlating with oxygen vacancies, in keeping with later results[72-78]. Other candidates assigned to the deep level emission include interstitial Zn and O[79-81], zinc vacancies[82-84] and the oxygen anti-site[85].

The deep level emissions for a range of bulk samples will be fitted with Gaussians and their positions compared with those previously measured or calculated in existing literature. In the case where consensus is apparent, the possible causes of the abundance of the particular defect will be discussed.

2.2.1 Melt-growth and Hydrothermal growth

Figure 2-21 shows the deep level PL emission for single crystal bulk zinc oxide sourced from three different producers. As has been mentioned previously, Tokyo Denpa and MTI crystals are grown by the hydrothermal method. Both of these samples show clearly visible luminescence centred around 2.43 eV which is consistent with the model for oxygen vacancies proposed by Vanheusden in 1995[71] although this is not in agreement with the value of 1.62 eV calculated by Sun et al using the full-potential linear muffin-tin orbital method for the same defect[86].

Cermet crystals are grown by the melt-growth technique and have consistently been found to display little to no deep level emission.

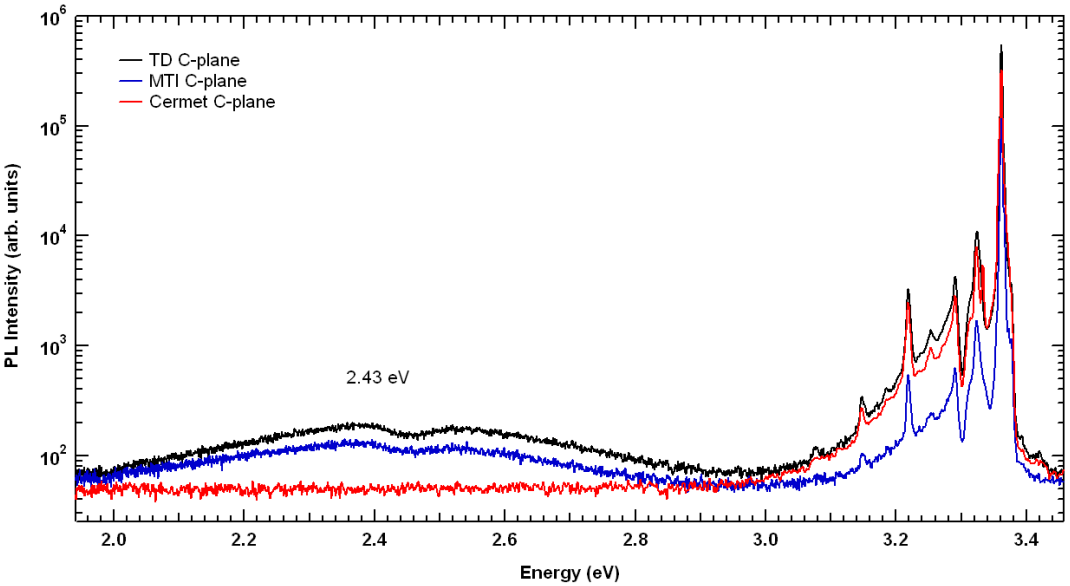

Figure 2-21 Deep level emission for bulk ZnO grown by different methds

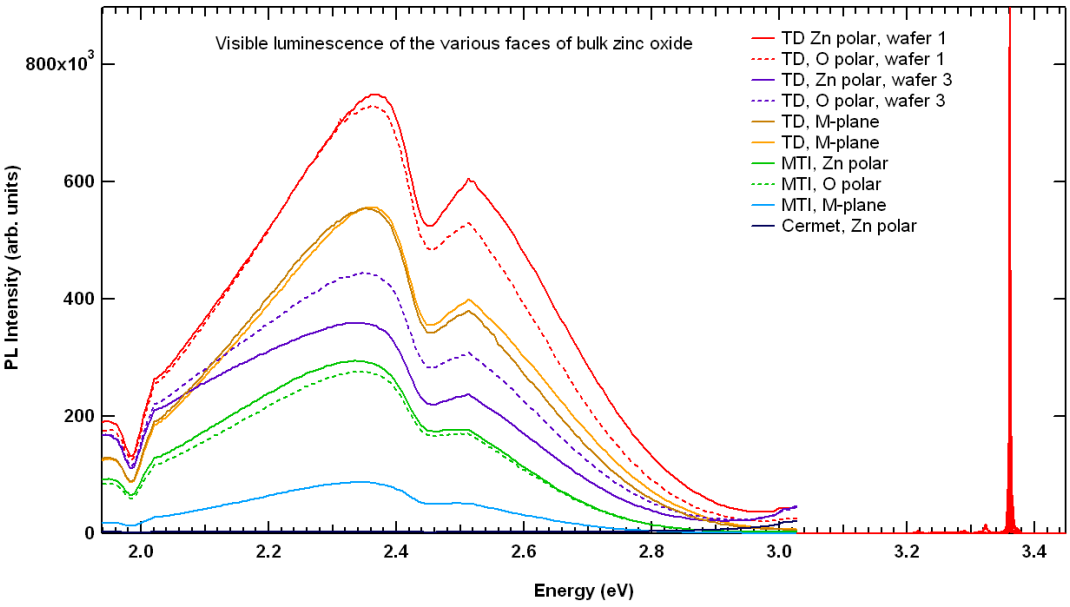

Figure 2-22 Influence of growth method on deep level PL emission

The PL results on a linear scale y-axis shows both the relative difference in line width between the NBE and deep level emissions and emphasises the absence of the deep level of melt grown Cermet crystals relative to hydrothermally grown Tokyo Denpa and MTI crystals.

2.2.2 Correcting for grating defects in the green and orange

The spectrometer grating used in these experiments has two noticeable defects in its diffraction pattern, one centred around 2 eV and another larger one at 2.4 eV. These defects are a feature of the wavelength dependent diffraction grating transmission efficiency and are peculiar to a particular grating. It is still possible to fit Gaussians to the data by extrapolating a straight line across the affected region. An example of this extrapolation can be seen in Figure 2-23

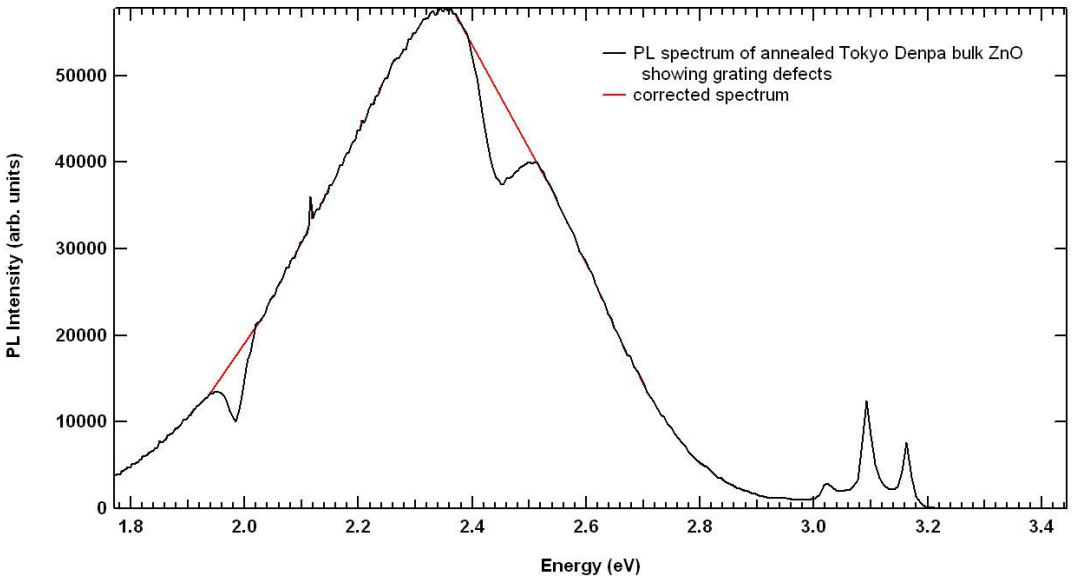

Figure 2-23 Correcting for grating defect

Following this correction, the peak can be fitted with two Gaussians, though due to the large line width and significant overlap between the two peaks, the precise position of the peaks is the subject of frequent debate.

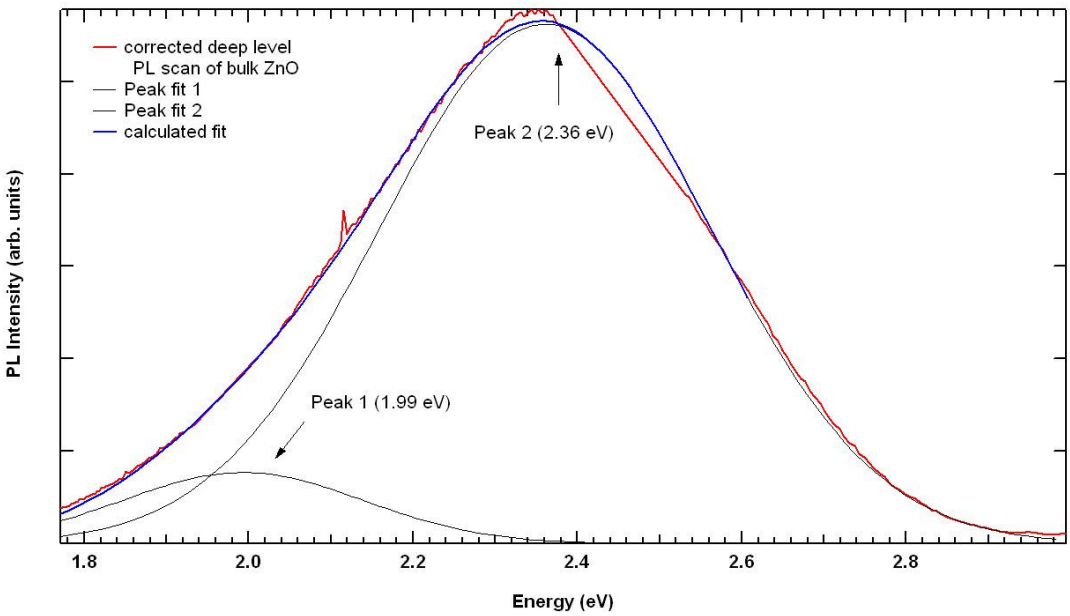

Figure 2-24 Double peak fitting of deep level emission - 1

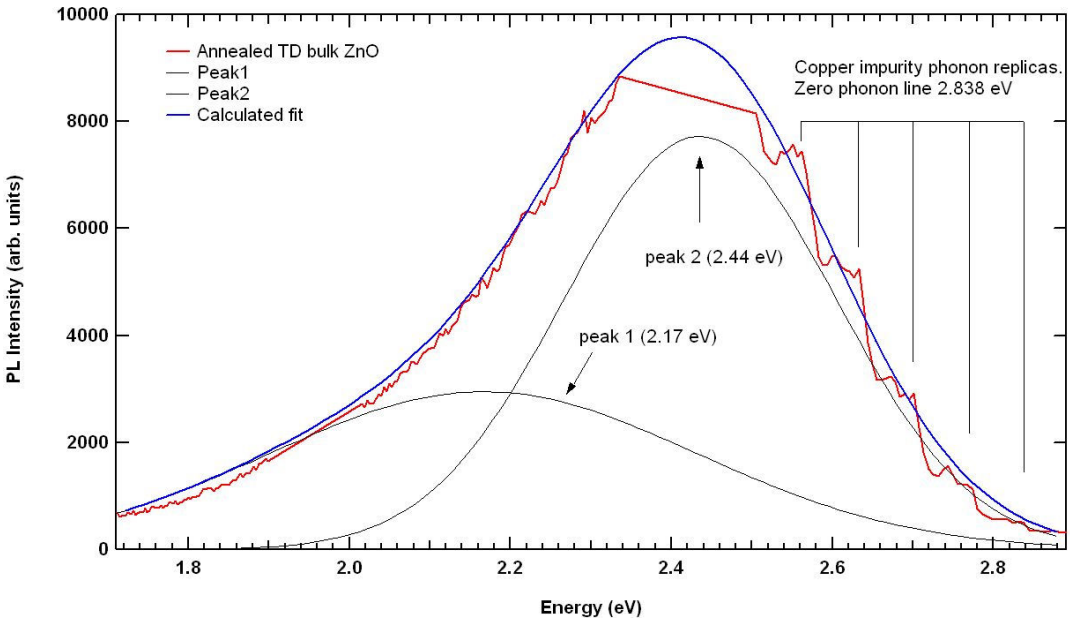

Figure 2-25 Double peak fitting of deep level emission - 2

Figure 2-24 and Figure 2-25 show two PL spectra clearly dominated by different peaks. The former, when fitted with two guassians, shows one emission peak at 1.99 eV and another at 2.36 eV. The latter shows an emission peak at 2.17 eV and another at 2.44 eV. It would be fair then, to assume that a complete model of the deep level luminescence of bulk zinc oxide requires 4 separate peaks. However by introducing a 5th peak, this time at 2.28 eV, it becomes possible to show that the emission seemingly located at 2.17 eV is actually a linear combination of this 5th peak, and the peak located at 1.99 eV. It is also possible to show that the emission at 3.36 eV is a linear combination of the same 5th peak, and the peak at 3.44 eV.

By doing this, we reduce the number of emission peaks required to model the deep level PL of bulk zinc oxide from four to three, though it requires fitting 3 gaussians to each spectrum instead of the original two.

2.2.3 Fitting for three transitions

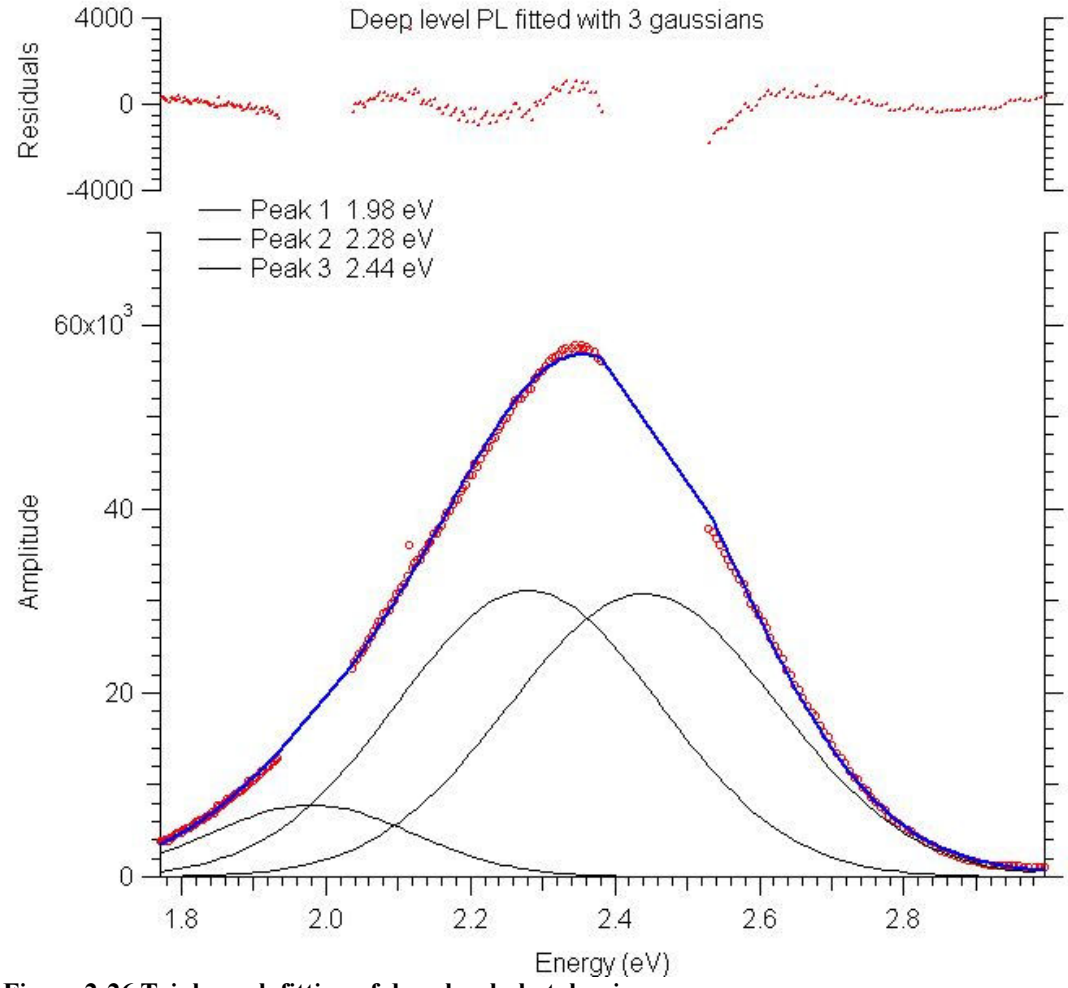

Figure 2-26 Triple peak fitting of deep level photoluminescence

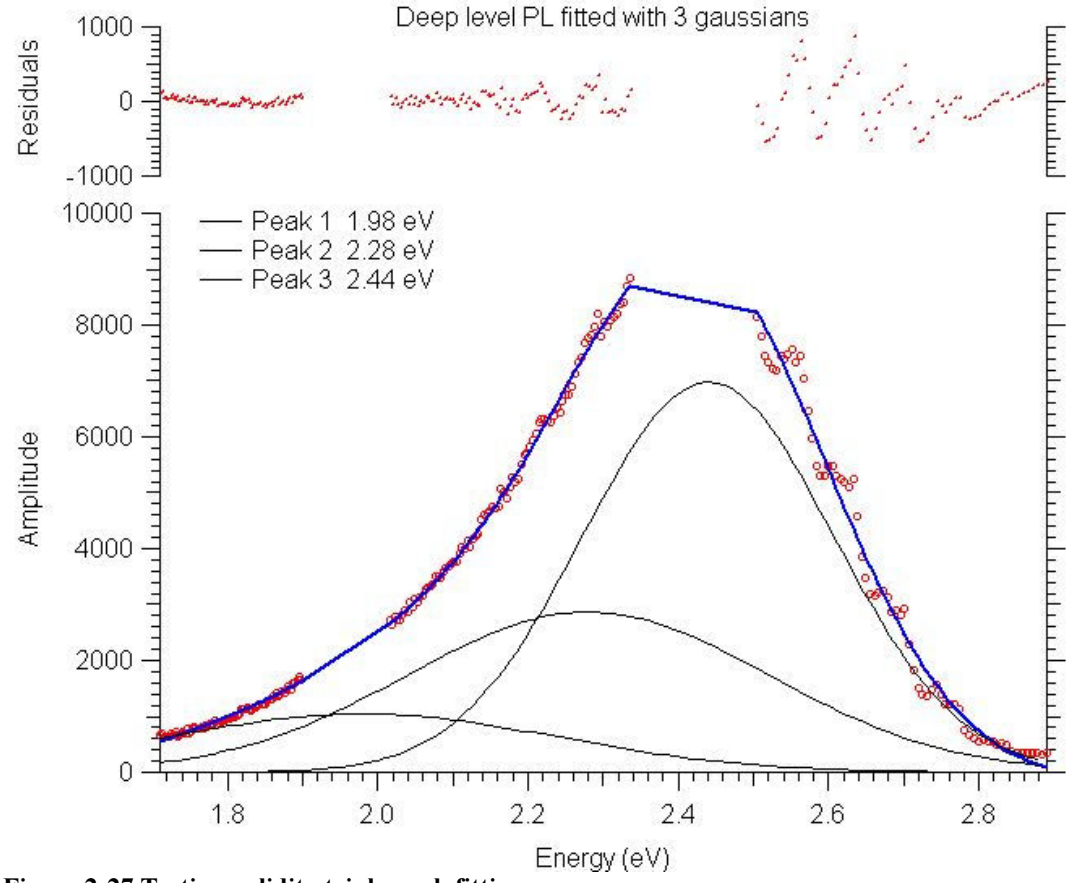

Figure 2-27 Testing validity triple peak fitting

Figure 2-26 and Figure 2-27 show an example of this triple peak fitting method. The residuals between the data and the fit in Figure 2-26 show how the grating defects have impacted the fits. The periodic modulation of the residuals in Figure 2-27 indicate the presence of copper impurities which will be shown in the next section..

2.2.4 Peak response to temperature

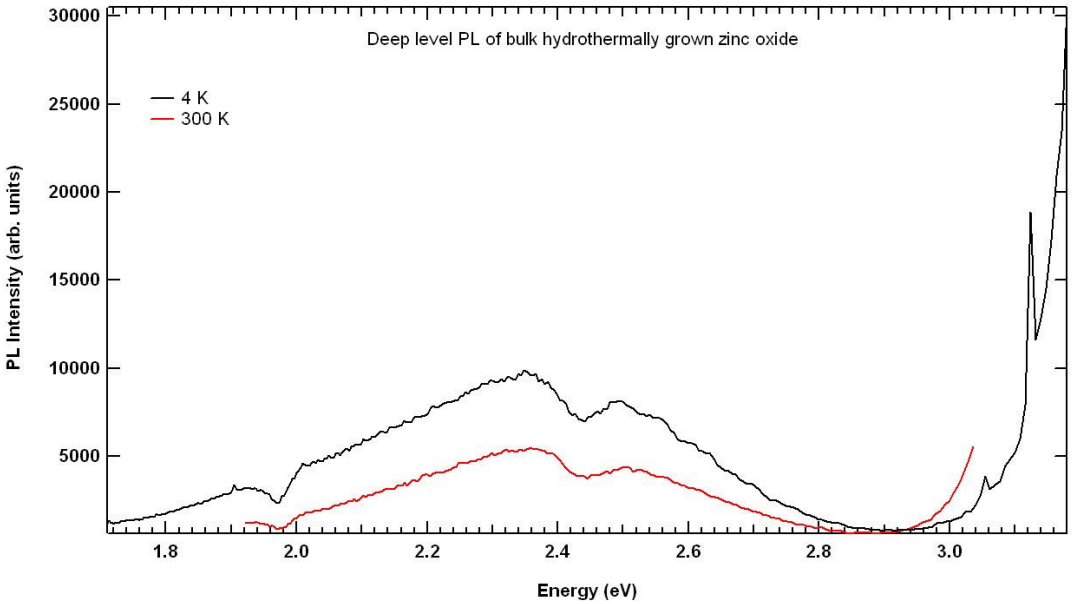

Figure 2-28 Deep level emission response to temperature change

Figure 2-28 shows the effect of temperature on the peak position of the deep level emission. It is clear to see that both the position and relative intensity of the three peaks are largely independent of temperature over the range studied. This allows for a high degree of confidence in comparing with the literature for results obtained at various temperatures.

2.3 Annealing trials

Annealing is the process of heating a material in order to change the physical structure, or to drive impurities in or out by controlling the mean energy of the individual atoms. By annealing samples over a range of temperatures and in different atmospheres it becomes possible to gain a better understanding of the nature of the various dopants and structural defects that are the root cause of many optical transitions.

In this experiment a single piece of Tokyo Denpa single crystal bulk zinc oxide was cleaved into several pieces and annealed over a range of temperatures for 90 minutes in an oxygen atmosphere. The effect on both polar faces was studied with PL and the emergence of copper related luminescence was observed.

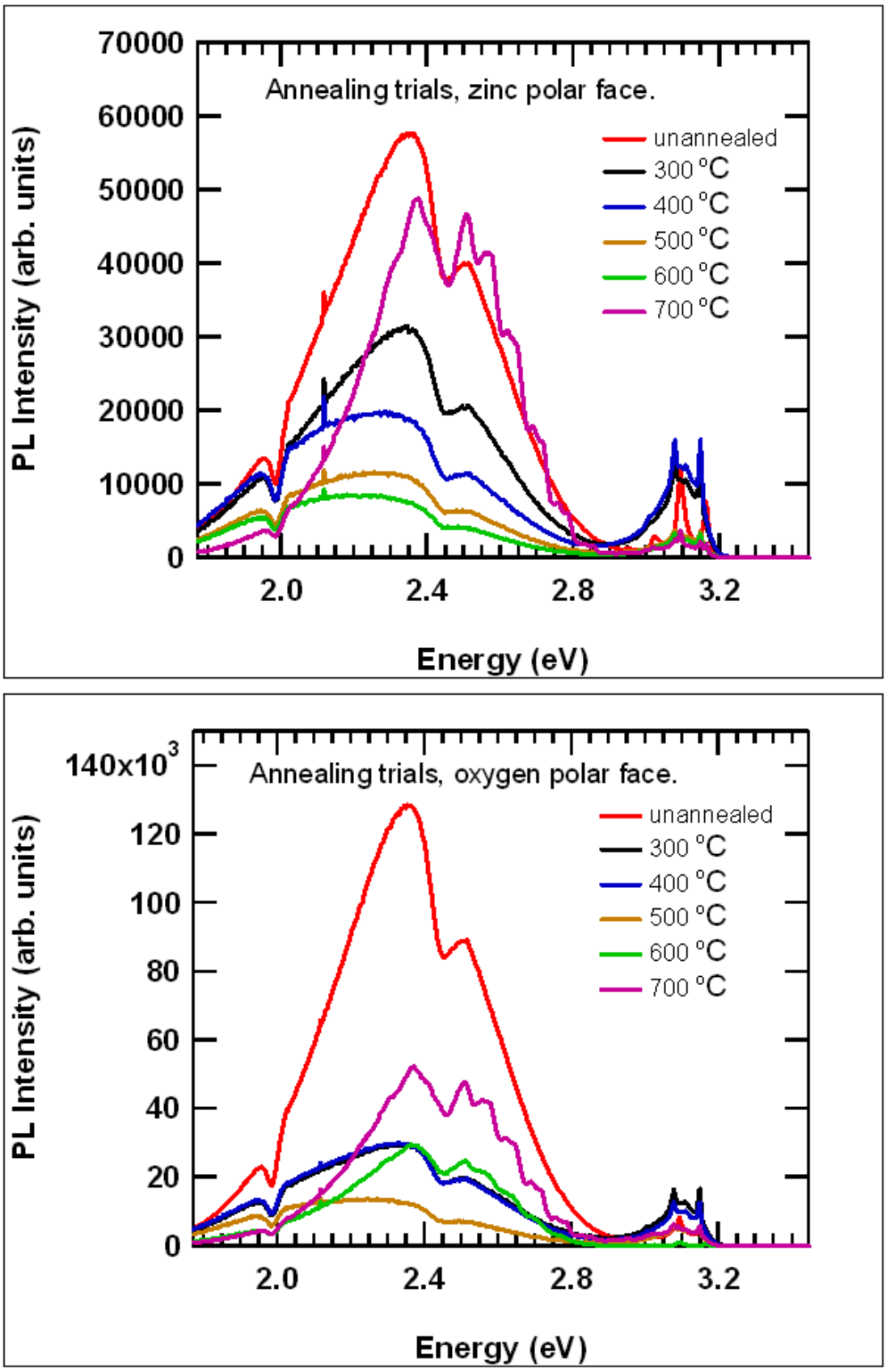

Figure 2-29 Emergence of copper related emission on Zn and O polar faces after annealing

Figure 2-29 shows the PL spectra of the annealed crystals, the PL intensity can be seen to decrease as the annealing temperature increases and is centered around 2.3 eV, up until a temperature of 600 ^{o}C for oxygen polar face and 700 ^{o}C for the zinc polar face. Above these temperatures the PL is dominated by a 2.44 eV peak while the lower energy emissions are quenched.

The NBE emission is distorted due to the use of filters to eliminate second order effects, and visible wavelength optimisation of the optical layout.

To perform a more quantitative analysis the emission spectra have been fitted using the triple transition model discussed earlier in the chapter. The peak positions have been fixed however the width and intensity remain unconstrained. It is expected that by observing how the deconvoluted peaks individually respond to a change in annealing temperature, the various proposed models for each transition may evaluated for plausibility.

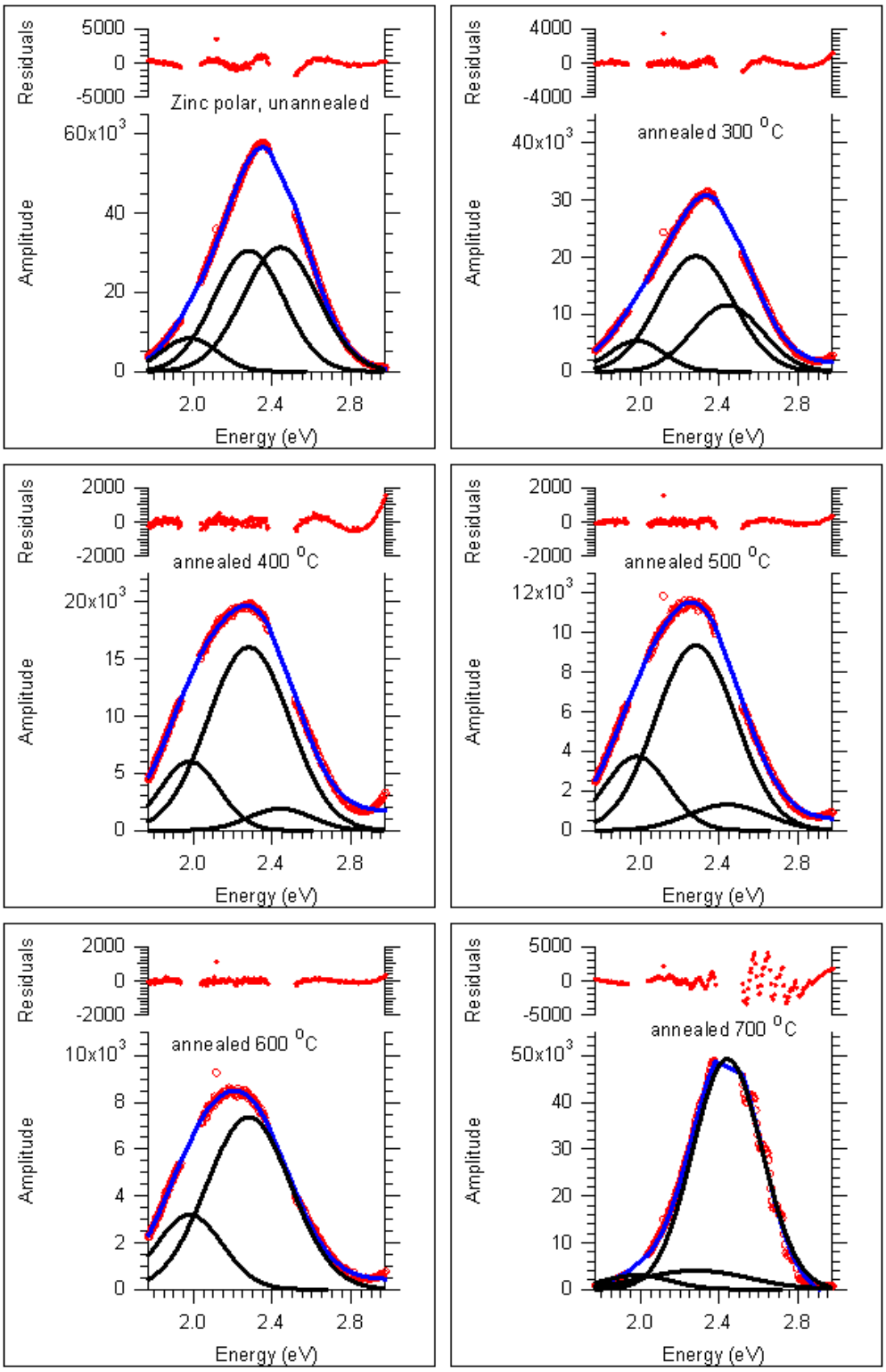

Figure 2-30 Triple peak fitting for annealing series – Zinc face

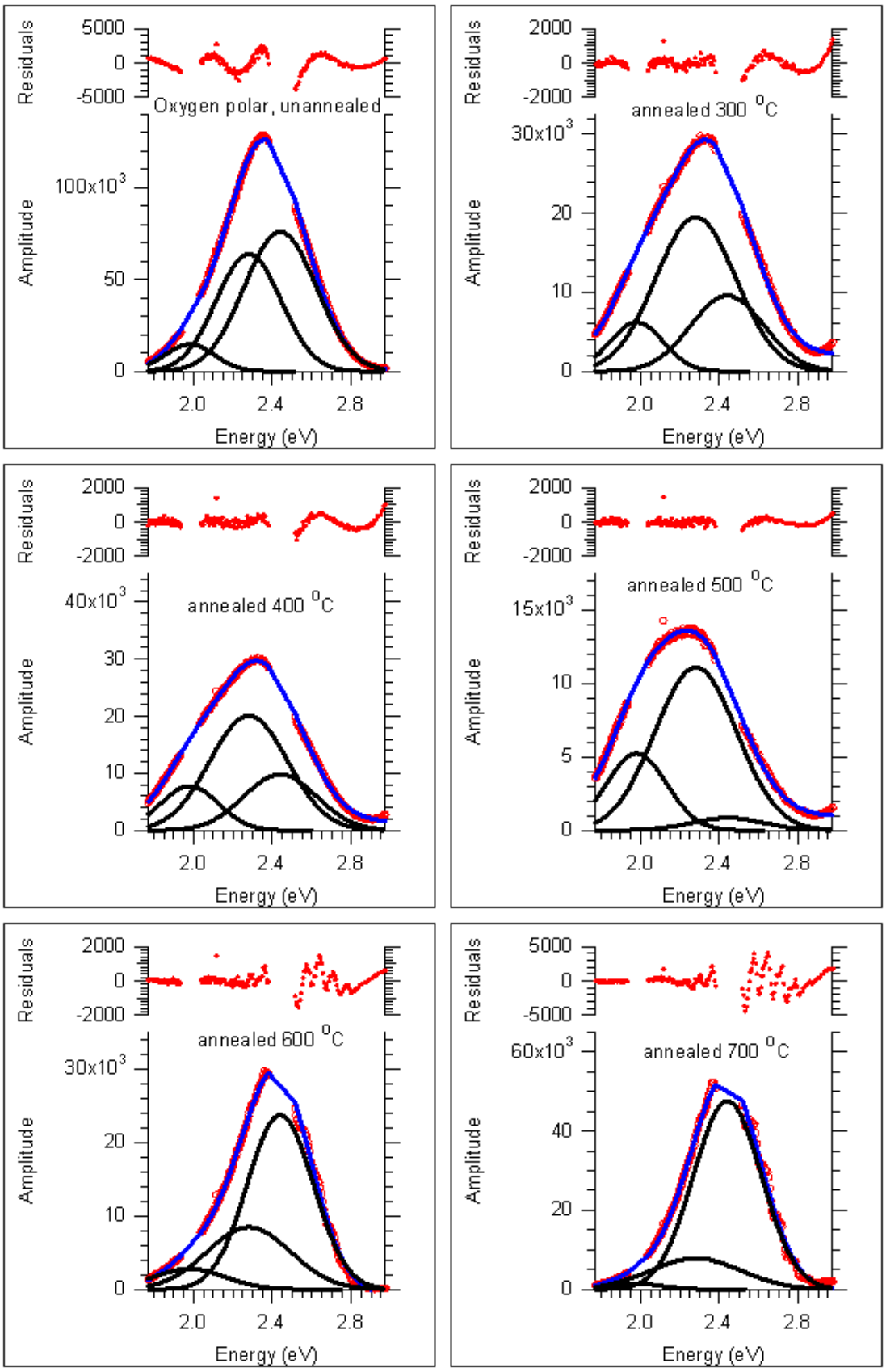

Figure 2-31 Triple peak fitting for annealing series – Oxygen face

Figure 2-30 and Figure 2-31 show the effects of the annealing trials on the zinc and oxygen polar faces. The spectra were fitted using three fixed position guassians, the assigned positions of which were determined through reference to the literature and a survey of unbounded fits. Included in the graphs is the residual trace left over from the subtraction of the sum of the fitted peaks from the raw data. This shows that the fits break down around the grating defects, and also on the high energy side of the spectrum due to the tailing off of the near band edge emission. Overall the fits show good agreement with the data.

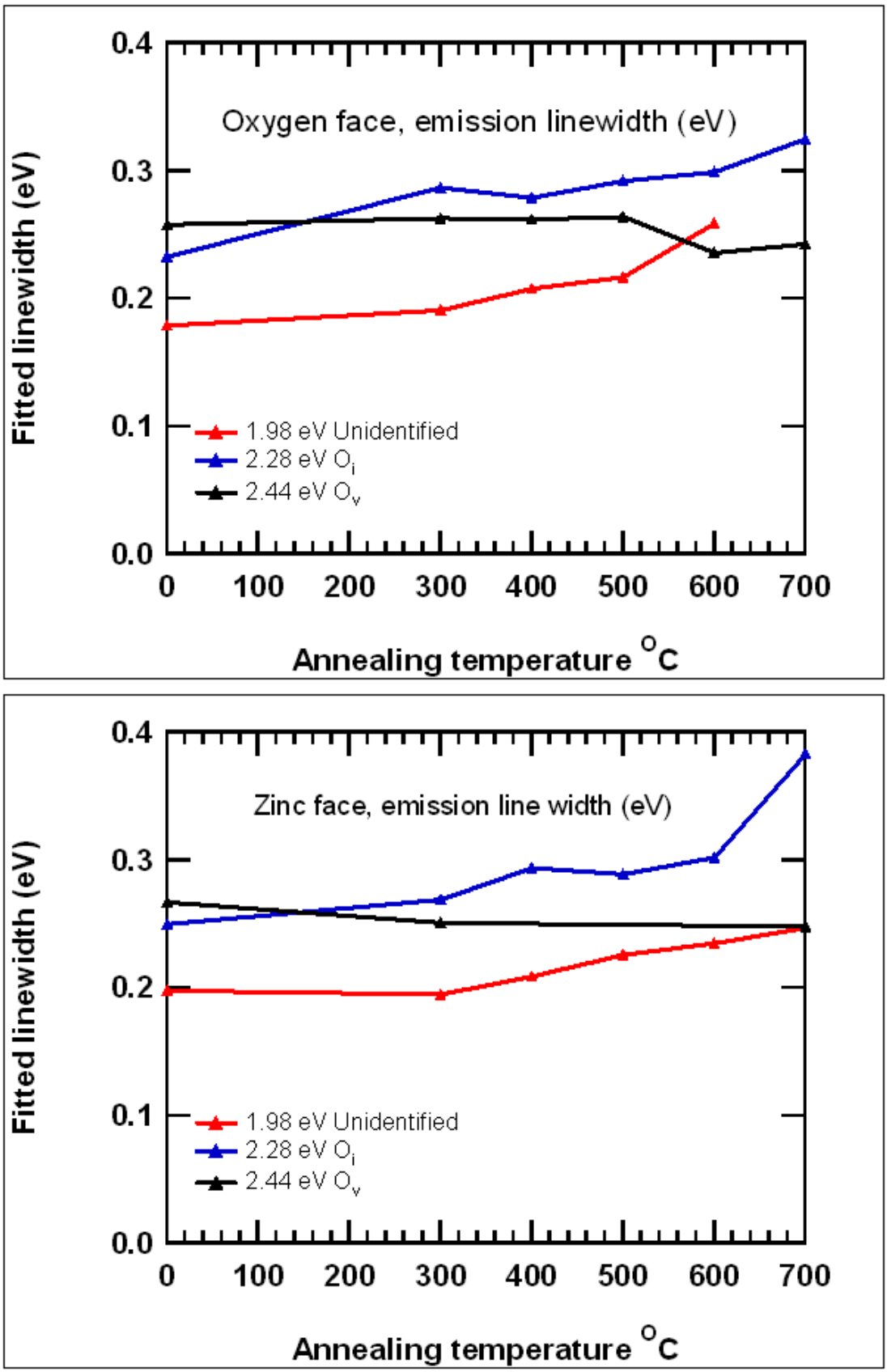

Figure 2-32 Checking continuity of fits across the range – 4K PL line widths

To confirm the validity of the fitting method the widths of peak fits are show against the annealing temperature in Figure 2-32. The change in line width with annealing temperature shows a monotonic variation across the range. Data points have been excluded in the case where peak intensity has dropped below a threshold value, in which case the line width has little influence on the quality of the fit.

The line widths of the emissions at 1.98 eV and 2.28 eV are shown to moderately increase with annealing temperature while that at 2.44 eV is shown to be constant over the observed range.

Figure 2-33 shows how the intensity of the three fitted peaks varies with annealing temperature when annealed in an oxygen ambient. The peak at 1.98 eV decreases with annealing temperature at a near constant rate as does the peak at 2.28 eV. However annealing the films at 300 ^{o}C results in a marked decrease in the 2.44 eV emission and is entirely quenched as the annealing temperature is increased to 500 ^{o}C.

Annealing at temperatures above 500 ^{o}C shows a significant resurgence in the intensity of PL emission from around 2.44 eV. The new emission is modified by the appearance of phonon lines with an energy of 70-72 meV with the zero phonon line (ZPL) at 2.82 eV, a strong indication of copper impurities in the material[69, 87] located on the zinc site within the lattice, although Reynolds et al find little indication of copper in ZnO bulk material observed to be showing similar vibronic structure[68].

The model proposed here will assume the presence of copper impurities. Annealing the samples in an oxygen atmosphere will reduce the number of oxygen vacancies and interstitials, the result of this is a decrease in the intensity of the PL emission at 2.44 eV. As the annealing temperature is increased the rate at which these defects are annealed out also increases, resulting in further decrease in the emission intensity. Occurring simultaneously with the reduction in oxygen vacancies and interstitials is the annealing out of impurities such as hydrogen, along with a corresponding drop in carrier concentration and a lowering of the Fermi level. As the Fermi level drops below the Cu acceptor level (190 meV below the conduction band) the holes become stable and recombination is possible. Thus, while the oxygen vacancy emission at 2.44 eV is diminished by annealing in oxygen, the copper related emission (also centered around 2.44 eV) shows a dramatic increase in intensity as the Fermi level drops below the Cu

acceptor level. What appears to be a single emission first decreasing and then increasing in intensity as the annealing temperature is raised, is in fact two distinct and unrelated emissions that by chance share a similar recombination energy.

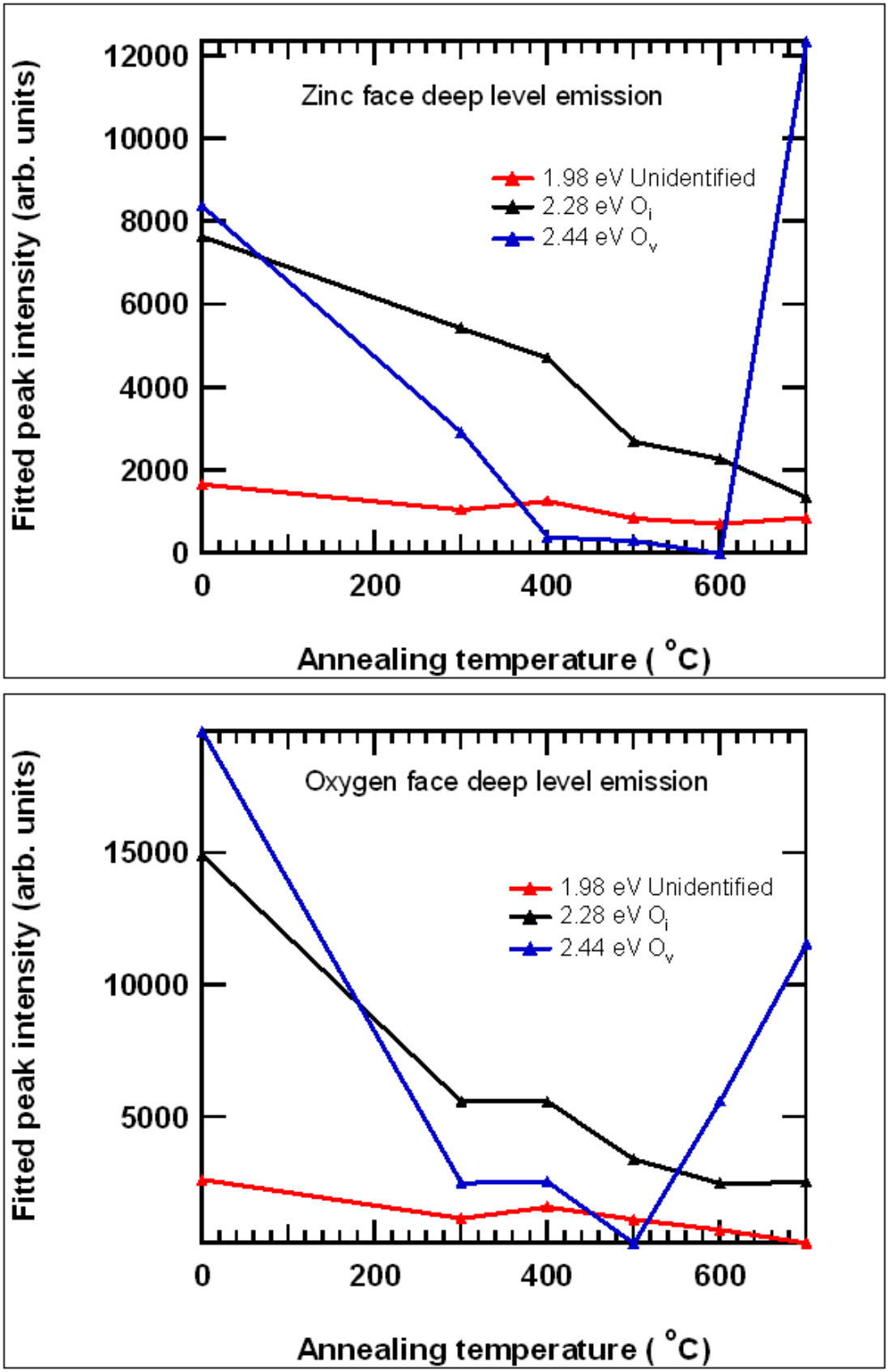

Figure 2-33 Fitted peak intensities for zinc and oxygen polar faces – annealing trials

2.3.1 Annealing in hydrogen forming gas

In order to test the validity of this hypothesis several films are annealed under various conditions in a hydrogen forming gas. It is hoped that by annealing in hydrogen/oxygen the donor level in the material can be influenced and from that, the Fermi level lowered and raised.

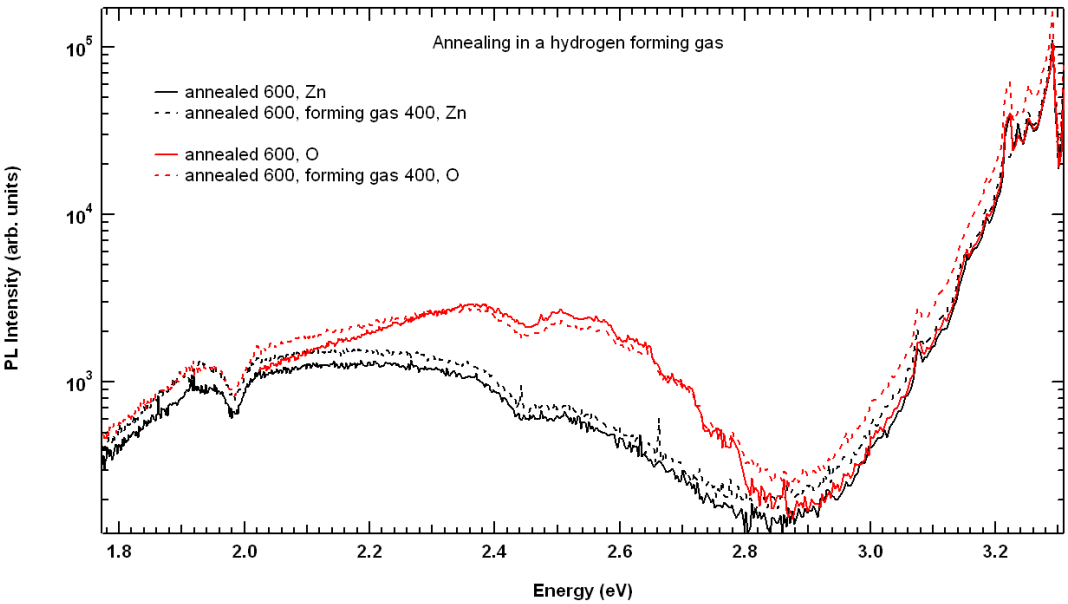

Figure 2-34 Hydrogen forming gas trials – 400 deg C

The oxygen and zinc polar faces are annealed at 600 degree C in oxygen in order to reduce the influence of oxygen vacancies on the luminescence in the region of interest. As observed in previous annealing experiments at 600 ^{o}C the oxygen polar face shows the appearance of vibronic features in the PL spectrum while the zinc polar face shows none.

The samples are then annealed in a hydrogen forming gas at 400 ^{o}C in order to drive hydrogen into the material, however no change is observed in the visible luminescence.

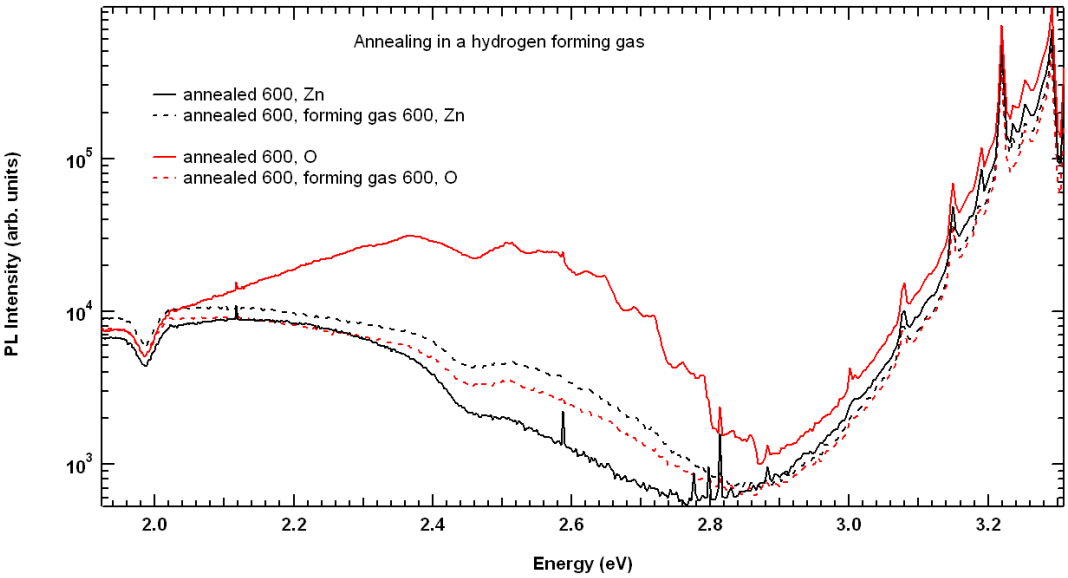

Figure 2-35 Hydrogen forming gas trials, suppression of copper related emission – 600 deg C

The experiment is repeated and illustrated in Figure 2-35 however this time the temperature of the forming gas is raised to 600 ^{o}C. This time the vibronic features are clearly absent in the oxygen face after the forming gas annealing has taken place. This is a clear indication that hydrogen plays a role in the observation of the vibronic features and the results are consistent with a shifting of the Fermi level around a copper related energy level in the band.

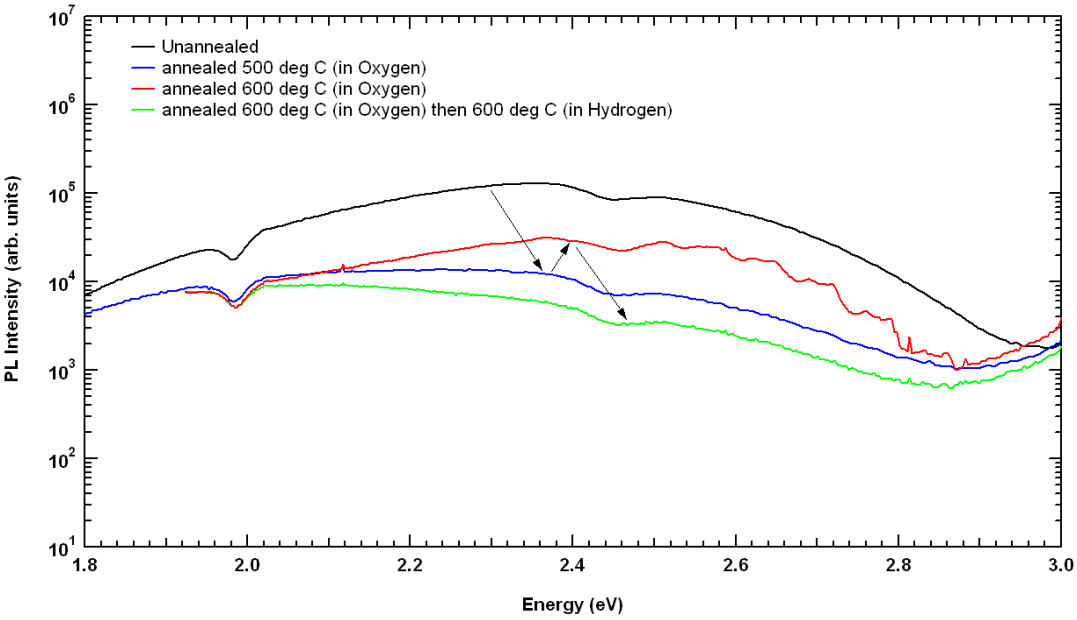

Figure 2-36 Manipulating vibronic features

To fully illustrate the situation consider the series of events seen in figure Figure 2-36. A virgin sample is annealed in oxygen at 500 ^{o}C and a decrease in the emission around 2.44 eV is observed. This is consistent with the oxygen vacancy model. The same sample is then annealed at 600 ^{o}C in oxygen and this time the intensity of the emission increases and vibronic features appear. Consistent with the Fermi level dropping below a Cu acceptor level as defects are annealed out. The sample is then re-annealed in hydrogen forming gas at 600 ^{o}C and the vibronic features are quenched indicating that the Fermi level has once again shifted above the Cu acceptor level.

It is believed that this model is fully consistent with the evidence observed however further experimentation would increase confidence in the model.

2.3.2 Observations requiring further investigation

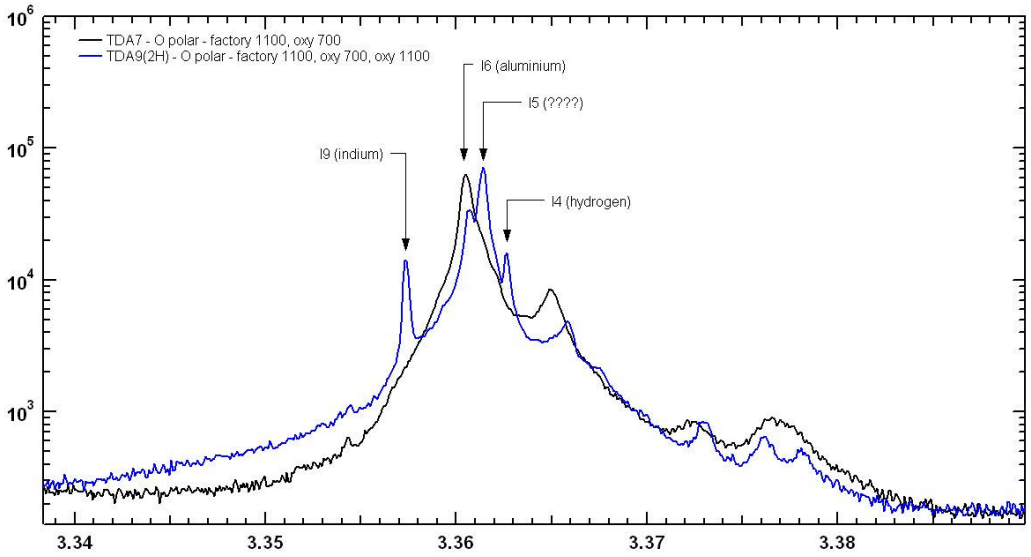

Figure 2-37 Absence of dominant D^0X emission peak – future work

Assignments for the I4,6,8,9 lines are now being made with increased confidence however the line labelled as I5 still remains unidentified. It has tentatively been assigned variously to iron or copper.

For the first time we have observed a zinc oxide sample with the normally prominent I5 line absent. It is our hope that, through the use of SIMS, we will be able to identify a definitive difference in the concentration of trace impurities between the samples that will provide a clear direction for future doping trials.

A positive result will ensure an excellent journal publication of great interest to all researchers working on zinc oxide material.

2.4 Summary of peaks

Summary of PL peaks	
Peak Energy (eV)	Description
3.424	Longitudinal free A exciton in the first excited state
3.421	Transverse free A exciton in the first excited state
3.393	Longitudinal free B exciton
3.387	Transverse free B exciton
3.382	A exciton, upper polariton branch
3.3783	Longitudinal A exciton
3.3762	Transverse A exciton
3.3750	A exciton, lower polariton branch
3.3737	Ionised donor, A exciton bound to (I4)
3.3731	Ionised donor, A exciton bound to (I5)
3.3725	Ionised donor, A exciton bound to (I6)
3.3710	Rotator state, A exciton bound to (I4)
3.3701	Rotator state, A exciton bound to (I5)
3.3692	Rotator state, A exciton bound to (I6)
3.3672	B exciton bound to neutral donor (I4)
3.3658	B exciton bound to neutral donor (I5)
3.3653	B exciton bound to neutral donor (I6)
3.3627	(I4) A exciton bound to Hydrogen-neutral donor
3.3614	(I5) A exciton bound to neutral donor
3.3608	(I6) A exciton bound to Aluminium
3.3596	(I8) A exciton bound to Gallium
3.3575	(I9) A exciton bound to Indium
3.3528	(I10)
3.3476	(I11)
3.337	(?)
3.333	A exciton bound to structural defect
3.332	(?)
3.329	TES (I4)
3.324	TES (I5)
3.321	TES (I6)
3.306	1LO Fx
3.301	Fano resonance minimum
3.109	1LO I(4-6)
3.250	1LO TES I(4-6)
3.232	2LO Fx
3.216	2LO (I4-6)
3.182	2LO TES I(4-6)
3.144	3LO I(4-6)
2.82	Zero phonon line, Cu on Zn site
2.44	Oxygen vacancy and 5LO Cu(Zn)
2.28	Oxygen interstitial
1.98	(?)

Table 2-6 Summary of all observed 4K PL emission peaks

2.5 Conclusion

Hydrothermal single crystal bulk ZnO has shown to exhibit differences in the free exciton PL emission from the zinc and oxygen polar faces. The zinc polar face shows significantly higher emission intensity than the oxygen polar face. The difference is shown to be eliminated at annealing temperatures above 600 ^{o}C.

The splitting between the A_L and A_T free excitons shows considerable variation and may count for much of the discrepancy for published transition energies in the literature. The splitting is shown to vary with annealing temperature between 1.2 and 2.5 meV. The two electron satellites for I_4, I_5 and I_6 were observed and shown to conform to Haynes rule thus confirming their nature.

The peak at 3.218 eV previously assigned to a donor-acceptor pair recombination was conclusively shown through power dependence, energy spacing and Huang Rhys intensity fits to be the 2LO phonon replica of the neutral donor bound exciton features centered around I_5 contrary to common literature assignment.

The defect level PL emission has been fitted with three Gaussians and the intensities of these peaks has been studied under conditions of increasing annealing temperature. At high temperatures a series of phonon replicas appears with a zero phonon line at 2.82 eV. These are the phonon modes of copper sitting on a zinc site in the wurtzite crystal structure, their appearance at high annealing temperatures is attributed to the outward desorption of hydrogen during the annealing process, it has been hypothesized that the presence of hydrogen in the film raises the Fermi level above a Cu related acceptor level, quenching the luminescence. To advance this theory the samples were re-annealed in a hydrogen atmosphere and the copper luminescence was shown to disappear. This experiment shows a strong correlation between copper and hydrogen in the quenching of the luminescence.

3 Investigations of zinc oxide grown by Molecular Beam Epitaxy

Much of the excitement relating to zinc oxide is a result of its UV optical properties and the potential for efficient white light LED's. The fabrication of such devices typically involves the deposition of thin films of n-type and p-type material to form a p-n junction. To fully understand the mechanisms involved in thin film epitaxial growth of zinc oxide, a growth method must be chosen that offers a high degree of control over the growth parameters. Molecular beam epitaxy is a popular choice for precisely this reason. In this chapter the influence of growth conditions and post growth treatment on film quality are discussed[88, 89], the durability of zinc oxide films under environmental conditions is examined and the temperature dependence of the photoluminescence is observed and modelled.

Attempts are made to grow p-type material and the role of auto-compensation in doping and its influence on the electrical and optical properties of doped material is considered.

3.1 PL of MBE thin films

3.1.1 The near band edge region

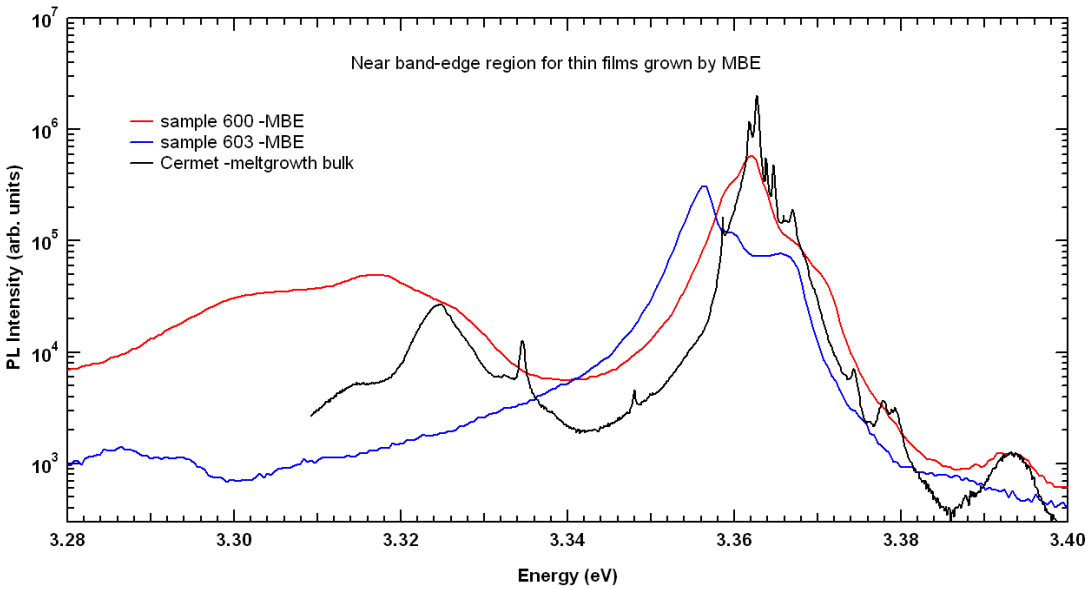

Figure 3-1 Comparison of MBE thin film and bulk crystal NBE PL at 4K

The PL of the near band edge region of MBE zinc oxide films can vary substantially depending on a variety of factors, including growth conditions, substrate type, and post growth treatment. The narrowest PL line width, measured at a temperature of 4^{o} K, of an excitonic transition measured for MBE films grown here at the University of Canterbury is 2.2 meV although line widths of as little as 1.5 meV have been reported in the literature[31]. The PL of typical MBE films grown locally are shown against a melt growth bulk sample in Figure 3-1. The spectrum is dominated by the same donor bound excitonic features typically observed in the bulk however the large line width can make individual identification of the peaks difficult. Additional difficulties include strain induced displacement of the transition energy which often results from a mismatch in the substrate lattice parameters. Films of high enough quality for the B_L-exciton at 3.392 eV to be observed have been grown locally, as seen in Figure 3-1.

3.1.2 Deep level emission spectrum

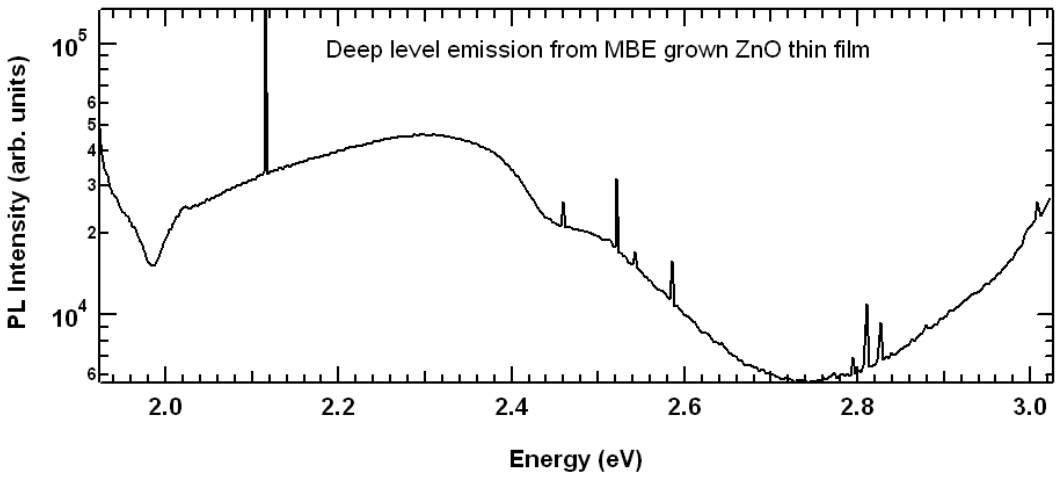

Figure 3-2 Deep level PL emission of MBE grown thin film

MBE grown zinc oxide displays similar broad deep level PL emission to that observed in bulk zinc oxide and in films grown by other methods. This deep level PL is often an indirect measure of film quality. Films with a high UV/Vis ratio in PL intensity generally have fewer defects than those with a low UV/Vis ratio. The peak emission occurs around 2.3 eV, however the broad nature of the peak makes individual identification difficult, The absorption features around 2.0 and 2.44 eV are the result of experimental artefacts and not a feature of the PL.

Some of the stray spikes seen throughout the scan are the result of cosmic rays striking the PMT while others correspond to stray plasma lines from the laser excitation source.

3.2 Effect of growth conditions on films

3.2.1 RF plasma power

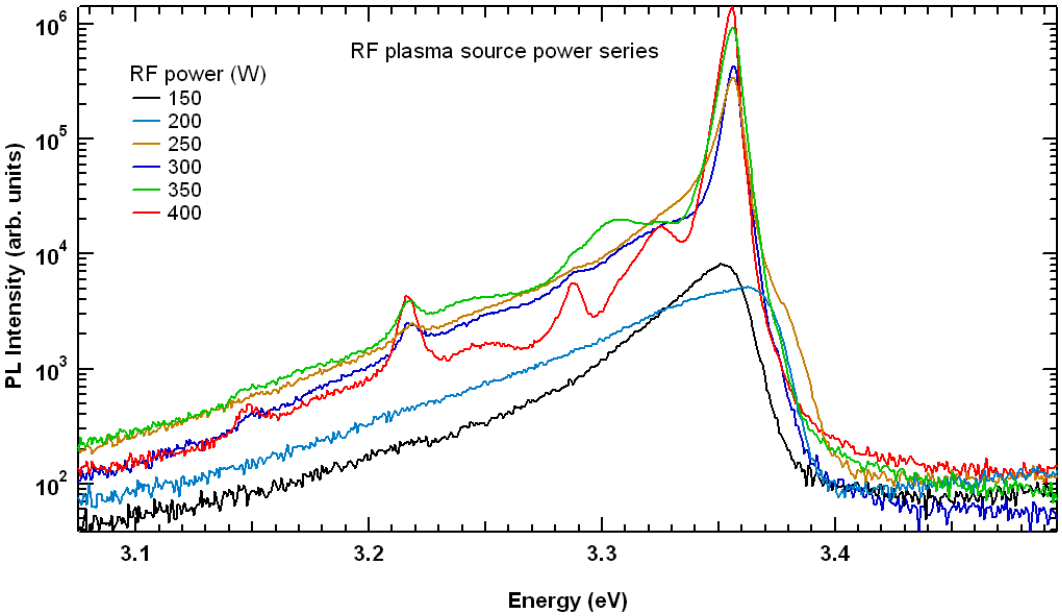

Figure 3-3 RF power dependence of NBE PL intensity – 4K

Active atomic oxygen is important for epitaxial growth of ZnO due to the large molecular binding energy of O_2. In plasma assisted MBE, the oxygen is atomised by an RF plasma generator to enhance oxygen incorporation into the film. By adjusting the RF power, the flux of the various oxygen species in the plasma coming from the generator can be altered. Optimising this flux for epitaxial growth is a crucial component of growing high quality MBE films.

A series of films was grown at increasing RF powers using an inductively coupled plasma source from Oxford Applied Research, model MDP21. The NBE PL results are displayed in Figure 3-3 and the defect level PL is available in Figure 3-5.

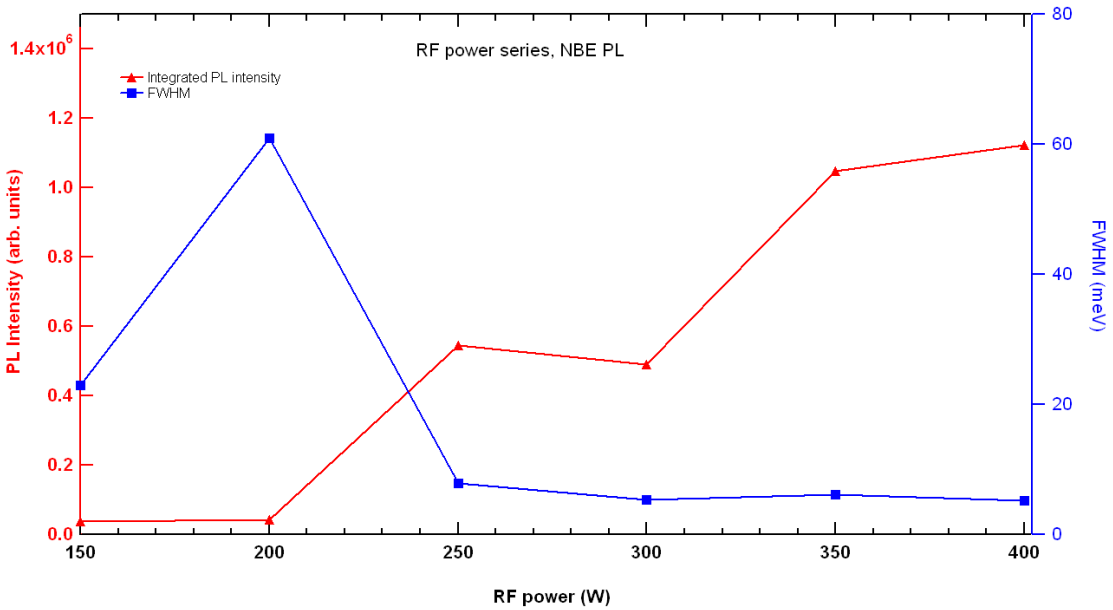

Figure 3-4 NBE line width and intensity

The integrated PL intensity of the NBE is shown in Figure 3-4 and is seen to increase almost monotonically with RF power up to 400 W. The FWHM of the PL shows a dramatic reduction when increasing the RF power from 200 W to 250 W.

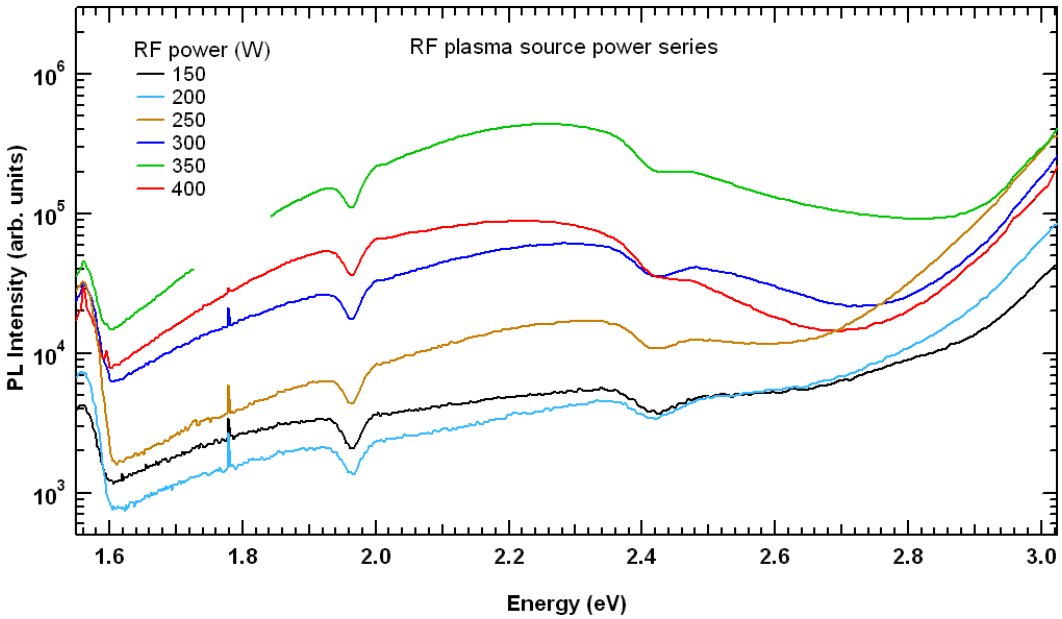

Figure 3-5 Deep level PL emission 4K – RF power dependence

The defect level emission is characteristically broad and centred around 2.2 eV. The intensity increases with RF power up until 350 Watts, at 400 Watts it shows a small decrease. The increase up to 350 Watts is likely a result of the overall increase in luminescence from the film, the decrease at 400 Watts indicates a significant improvement of the overall film quality as the decrease occurs simultaneously with an

increase in the NBE PL. This can be more clearly seen in the ratio of the peak intensities.

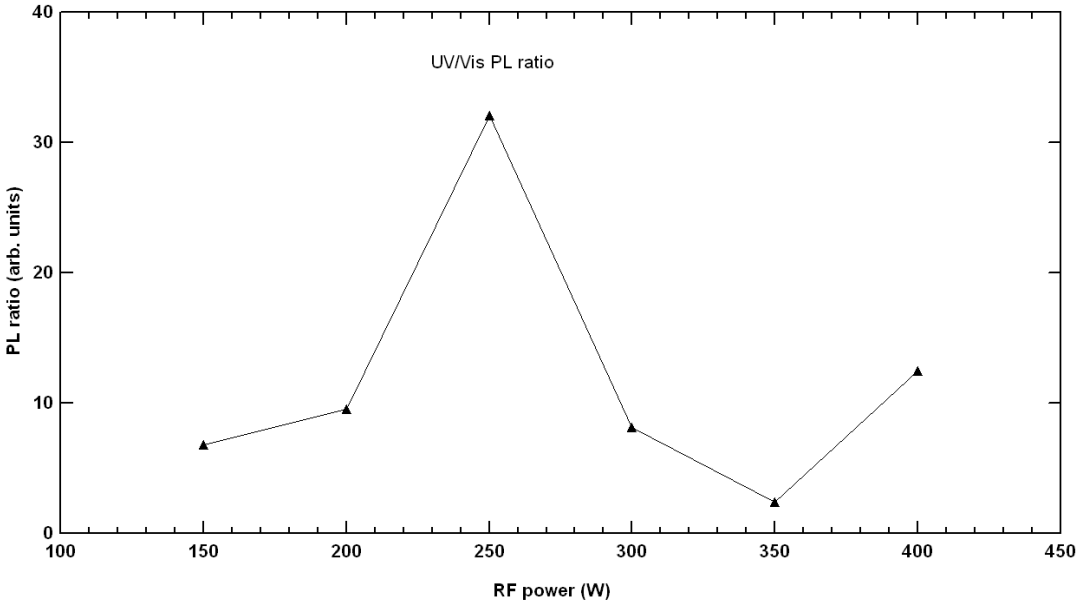

Figure 3-6 UV/Vis PL ratio at 4K

The ratio of UV (near band edge) luminescence to visible emission (Figure 3-6) is an indication of crystal quality. A high ratio indications that the material is of high quality. In this RF power series a ratio maximum is observed at 250 W although there are signs that the intensity may increase above 400 W. Although this may suggest that 250 W is the optimum RF power for growth, other factors such as overall optical emission intensity may suggest that higher plasma generator powers could be comparable.

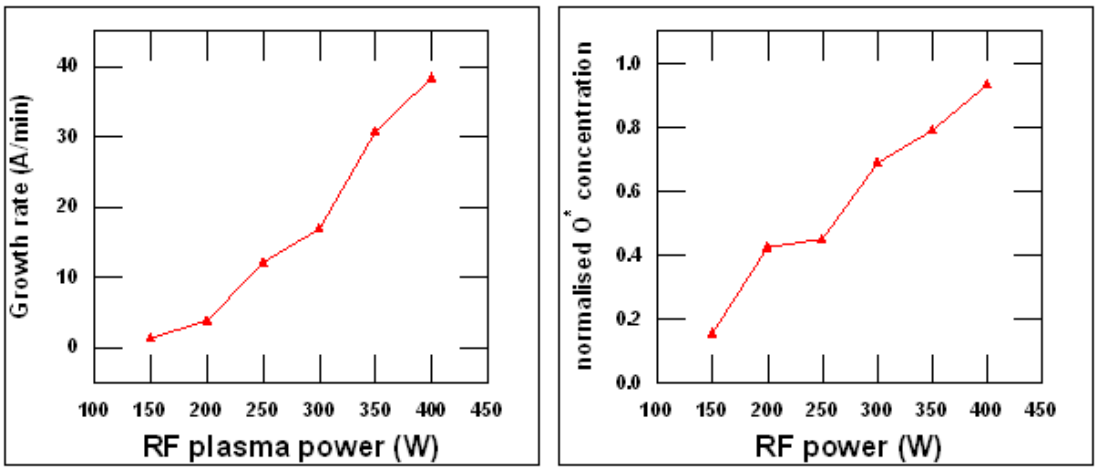

Figure 3-7 Influence of RF power on activated oxygen and growth rate

The growth rate (Figure 3-7) also increases monotonically with RF power up to 400 Watts. This is entirely consistent with results of Heo et al.[82] obtained during a

concurrent period of time. Their results extend beyond the range displayed here, to 600 Watts and show the growth rate plateaus above 400 Watts, indicating that most of the oxygen has been activated for growth or possibly that the in situ zinc flux may be bonding on the surface at its maximum allowable rate, and is no longer being limited by an inadequate supply of activated oxygen.

The Zn flux was maintained around $1.4*10^{14}$ $cm^{-2}s$ for each growth in this experiment.

3.3 Effect of buffer layers on film quality

Zinc and oxygen fluence, active oxygen species, substrate temperature are all growth parameters than can be independently changed in order to optimise film growth. The quality of the film however is still heavily limited by any lattice mismatch between zinc oxide and the growth substrate.

Sapphire is a popular choice as substrate due to its low cost and ready availability. The lattice mismatch between zinc oxide and sapphire in the most energetically favourable orientation is 17.9% and rotated by 30^o or 90^o with respect to the (0 0 0 1) sapphire basal plane[90]. One method of minimising this strain is to grow a low temperature buffer layer on the substrate using a material with a similar lattice spacing to zinc oxide. In some cases multiple buffer layers may be used[91].

3.3.1 Homoepitaxial buffer layer

In the case of a homoexpitaxial buffer layer, zinc oxide itself is used as the buffer layer material[34].

By growing the buffer layer at a low temperature, surface wetting can be maximised. A properly wetted surface shows good 2-D growth and avoids clustering and island formation. The low temperature contributes to proper wetting by reducing the mobility of the adatoms moving between multiple atomic planes. A high temperature buffer layer growth typically produces highly structured 3-D “islands” and results in increased surface roughness in the final film.

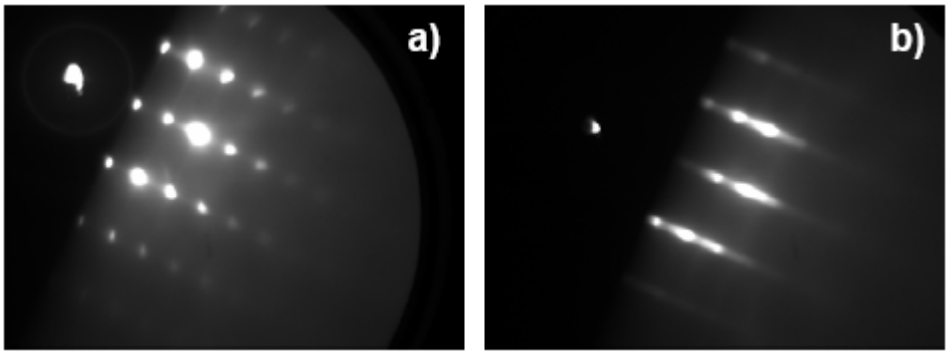

Figure 3-8 RHEED comparison – with and without LT ZnO buffer layer

These RHEED images are taken from two films grown in otherwise identical conditions. The first a) corresponds with a film grown with no buffer layer. The spotty pattern is indicative of a rough surface. The second film b) shows a film grown on a low temperature (300 ^{o}C) 50 nm thick ZnO buffer layer, the streaky pattern shows that the film has a significantly smoother surface.

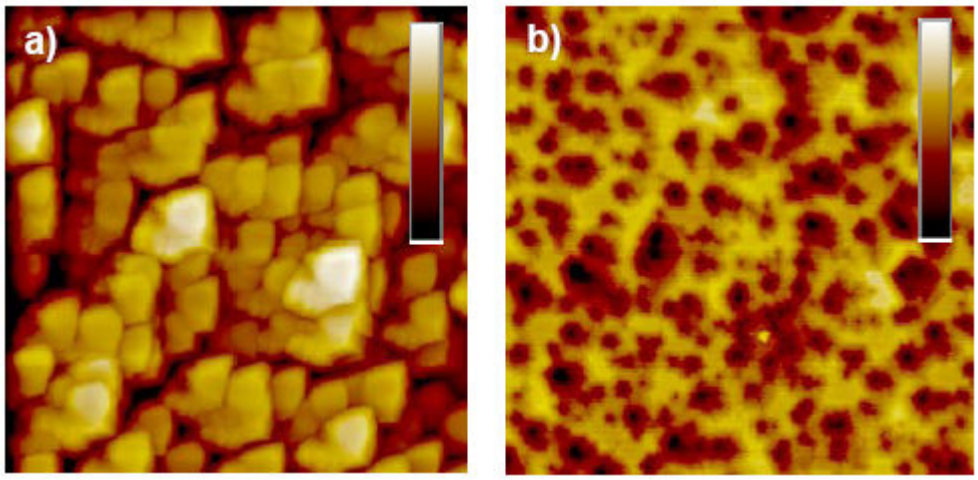

Figure 3-9 AFM comparison – with and without LT ZnO buffer layer.

AFM results show a similar pattern. The two images both show a 3 µm x 3 µm surface area however the height scale on the left corresponds to a film with no buffer layer and is shown using a colour scale of 300 nm. The film on the right is grown on a LT ZnO buffer layer is shown using a colour of 100 nm, the film grown on the homo-epitaxial buffer layer clearly displays smoother surface morphology.

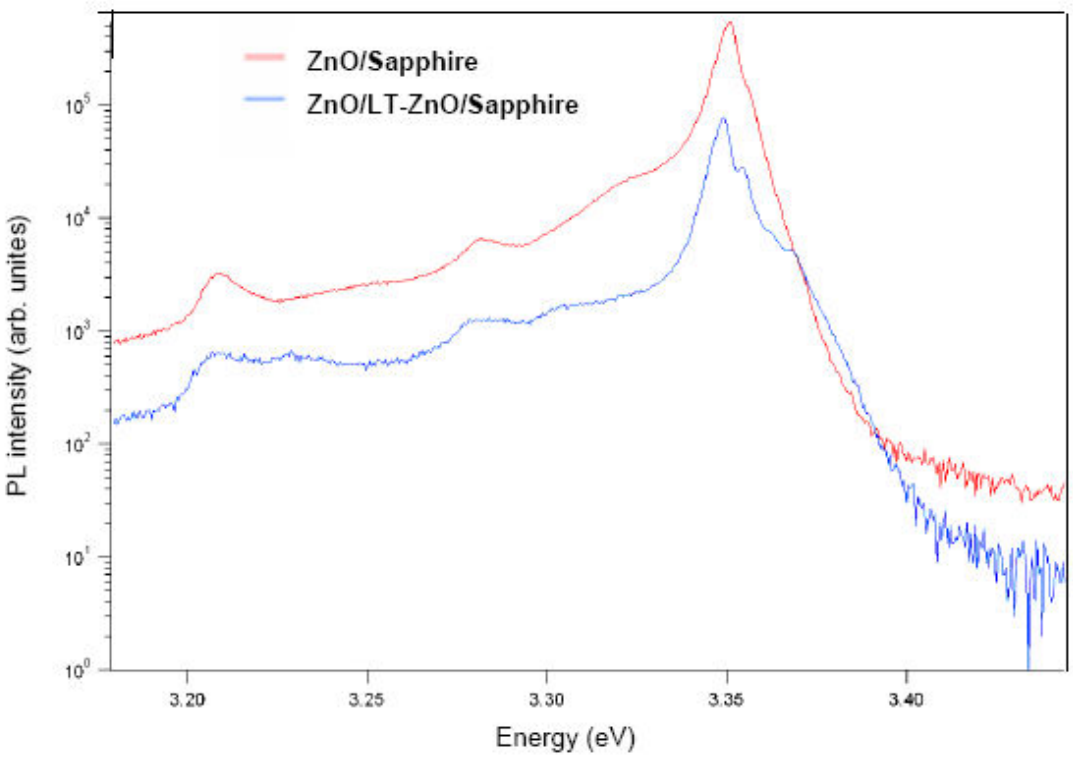

Figure 3-10 PL comparison – with and without LT ZnO buffer layer

Finally, the PL in Figure 3-10 confirms the results. The ZnO grown directly on sapphire shows less structure and a broader line width in the NBE when compared to the film grown on a LT buffer layer. The free exciton and individual donor bound exciton transitions are clearly distinguishable. These results show that a LT ZnO buffer layer can be used to improve film quality of zinc oxide on a sapphire substrate.

3.3.2 MgO

While the use of low temperature ZnO buffer layers has been shown to improve overall film quality, there still remains room for improvement.

MgO is a material that is chemically compatible with both ZnO and sapphire and with only a 9% lattice mismatch with sapphire, offers an excellent intermediate layer on which to grow ZnO[92]. In this experiment MgO is trialled as a buffer to improve the optical quality of ZnO films grown by PAMBE.

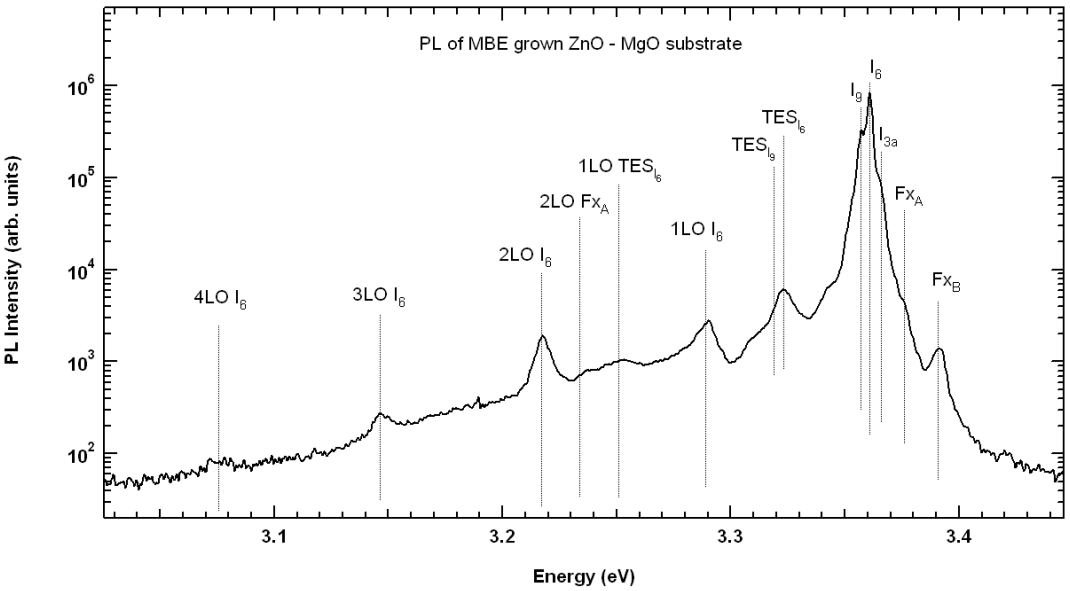

Figure 3-11 3K PL of ZnO grown on MgO buffer layer

The PL results for a 1.2 μm thick ZnO film grown on a 1 nm thick MgO buffer layer are exceptional. 1 nm was found to be the upper threshold for a MgO buffer layer before surface roughening was observed, as indicated by in-situ RHEED images during growth[93]. The film was grown at an RF power of 400 W, and oxygen flow of 1.6 sccm and a substrate temperature of 650 ^{o}C. The narrow line width (<3 meV) of the neutral donor peaks, the strength of the LO phonon modes, the TES modes, the Fano absorption line and the presence of both Fx_A and Fx_B are all indications that the film is approaching the quality of bulk single crystal. These results are also supported further in the PhD thesis of William C. T. Lee[93] by XRD. From this we can conclude that MgO is a most suitable buffer layer for the growth of devices requiring high crystal quality. The presence of I_6 and I_9 as the dominant emission peaks instead of I_5, which is more normally observed in hydrothermally grown bulk, is a result of the different growth environment. I_6 and I_9 correspond to aluminium and gallium impurities respectively, while I_5 remains as yet unidentified[9]. Further improvements could perhaps be introduced by utilising a low temperature ZnO buffer layer atop the MgO.

3.4 Flux stoichiometry

The growth of stoichiometric zinc oxide is a complex procedure and is not necessarily the result of stoichiometric zinc and oxygen flux during the growth. The precise

requirements are still the subject of debate as a result of conflicting reports[94-96]. In this section films are grown under zinc rich, oxygen rich and stoichiometric conditions. The resulting films are analysed using PL and SEM measurement techniques.

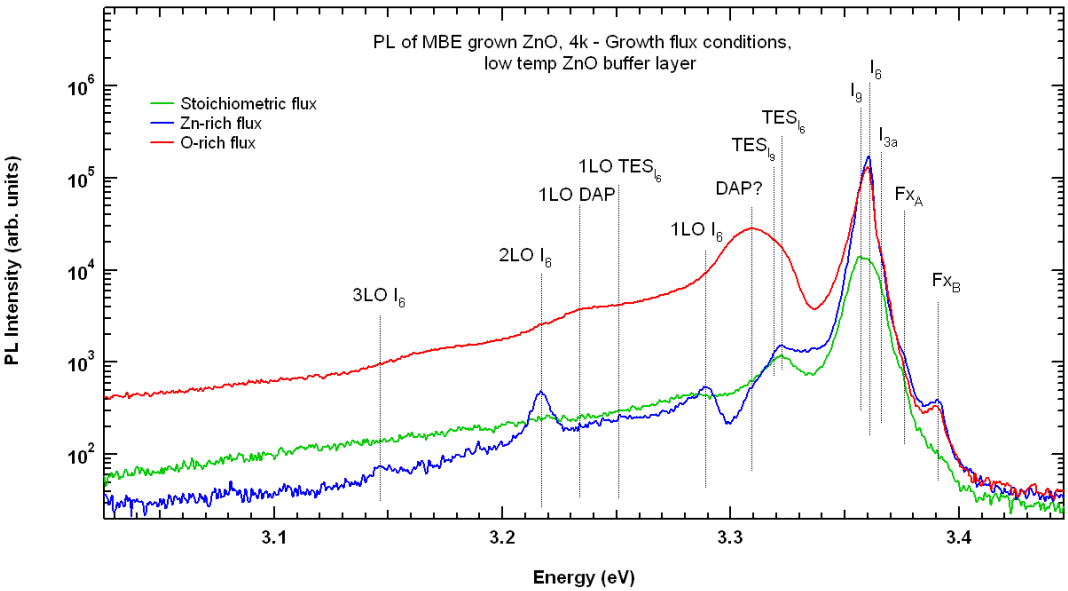

Figure 3-12 Influence of growth stoichiometry on NBE PL

The PL of all three films is dominated by the neutral donor bound excitons in the near band edge region, however the differences between them allow for interesting discussion. If we consider the high energy side of the spectrum first and move through to the low energy side we observe many differences in between.

The first thing of note is the presence of the B-exciton in the films grown under both Zn and O rich conditions. The B-exciton is frequently not observed in the PL of ZnO and its presence is an indication that the film is of high quality. The absence of the B-exciton from the film grown under stoichiometric conditions indicates that the film is likely to be highly defected.

The D^0X features correlate most closely with Al and In contamination of the film, as has come to be expected with films grown under these conditions. The source of the dopants is either a result of residual traces remaining in the chamber from previous growths and from the indium paste used to affix the substrate to the heater, or from traces in the starting material.

The film grown under Zn rich conditions shows the highest intensity and narrowest line width suggesting that it is the film with the highest crystal quality, the film grown

under O-rich conditions also shows good line width while the film grown under stoichiometric conditions once again shows evidence of poor crystallinity.

Perhaps most interestingly the film grown under O-rich conditions shows a broad emission peak centred around 3.1 eV which places it in the region frequently associated with donor-acceptor pair transitions[17], this origin could be supported by observing the laser power dependence of the PL emission intensity at 3.3 eV.

Due to the relative flux ratio during growth this indicates that either oxygen interstitials or zinc vacancies may act as acceptors in a DAP complex.

The Fano absorption line at 3.3 eV is perhaps one of the most direct measures of crystal quality as determined by the PL[63, 64]. It is present only in films with narrow line widths as it requires discrete energy levels (the 1LO of the D^0X to couple with a continuous background - the tail of the band edge).

The sharpness of this absorption line and also of the LO phonon replicas of the film grown under Zn rich conditions are strong arguments for this film being the most stoichiometric and possessing the better crystal structure.

3.5 Annealing trials

Zinc oxide films grown by methods such as MBE are often polycrystalline or display a high concentration of small crystal domains. These domains add a degree of inhomogeneity to the crystal that can negatively impact the electrical properties. In addition many impurities may be introduced into the crystal during growth. One way of treating both problems is to anneal the films after growth has been completed. In this section films are annealed over a range of times in order to determine the influence of annealing time on the optical quality of the material. The annealing temperature is also varied in order to determine its effect on the final quality of the films.

3.5.1 Annealing time

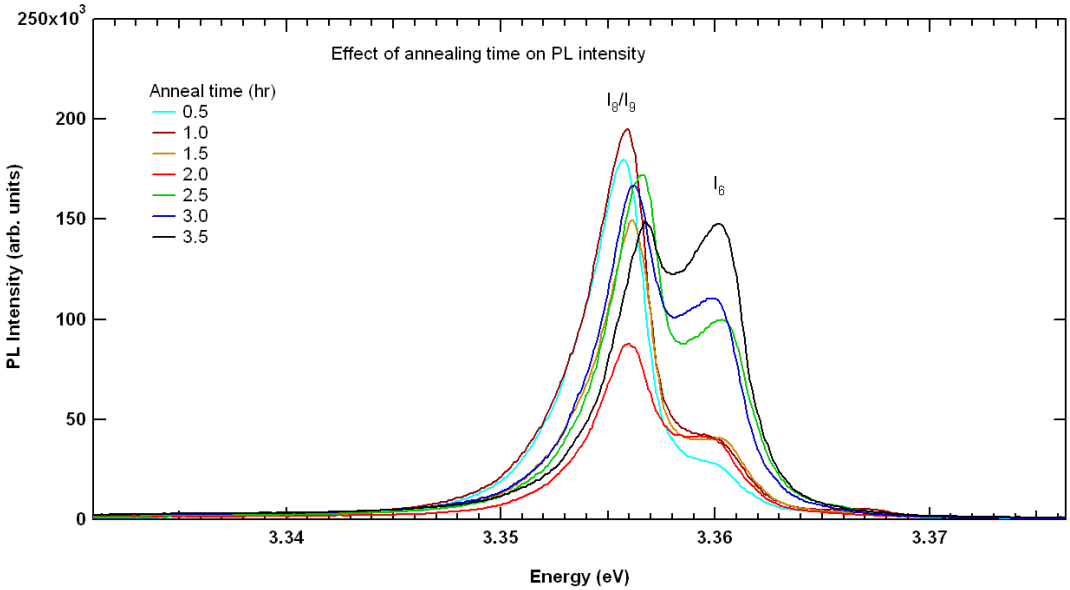

Figure 3-13 Influence of annealing time on NBE PL – 4K

An MBE grown film annealed for increasing periods of time (Figure 3-13) displays a clear evolution of the relative peak intensity between the two dominant features. One located near 3.360 eV, most likely I_6 (Al) and the second in the region of 3.356, most likely I8 or I9 (Ga, In). By plotting the intensity of the two dominant peaks their behavior under annealing conditions is observed. The peak labeled I_8 can be seen in Figure 3-13 to generally decrease in intensity with an increase in annealing time (with a minimum at 2 hours) while I_6 clearly increases in intensity. A quick glance at the ratio of the two peaks (to normalize for variations - Figure 3-14) shows the ratio shifting increasingly in favour of the I_6 peak. The sum of the peak intensities increases with time showing that even after 3.5 hours an equilibrium configuration of the film has not been attained.

The decrease in the I_8 peak may be a result of Ga being driven out of the film during the annealing process.

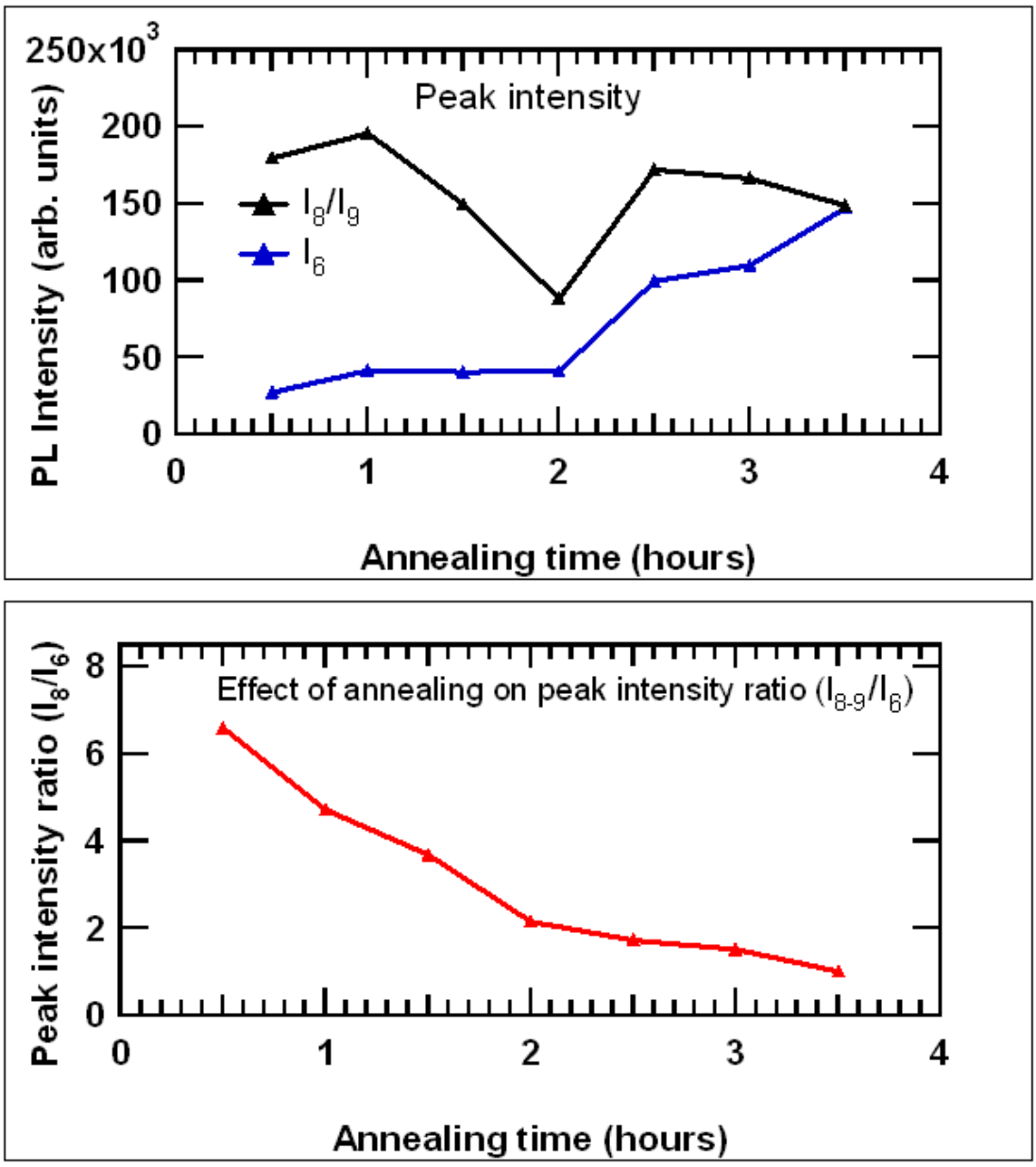

Figure 3-14 Influence of annealing time on NBE PL – processed data

3.5.2 Annealing temperature

In addition to the annealing time, temperature plays a role in process. In this experiment samples were annealed at two different temperatures and compared to the unannealed sample in order to determine the effect of annealing on MBE grown films. The samples were annealed in air for one hour.

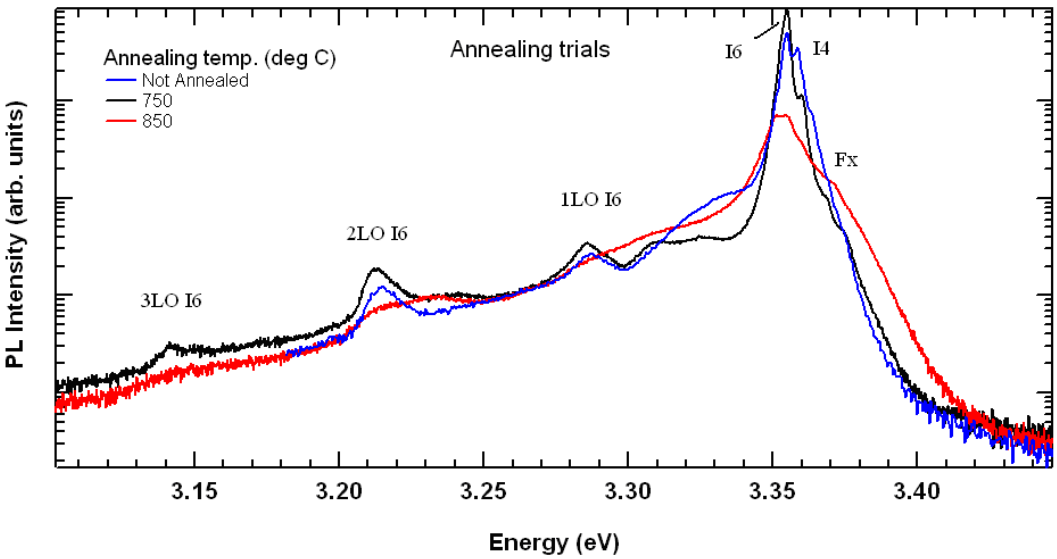

Figure 3-15 Effect of annealing temperature on NBE PL

Figure 3-15 shows the PL results for the three films. One film was unannealed, and the remaining two were annealed at temperatures of 750 ^{o}C and at 850 ^{o}C respectively.

The results show a slight improvement in the film annealed at 750 – an increase in intensity, a narrow line width (2.3 meV) and a reduction of what is believed to be the I_4 line corresponding to hydrogen impurities. There is also a sharpening of the LO phonon features and the appearance of the Fano absorption line. The absorption line is a consequence of quantum mechanical coupling between a discrete energy state and a continuous background, it is present only when the line width is low enough to be classified as a "discrete energy level" and as such can be used as an indirect measure of quality.

In the film annealed at 850 ^{o}C I_5 and I_6 become the dominant features and the free exciton shows an increase in intensity. However overall it shows reduced luminescence, increased FWHM and an overall degradation in film quality.

While not conclusive, the results suggest that annealing temperatures lower than 850 ^{o}C are preferable.

3.6 Nitrogen doping for P-type material

Nitrogen has been theorised as a suitable choice for P-type doping in ZnO oxide and frequent attempts have been made to incorporate nitrogen into films during growth[26, 38, 97].

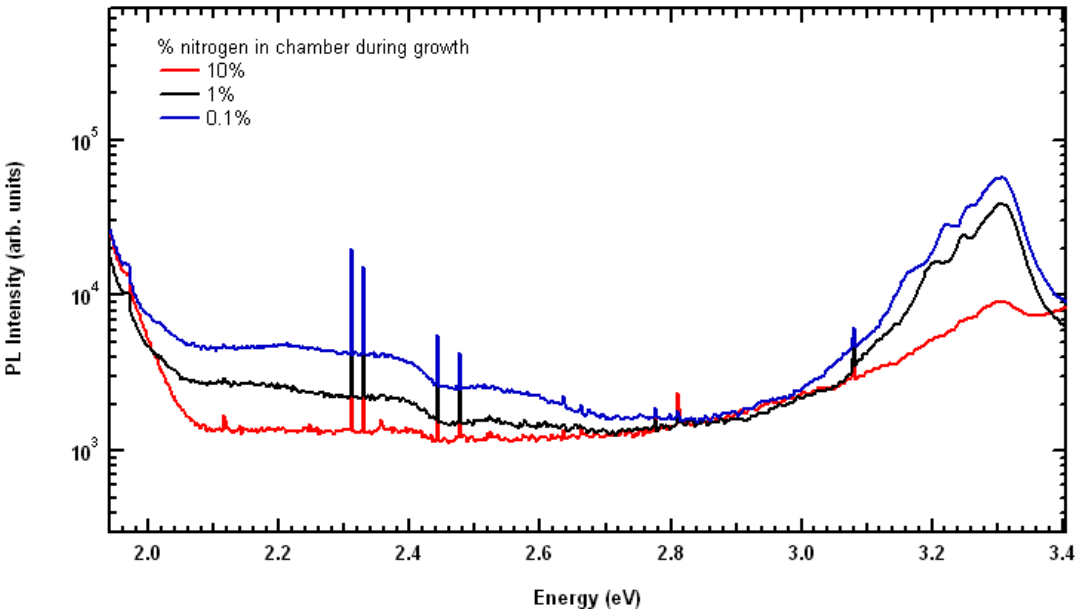

Figure 3-16 Effect of nitrogen flux during growth - PL

In order to better understand the effect of ambient nitrogen content during growth, a series of films was grown with increasing concentrations of nitrogen present. The result in Figure 3-16 show the detrimental effect the nitrogen incorporation has on the PL efficiency of ZnO films. Plotting the PL intensity against the nitrogen content during growth shows this clearly (Figure 3-17).

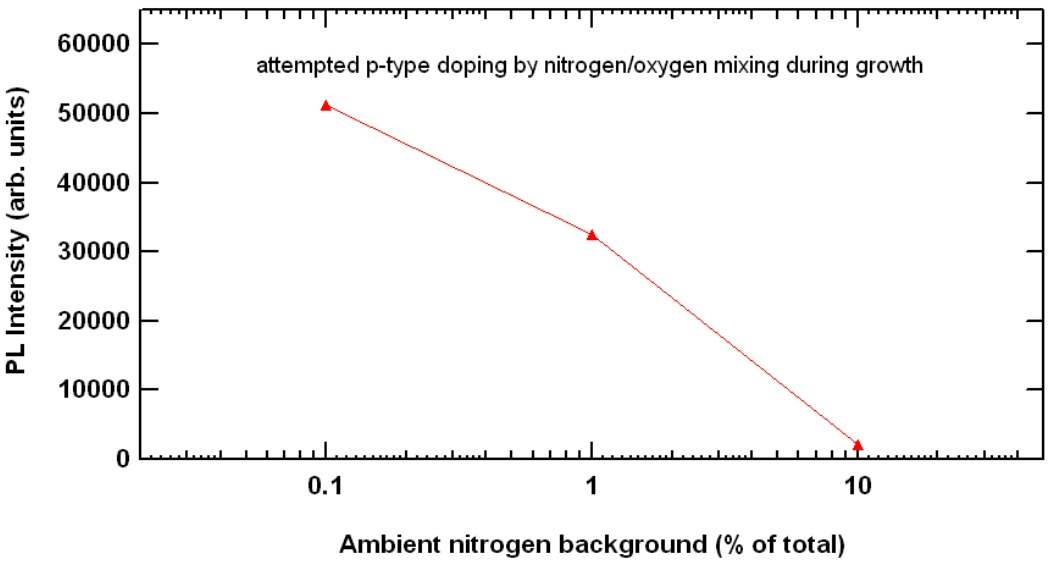

Figure 3-17 PL intensity reduced by incorporated nitrogen

A film was grown in house with nitrogen gas introduced into the vacuum chamber during growth. The resultant film was analysed for sample uniformity by means of spatially resolved PL on a mm scale. PL scans were made at mm spaced steps across the film and the PL signals were compared.

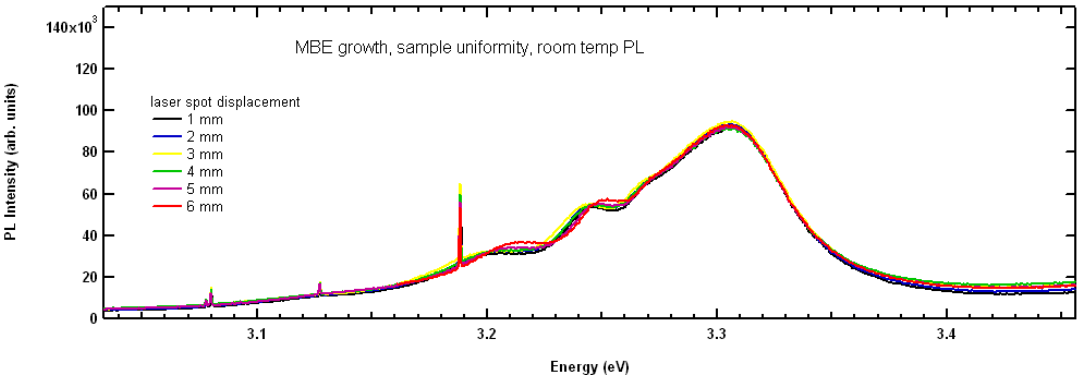

Figure 3-18 Thin film doped with nitrogen – spatial variance in room temp PL

Figure 3-18 shows the PL spectra of an MBE sample taken at various positions across the film. The results show a high degree of similarity and intensity across a 6 mm range on the sample which suggests that MBE can readily achieve an excellent degree of macroscopic uniformity over a large surface area, even with significant nitrogen incorporation.

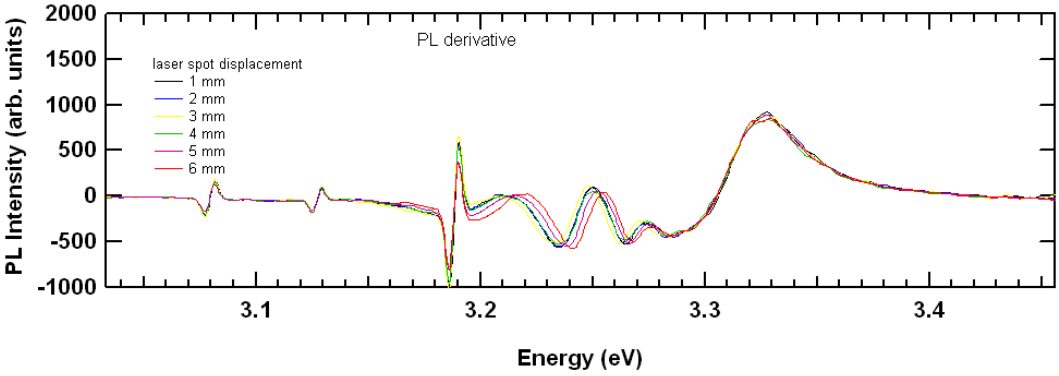

Figure 3-19 Extracting change in peak position from room temp PL

However although the peak PL intensity at 3.31 eV, tentatively assigned to excitons bound to a defect, remains constant in position and intensity, a noticeable difference is observed for the PL emissions observed around 3.246 and 3.205 eV. To track the change in peak position across the sample, the PL signal has been differentiated, peak

positions can be estimated from the x-intercept positions. The signal has been smoothed to remove the noise, tracking the laser plasma lines ensures that the peak positions are not influenced by the smoothing process.

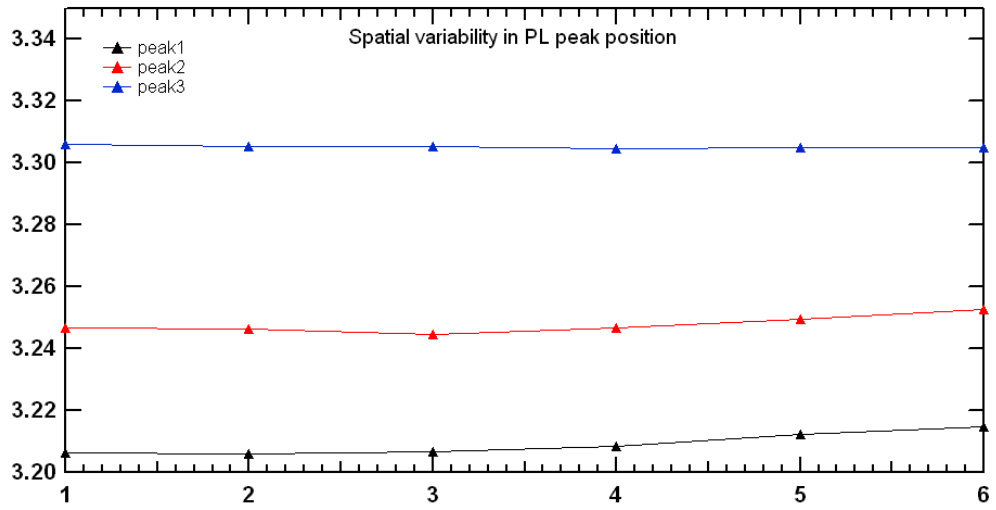

Figure 3-20 Change in PL peak positions across sample

Plotting the peak position against spatial displacement shows that the dominant peak (3) remains constant in energy, regardless of which part of the film is examined however both lower energy peaks (1, 2) show an increase in energy for x > 3 mm. If the shift were strain induced it should affect all peaks equally. However if the peaks are assigned to donor-acceptor pair transitions, where the acceptors are introduced through nitrogen doping during growth, then an increase in the concentration of the majority donors would result in an apparent blue shift of the observed DAP peak positions due to a decrease in the average distance between the donor and acceptor centres.

$$E_{DA} = (Eg - E_A - E_D) + \varepsilon e/r$$

Where r is the average distance between the donor and acceptor in a DAP, e is the electron unit charge and ε is the dielectric constant of the material.

The energy of 3.246 eV for the DAP (peak 2) closely matches that of 3.248 eV found by Park et al[98] for nitrogen doped acceptors in ZnO. The discrepancy in energy can be ascribed to a difference in carrier concentration. Further tests involving laser

excitation power dependent measurements of the peak PL energy could further support these results.

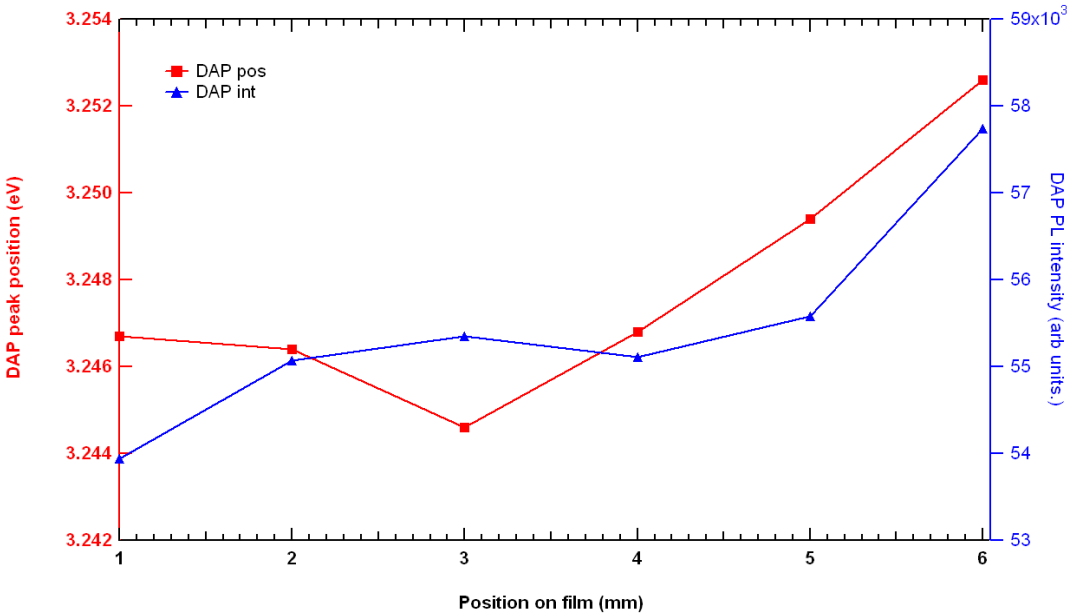

Figure 3-21 Peak intensity and position across sample

One of the primary causes assigned to the difficulty of growing P-type ZnO has been the tendency towards auto-compensation of the material in response to doping. That is to say, when an acceptor impurity such as nitrogen is introduced into the lattice, a compensatory defect is created which produces an additional donor electron, for this reason acceptors can never be the dominant carrier. Since it is clear that increasing the concentration of the majority carrier should blue shift a DAP peak, and increasing the minority carrier should increase the intensity of a DAP peak, then for auto-compensation to occur, a simultaneous blue shift and intensity increase should be observed when the sample volume is moved from a lightly doped to a more heavily doped section of the material. In Figure 3-21, by plotting both the peak intensity and peak position together we can see that this is clearly the case. From this example we present experimental evidence from the PL that auto-compensation is indeed occurring in films doped with nitrogen. How this effect might be avoided is as yet, unknown and remains a major obstacle to the successful reliable growth of p-type ZnO.

3.7 Temperature dependent PL

At low temperatures the near band edge luminescence is usually dominated by neutral donor bound excitons. As the temperature is increased these excitons are freed from their neutral donors and the emission peak associated with the transition shows a subsequent decrease. By comparing how the PL intensity of the donor bound exciton peak changes as a function of temperature, its *activation* energy can be calculated. The binding energy of an exciton to a donor is known as the *localisation* energy. This energy is typically around 14-15 meV, knowledge of this can be used to confirm the identity PL emission peaks in samples grown by methods such as MBE where the broad line-width and strain induced energy shifts often make individual identification difficult. In this experiment the activation energy is calculated for the dominant emission peak in a high quality MBE grown sample. The calculation is performed using an Arrhenius fit with two modes of decay.

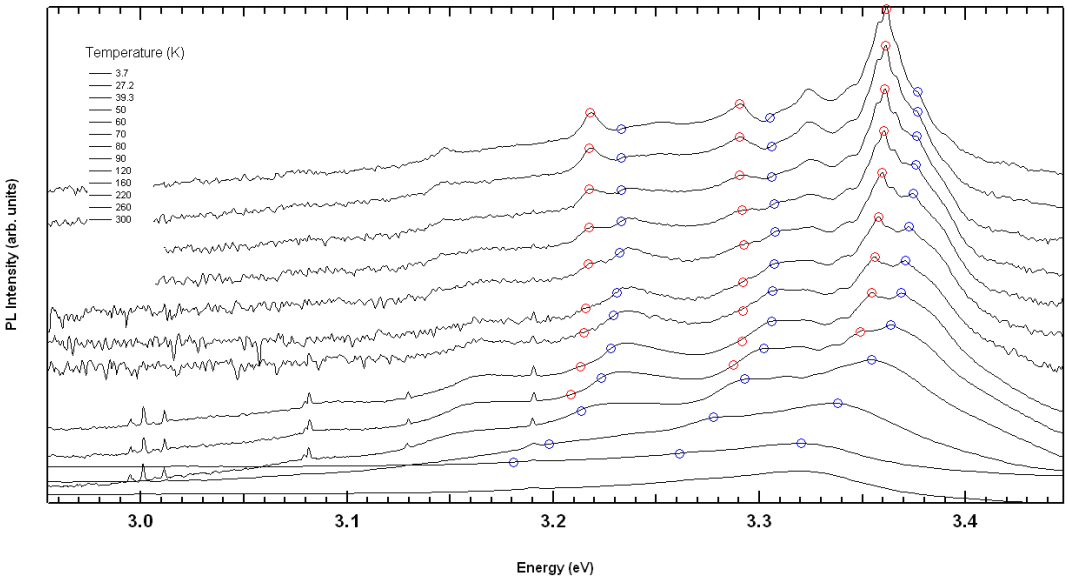

Figure 3-22 Temperature dependent PL - tracking peak position with increasing temperature

The temperature dependent PL is displayed with an offset to better illustrate the evolution of the emission spectrum as the temperature is increased. The decrease in intensity and the red-shift of the emission peaks are readily apparent.

The zero phonon lines (ZPL's) of the free exciton (Fx_A) and dominant neutral bound donor (I_5) around 3.36 eV are marked with blue and red identifiers respectively. The first and second phonon replica position are calculated and mapped onto the scans.

The LO phonon assisted lines of I_5 behave as expected however those of the Fx_A appear to predict a peak position at a lower energy than what is observed. An explanation for this is the increasing contribution of the free B exciton (Fx_B) as the temperature is increased. The net combination of A and B free excitons would result in an observed emission peak at an energy above that of the phonon assisted Fx_A lines. This is evidence of the increased role of the B exciton at higher temperatures.

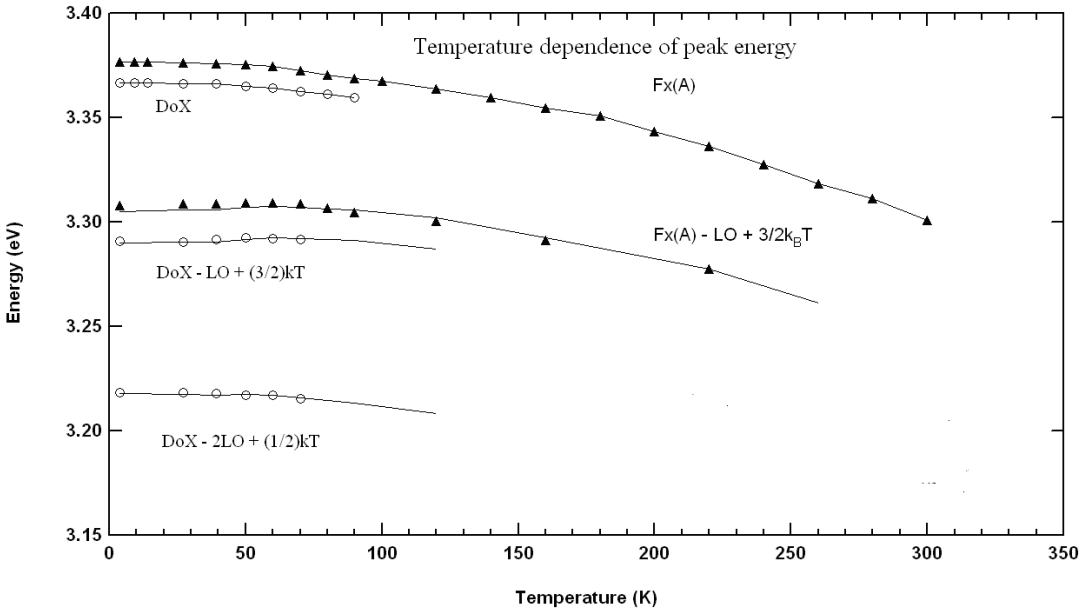

Figure 3-23 Observed and expected peak positions

The energies of the Fx_A and I_5 emission peaks are plotted against temperature in Figure 3-23 to better illustrate the point. The markers correspond to the observed peak positions while the solid lines are the expected peak positions. The donor bound exciton I_5 behaves as expected[99].

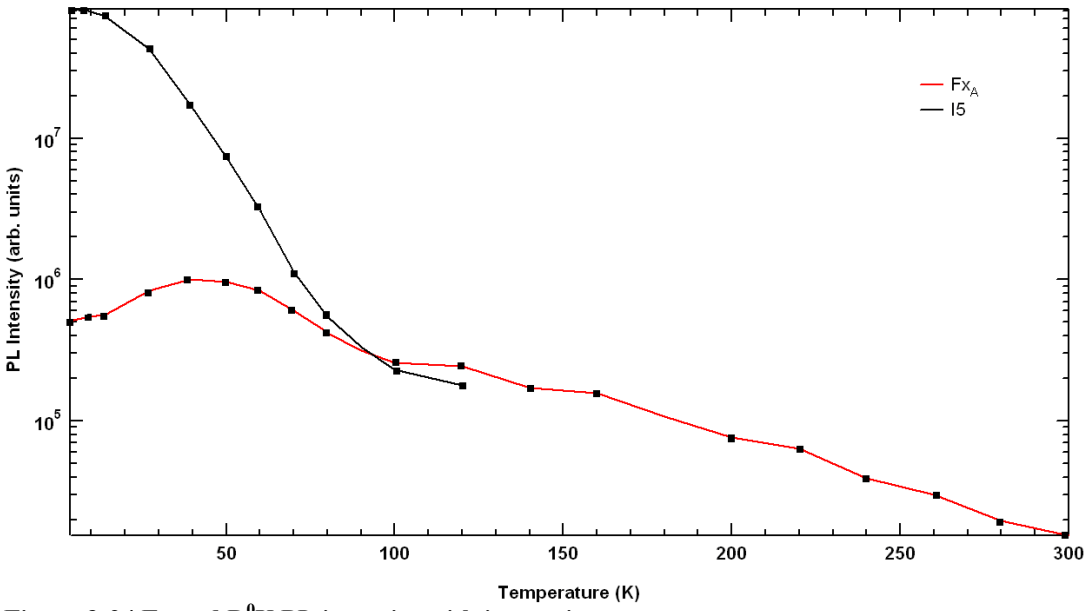

Figure 3-24 Fx and D^0X PL intensity with increasing temperature

Consider now the temperature dependence of the PL intensity. At low temperatures the neutral donor bound exciton I_5 is clearly dominant over the free exciton. As the temperature is increased from 4 K to 50 K the intensity of the Fx increases at the expense of the bound exciton. This is a clear indication that a portion of the bound excitons are being thermalised to free excitons before recombination occurs. At a temperature of around 90 K the two emission peaks have reached parity and above this temperature the free exciton comes to dominate the PL spectrum. Above 120 K the emission peak of the donor bound excitons are no longer distinguishable, the result of a combination of quenching and thermal broadening. By fitting the intensity of the bound exciton as a function of temperature the activation energy of the exciton to the donor can be calculated, this energy is approximately the binding energy of the free exciton to the neutral donor (localisation energy).

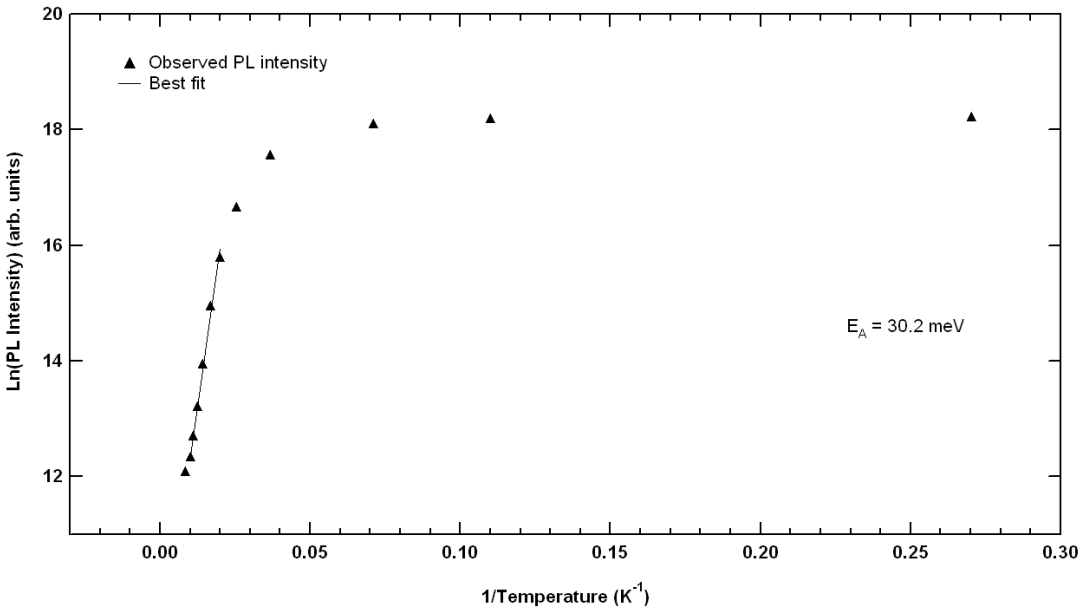

Figure 3-25 Calculating activation energy – simplistic approach

In its simplest form the intensity of the emission peak as a function of temperature (T) can be described by a function of the form

$$I(T) = \frac{I(0)}{1 + Ae^{-\frac{E_A}{kT}}}$$

Where A is a dimensionless free fitting parameter, E_A is the activation energy, T is the sample temperature and k is the Boltzmann constant.

By making some rough mathematical approximations, the gradient of a straight line fit to the log of the intensity against the inverse of the high temperature data should be proportional to the activation energy by the Boltzmann constant. This method is considered suitable for approximate calculations made without the benefit of complex fitting algorithms, however the accuracy suffers due to often large uncertainties in the PL intensity of the high temperature data.

This fit is performed in Figure 3-25 and from it an activation energy of 30.2 meV is calculated. This simple linear fit is heavily weighted towards the high temperature data (small 1/T) and as such is less sensitive to low activation energies.

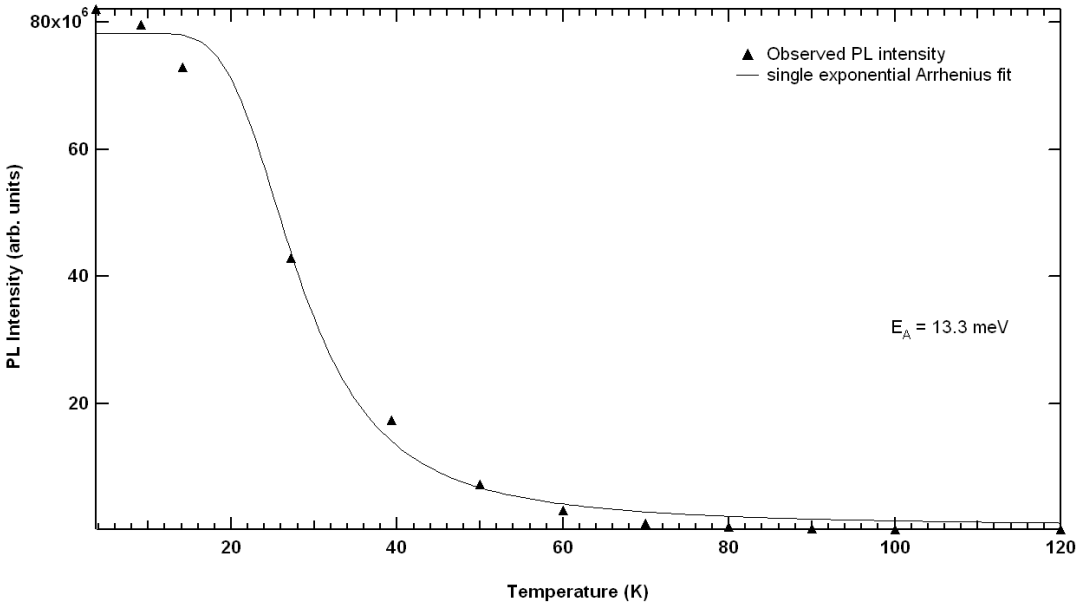

Figure 3-26 Fitting temperature dependant PL with single exponential Arrhenius

A more accurate fitting method is to simply fit the data using the complete equation. This is done in

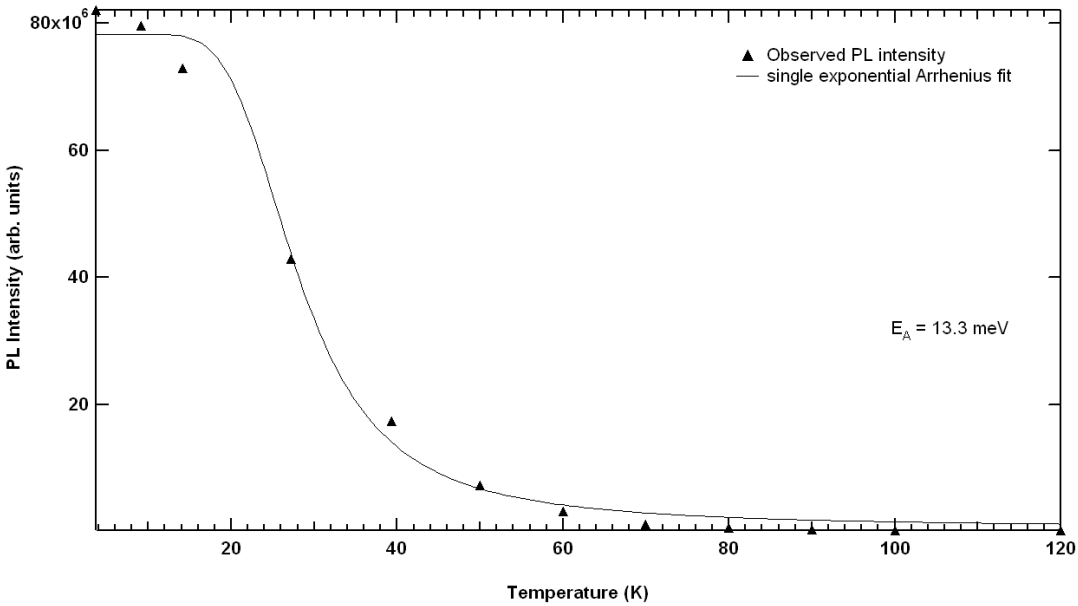

Figure 3-26 and an activation energy of 13.3 meV is obtained. The result is close to that of the expected localisation energy, however in many regions the fit remains poor.

With this in mind a second exponential decay term is introduced and the data is fitted to the function

$$I(T) = \frac{I(0)}{1 + Ae^{-\frac{E_A}{kT}} + Be^{-\frac{E_B}{kT}}}$$

With E_B being a second activation energy, corresponding to a secondary mode of decay for the donor bound excitons.

Performing the fit with two activation energies in Figure 3-27 returns energies of 30.7 and 6.4 meV. The high energy term is close to that obtained in the linear fit method and illustrates how the weighting of that method favours larger activation energies. This activation energy may correspond to the donor binding energy (the energy with which the donor electron is bound to the neutral donor) of around 50 meV while the low energy term of 6.4 meV corresponds to that of localisation energy (the energy with which the exciton is bound to the neutral donor) of 15 meV. The poor agreement may be a result of systematic errors in obtaining the PL intensity of the peak emission through fitting, including averaging of the data from overlapping emission peaks, something which is a common problem when fitting the near band edge PL of zinc oxide. The fit is further complicated by a loss of peak resolution at temperatures that are still below the activation energies. To maximise accuracy it is ideal to have PL data at sample temperatures corresponding to several times the activation energy, however due to a loss of resolution at those temperatures this remains largely impossible for zinc oxide.

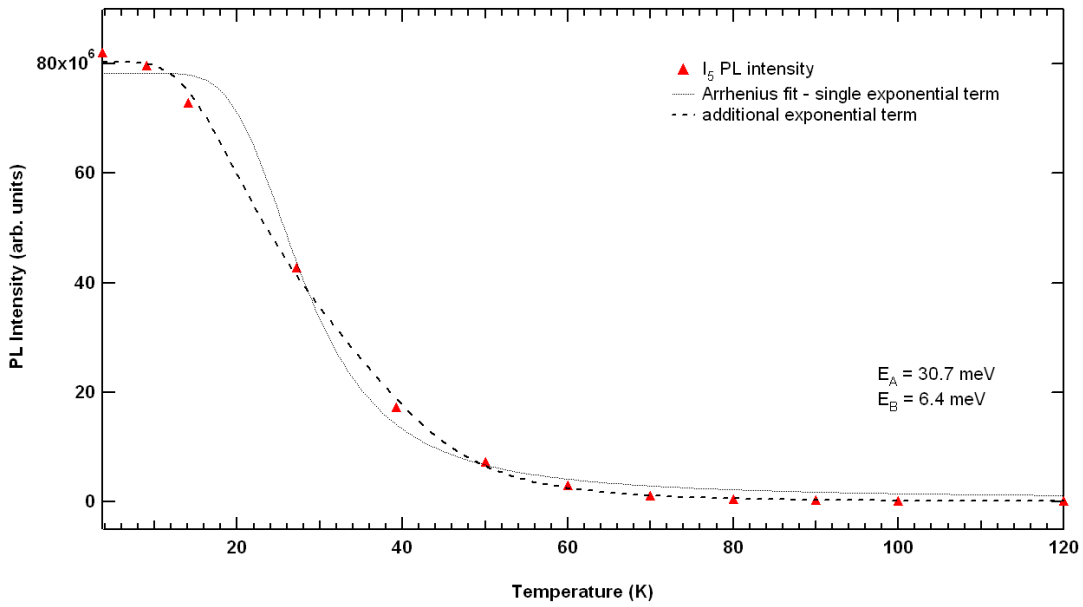

Figure 3-27 Fitting temperature dependant PL with double exponential Arrhenius

3.8 Film durability

Most semiconductor devices are designed to operate with the properties they are established with during, or immediately after, growth. Any long term drift in these properties will usually prove detrimental to the operation of the device. When most consumer devices are expected to have lifetimes measuring in years it is important to know the long term behaviour of the material under various operating conditions.

In this experiment a film of MBE grown zinc oxide, kept in air, at room temperature, was repeatedly re-examined over a period of 9 months in order to observe any long term changes in the optical luminescence that might hint at changes in the basic electrical properties.

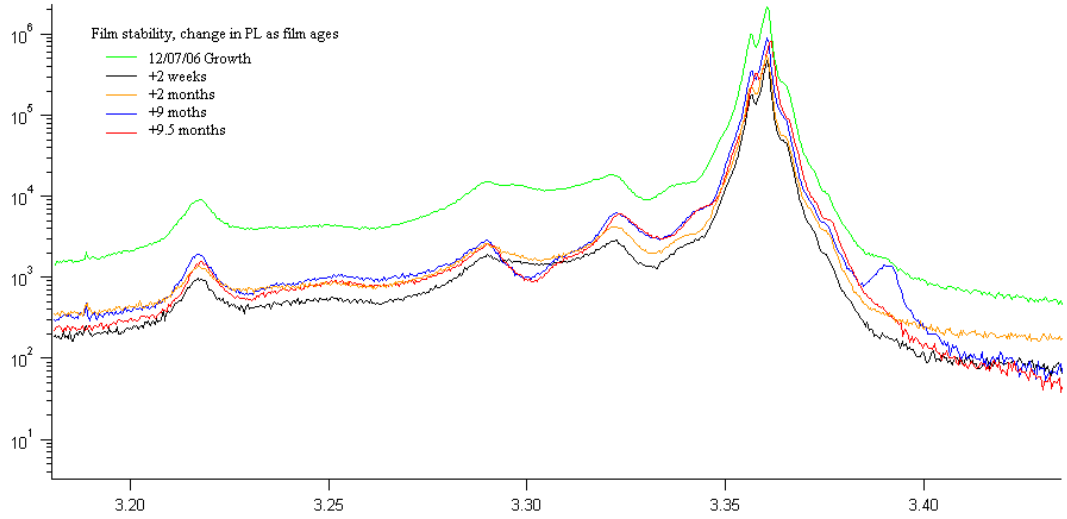

Figure 3-28 Film stability

Figure 3-28 shows the PL of the film measured in the days immediately following growth and in subsequent months. Overall the film shows good uniformity over time. There is no significant shift in the bandgap that might indicate relaxation of the lattice, no obvious new PL features that would indicate absorption of dopants from the atmosphere and no significant broadening of the PL features that would suggest large scale surface reconstruction as a result of reacting with the air.

The emission peak at 3.385 eV seen in the blue line is thought to be the B-exciton and has been observed in other high quality films, although the reason for its intermittent appearance is currently unknown.

From this we can conclude that zinc oxide is stable in air at room temperature without the need for capping layers or special protection. This is a positive result for zinc oxide based devices.

3.9 Conclusion

MBE films with line widths as low as 2.2 meV were grown by plasma assisted molecular beam epitaxy on an MgO buffer layer, although most films showed line widths closer to 5 meV.

Peaks associated with Ga, In and Al were frequently identified in varying concentrations across a large number of films. The films were shown to be relatively stable over an extended period of time which is promising for future device implementation.

The power supplied to the RF plasma generator is an important parameter in the growth of MBE ZnO. Optimum power levels were found between 375 and 400 Watts.

Annealing the films at increasing temperatures had the effect of reducing the intensity of the emission associated with Ga while at the same time increasing the relative intensity of the emission associated with Al.

Attempts at p-type doping were made by incorporating nitrogen during growth. It was found that nitrogen incorporation had a deleterious effect on the optical quality of the material. Although no PL peaks easily identified as coming from acceptors were observed, indications of donor-acceptor pairs suggest that nitrogen has successfully been incorporated into the films. Variation in the DAP peak position suggest that donor and acceptor levels varied in concentration across 10 mm^2 surface.

The activation energy of a dominant neutral donor bound exciton I_5 is calculated to be 30.7 meV with a secondary activation energy of 6.4 meV also observed

4 Optical characterisation of sputtered zinc oxide films

Zinc oxide is an excellent candidate for piezoelectric devices[100-102]. To maximise the piezo electric potential for device application it needs to have high resistivity[103] and a uniformly aligned crystal orientation. Sputtering is a relatively mature growth method commonly known for its ease of use, wide range of suitable substrates[104-108] and polycrystalline film structure. Films are typically highly resistive[109, 110], and growth occurs with the c-axis normal to the substrate surface[111-114]. For this reason it is an ideal candidate for growing piezo electric films. In this chapter two sputtering techniques are used by to grow zinc oxide films and the results compared and contrasted in a collaboration with Leo Schuler of the electrical engineering department at the University of Canterbury to determine the optimum growth method for maximising piezo and optical properties. Post growth treatment methods are then considered to further optimise these properties and a wide variety of common substrates are tested to determine how readily optical quality films can be grown on a range of different materials. Finally a two layer super structure is attempted with a highly piezoelectric surface layer grown on top of an optically active buffer layer.

4.1 DC vs RF sputtered films

Two zinc oxide thin films were grown to a thickness of 500 nm on glass by RF and -DC sputtering in identical geometric arrangements[115]. The target-substrate distance was 110 mm and the background oxygen pressure was kept constant at 1.2×10^{-2} mbar. The DC film was sputtered under reactive conditions at 250W using a 99.995% purity zinc target, a reactive O_2 flow rate of 9 sccm and the argon sputtering gas at 6 sccm. The RF sputtering was performed at 200 W using a 99.99% purity ceramic ZnO target with 15 sccm Ar sputtering gas. The substrates were not heated other than the self heating that occurred during deposition.

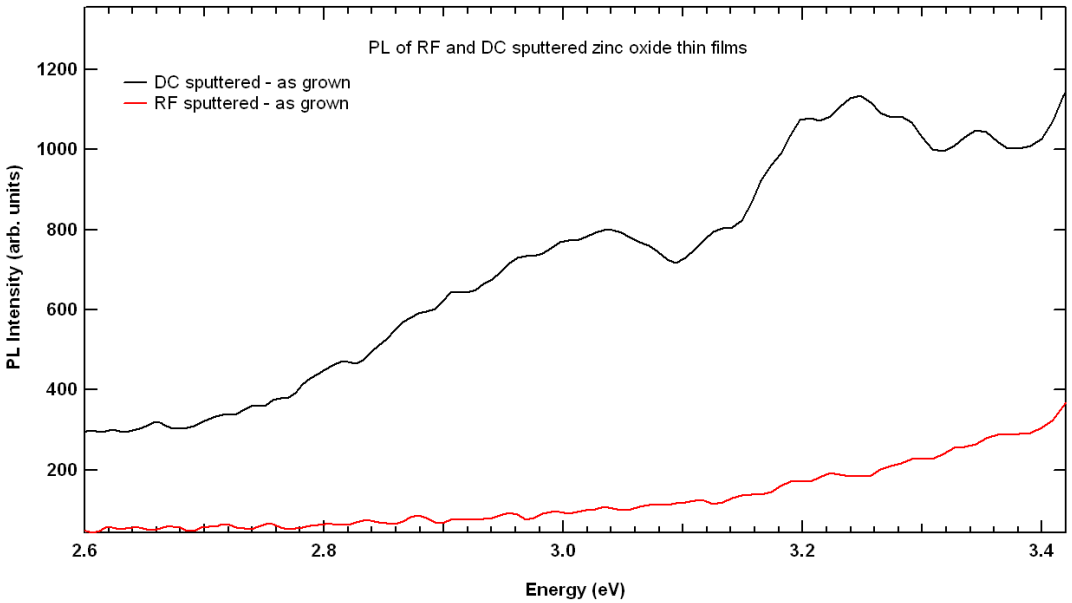

Figure 4-1 PL of DC and RF sputtered ZnO thin films grown on glass

The results of the growth are shown in Figure 4-1 and illustrate that little optical activity occurs when the samples are stimulated by the 333 nm Ar laser emission, at a temperature of 4 K. The DC sputtered film shows two weak emission centres, near 3.05 and 3.25 eV while the RF sputtered film shows no detectable emission. The weak nature of the PL suggests that the overall film quality is very poor, though the DC sputtered film is superior to the RF sputtered.

SEM and AFM images in Figure 4-2 show the difference in morphology between the two films. The average grain diameter of DC sputtered zinc oxide is 200 nm and the RMS roughness is 75 nm, as determined from the AFM image.

For the RF sputtered film the average grain diameter is 50 nm and has a surface roughness of 7 nm. Smaller grain sizes result in an increase in the surface area to volume ratio which suggests that non-radiative surface traps are responsible for the quenched luminescence of the RF sputtered film while the larger grain size in the DC film allows for a greater proportion of radiative transitions within the crystal volume.

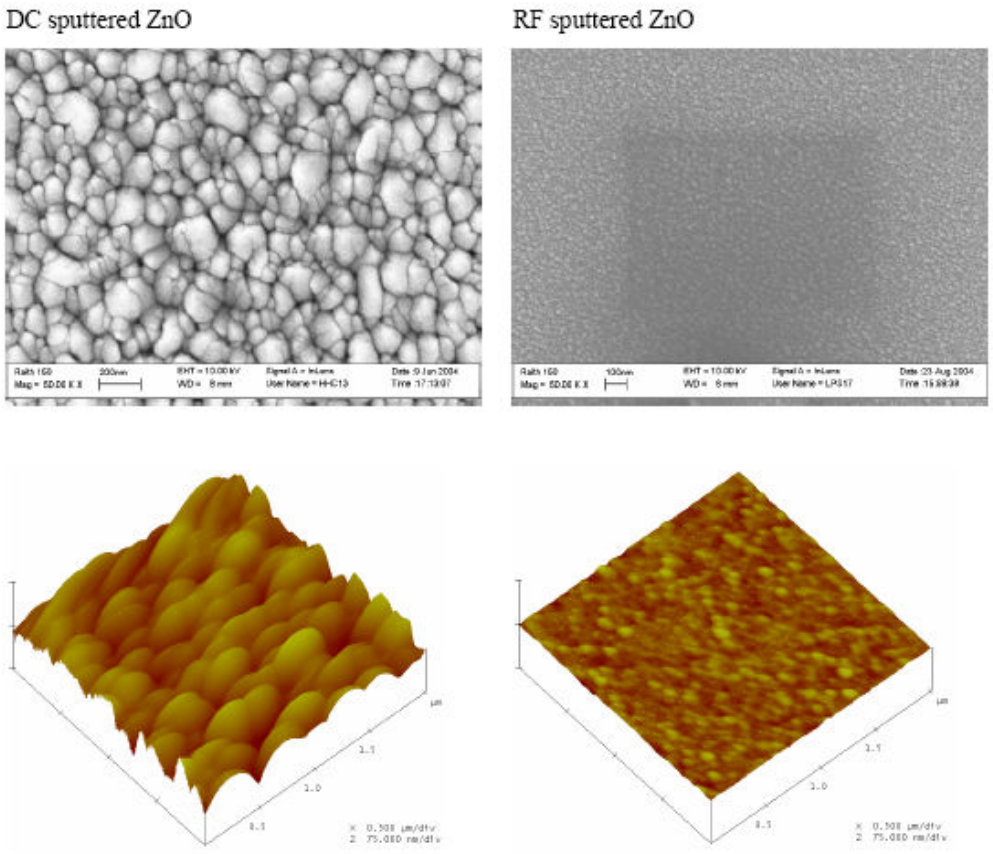

Figure 4-2 SEM and AFM comparison of RF and DC sputtered films

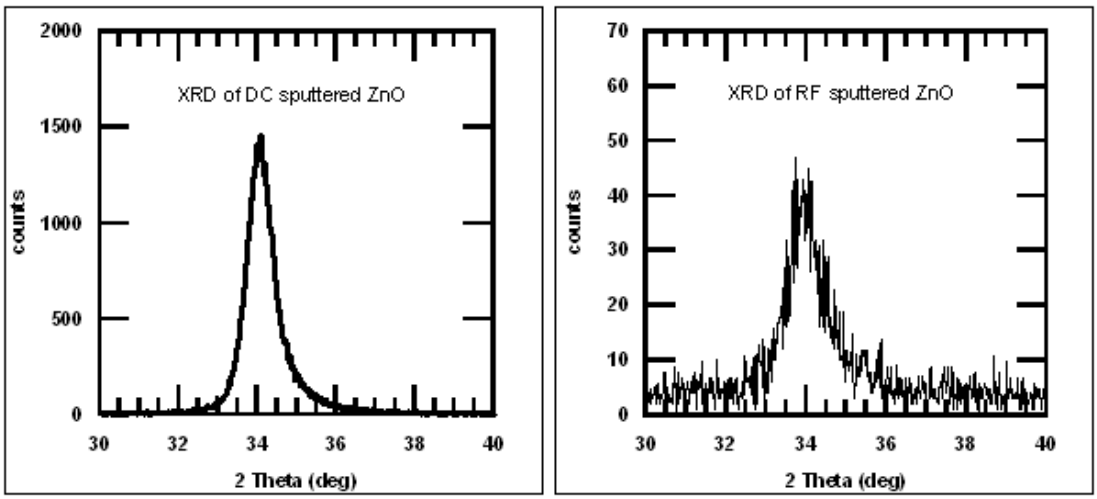

Figure 4-3 XRD of DC and RF sputtered films, pre-annealing

Both films appear transparent on glass and have a 1:1 (Zn:O) stoichiometry as determined by Rutherford Backscattering measurements (RBS).

XRD scans of the as grown films show a peak at 34.18^{O} for the DC sputtered film and 34.08^{O} for the RF, which confirms c-axis oriented polycrystalline growth of ZnO. The large line widths of 0.532^{o} and 0.536^{o} respectively, confirms the high concentration of

defects and inhomogeneous strain, and the shift of the central peak position from the relaxed bulk value of 34.47^{o} suggests a high degree of tensile strain.

Post growth treatment of the films is clearly required to improve the quality and will help determine the optimum growth method for sputtering zinc oxide films.

4.2 Post growth treatment – annealing

One reason for the poor quality of the PL from as-grown sputtered zinc oxide films may be due to the low surface mobility of incident atoms on an unheated substrate. This would result in the polycrystallinity of the films that has been observed and allow for a high defect density and a large degree of unrelaxed strain, due to the lattice mismatch between wurtzite ZnO and the substrate. Post growth annealing is one way of improving the crystallinity of thin films[41, 116-120] by increasing the mobility of individual atoms and allowing relaxation and crystal growth to occur.

In this experiment DC and RF sputtered films grown on Si (100) substrates were cleaved and annealed in a quartz tube furnace under N_2 atmosphere. The temperature was varied between 600 and 900 ^{O}C and the duration was 30 min.

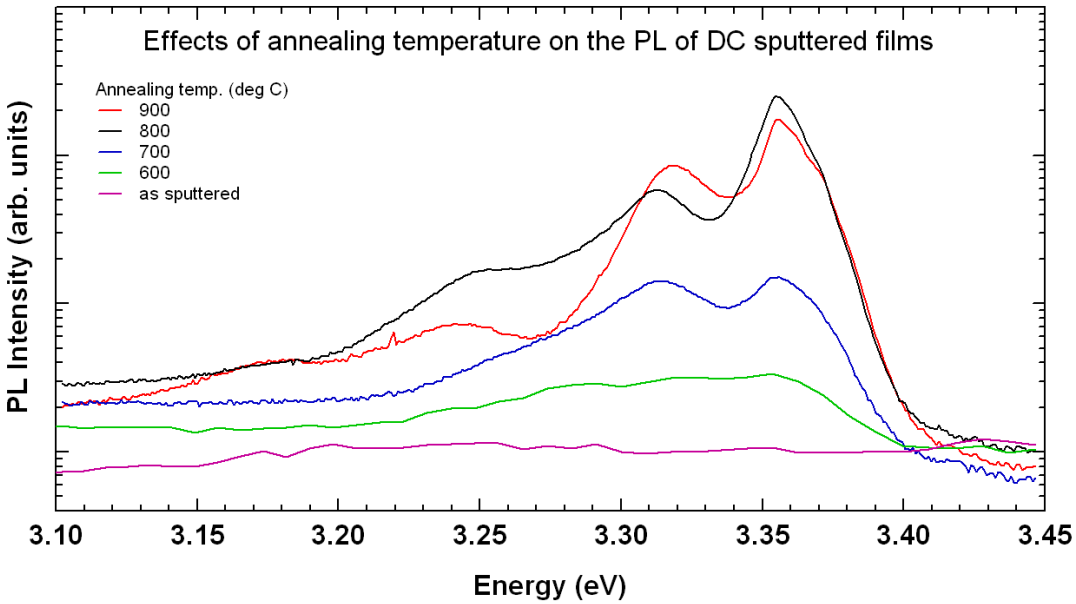

Figure 4-4 Improving DC sputtered films with annealing

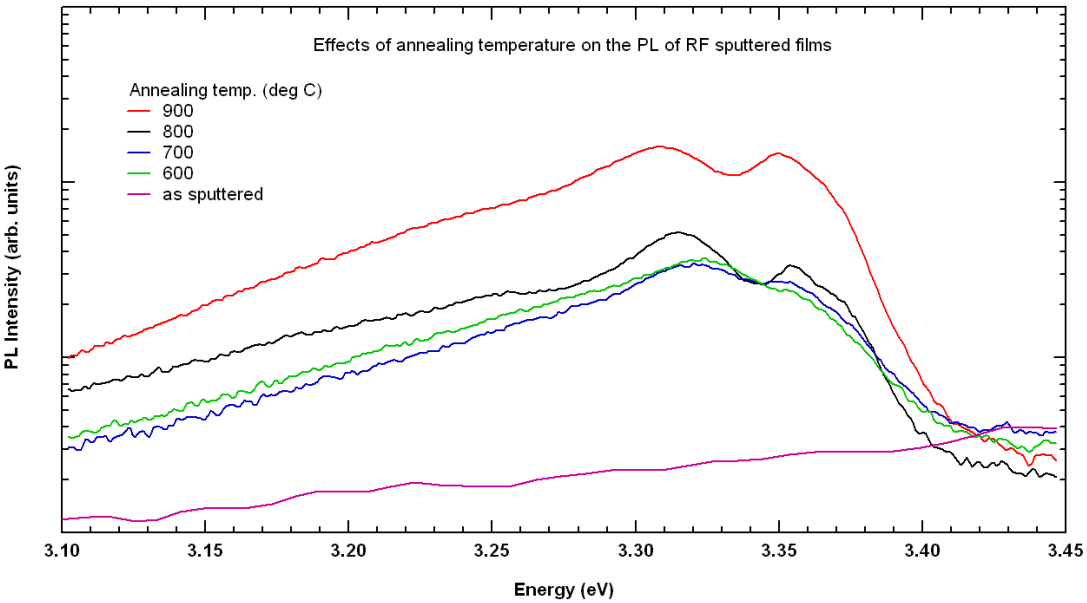

Figure 4-5 Improving RF sputtered films with annealing

The strength of the integrated PL signal over the near band edge region generally increases with annealing temperature (Figure 4-4 and Figure 4-5). The PL is dominated by excitons bound to neutral donors at 3.355 eV and what are either excitons bound to surface related defects or donor-acceptor pair recombination between 3.31 and 3.32 eV. The large line width is typical of sputtered ZnO and indicates that the films are still polycrystalline with a high concentration of defects, surface or otherwise.

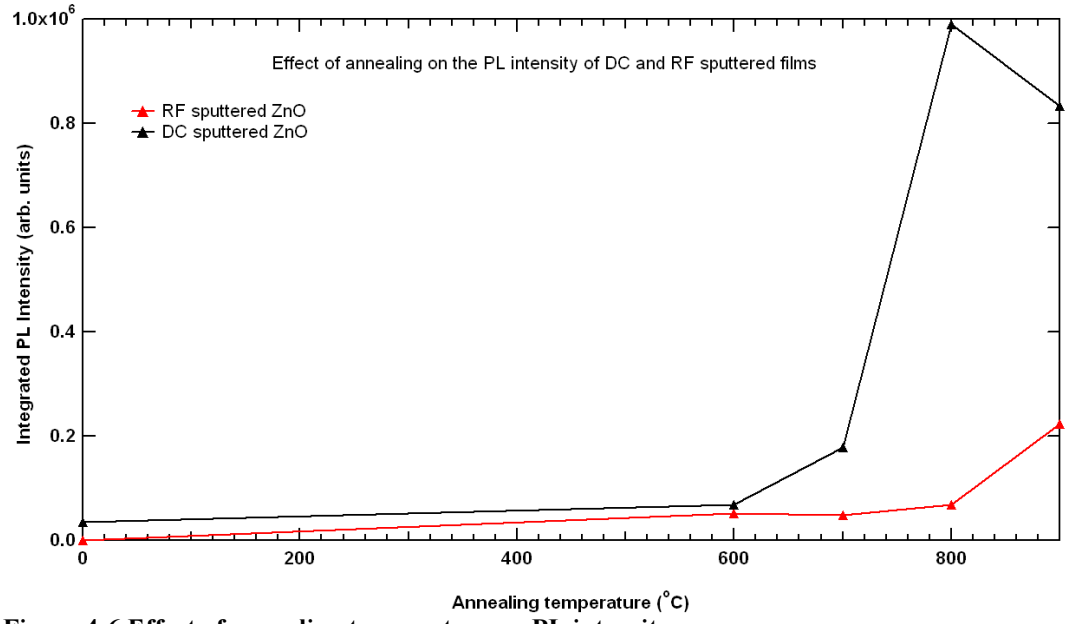

Figure 4-6 Effect of annealing temperature on PL intensity

Figure 4-6 shows how the integrated PL intensity of the near band edge region changes with annealing temperature. The intensity of the DC sputtered film increases sharply above an annealing temperature of 700 ^{O}C and is up to 15 times stronger than that of the RF sputtered film. The intensity of the RF sputtered film is still increasing up to an annealing temperature of 900 ^{O}C however, it is concluded that DC sputtering is the superior method of growth for maximising the optical properties.

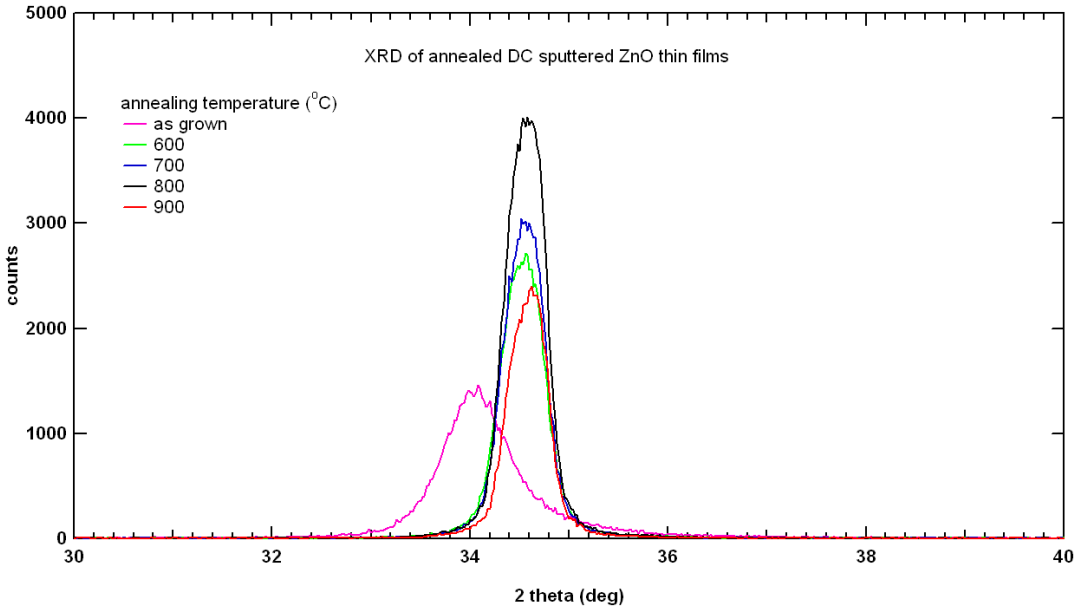

Figure 4-7 XRD of annealed DC sputtered films

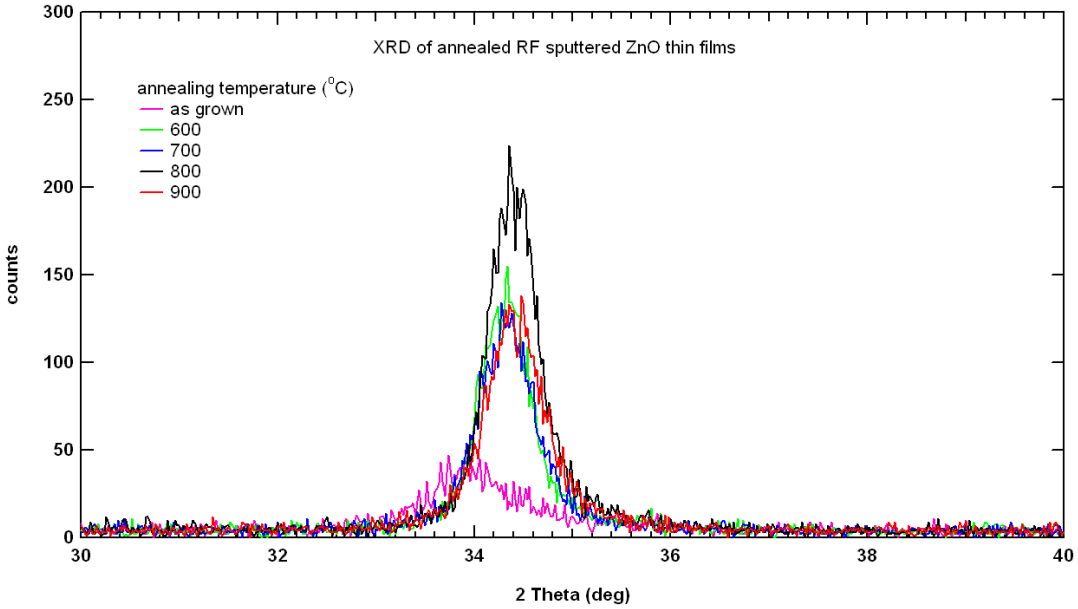

Figure 4-8 XRD of annealed RF sputtered films

DC sputtered ZnO

Annealing temperature	As sputtered	600 °C	700 °C	800 °C	900 °C
FWHM ZnO (002) peak	0.532	0.484	0.488	0.47	0.466
Peak angle (Degrees)	34.18	34.54	34.56	34.62	34.66

RF sputtered ZnO

Annealing temperature	As sputtered	600 °C	700 °C	800 °C	900 °C
FWHM ZnO (002) peak	0.536	0.446	0.516	0.482	0.492
Peak angle (Degrees)	34.08	34.52	34.48	34.6	34.52

Table 4-1 XRD comparison of RF and DC sputtered films

In Figure 4-7 and Figure 4-8, as well as in Table 4-1 the XRD results show a significant improvement in the films when annealed at temperatures as low as 600 ^{o}C. The XRD line width decreases from 0.53^{o} to around 0.49^{o} after annealing and the position shifts from the strained 34.1^{o} to the relaxed 34.5^{o} expected for [0001] ZnO.

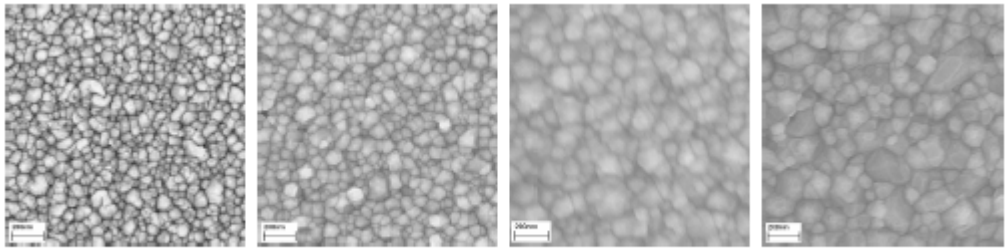

Figure 4-9 SEM of annealed DC sputtered films – Grain size increases with annealing temperature

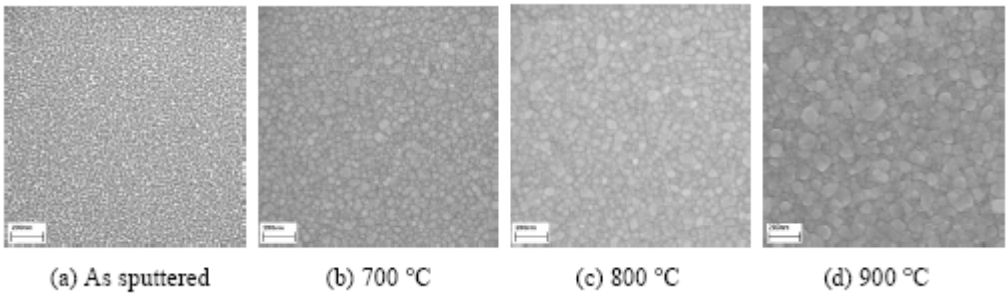

Figure 4-10 SEM of annealed RF sputtered films – grain size increases with annealing temperature

The SEM images, all with the same magnification, of the annealed films show that the crystal size increases with annealing temperature. As the crystal size increases, the surface area to volume ratio decreases. The correlation between increasing PL intensity and mean crystal diameter with annealing temperature is consistent with the hypothesis

that a high surface area to volume ratio results in more surface traps in the excited volume of the crystal and that these surface traps provide an increase in non-radiative pathways for recombination. By annealing the films and increasing the mean crystal diameter, the concentration of non-radiative surface traps in the excited volume is decreased which results in enhanced luminescence.

The integrated 4K PL NBE intensity in Figure 4-11 tracks closely with mean crystal diameter. Further reinforcing the argument that the improved photoluminescence after annealing is strongly related to an increase in the crystal volume.

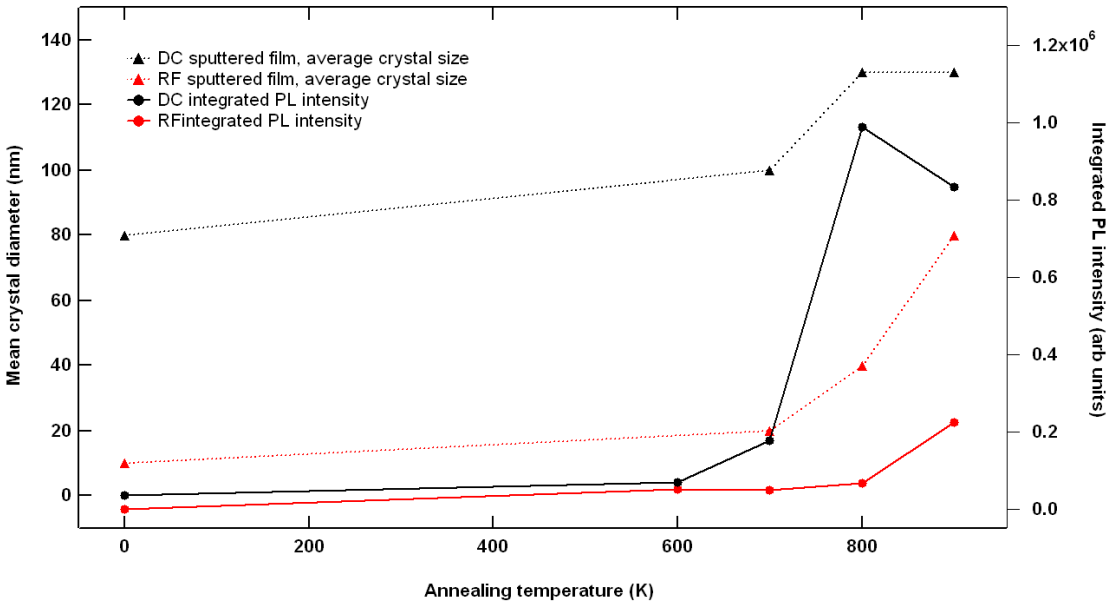

Figure 4-11 Correlation between mean crystal diameter in 4K PL intensity

Similar results obtained by Wang et al[121] for ZnO sputtered on quartz suggest that face to face annealing of the ZnO films may provide the same benefits to the optical and electrical quality without increasing the surface roughness as a result of sublimation during the annealing process.

4.2.1 Etching of sputtered films

In order to further investigate the properties of sputtered zinc oxide for future device applications, reactive ion etching (RIE) experiments were performed on both the DC and RF sputtered, annealed films.

RIE is a technique for patterning and micro processing of thin films and substrates. Unlike wet etching, it produces no liquid waste. It is easily scalable and allows for a high degree of control over the etching process.

The etching was performed after sample annealing using an Oxford Plasma lab 80 plus system. CHF_3 was used as the etching gas with a flow of 25 sccm and the etching pressure was kept at 20 mTorr. A 50 nm Cr mask was used to help determine etching depth. The etching time was 30 minutes and an etch rate of around 5 nm/min was achieved.

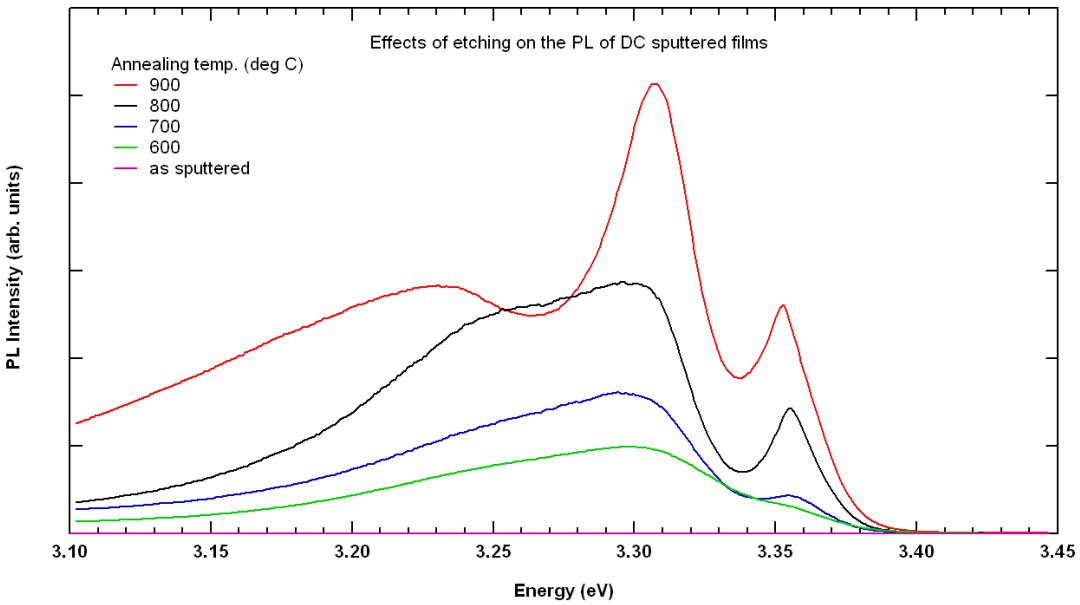

Figure 4-12 RIE etching of annealed DC sputtered films - PL

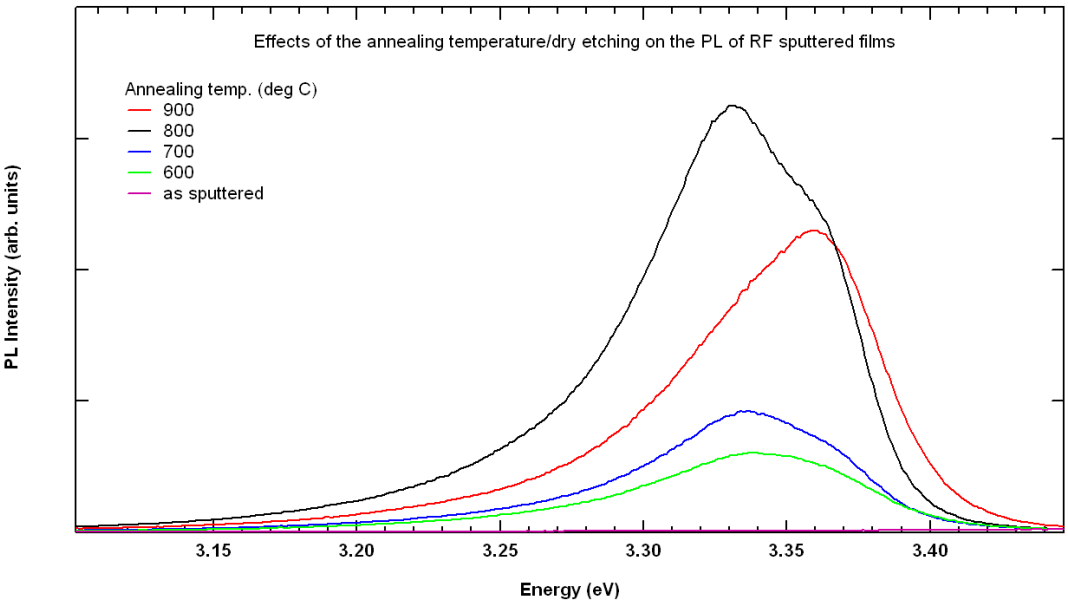

Figure 4-13 RIE etching of annealed RF sputtered films - PL

The PL of the films that have been etched after annealing show several changes from the un-etched. The most significant of which is the emergence of a new PL peak around 3.23 eV on the DC sputtered film, a region associated with donor-acceptor pair recombination, suggesting the introduction of acceptor impurities into the film. Also of note is the dominance of an emission centred around 3.31 eV, an area associated with excitons bound to structural defects.

DC sputtered ZnO

Annealing temperature	As sputtered	600 °C	700 °C	800 °C	900 °C
FWHM (002) peak	0.632	0.508	0.486	0.478	0.466
Peak angle (Degrees)	34.08	34.56	34.52	34.58	34.62

RF sputtered ZnO

Annealing temperature	As sputtered	600 °C	700 °C	800 °C	900 °C
FWHM (002) peak	0.644	0.566	0.57	0.522	0.672
Peak angle (Degrees)	33.74	34.34	34.28	34.26	34.48

Table 4-2 XRD results for annealed/etched films

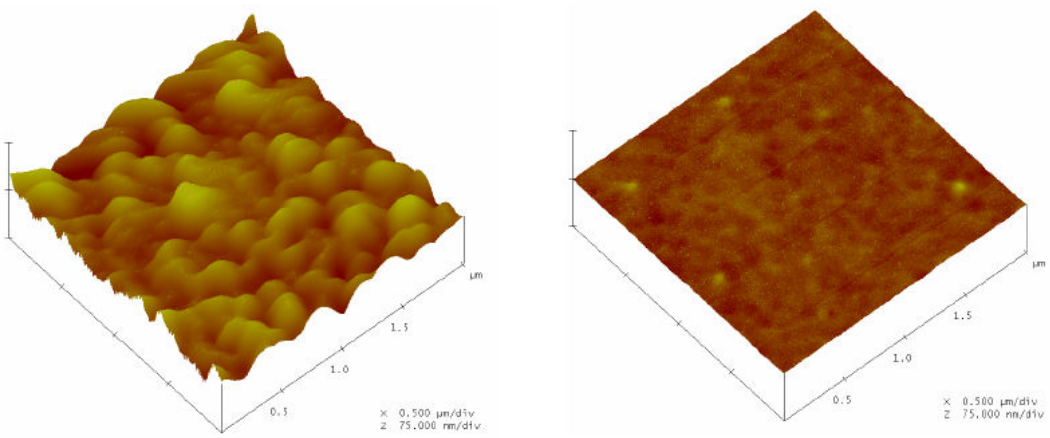

Figure 4-14 AFM image of RIE etched surfaces

Figure 4-14 shows an AFM view of the surfaces of the sputtered, etched films. The DC sputtered film on the left shows an average grain diameter of 200 nm and an RMS roughness of 61 nm. The RF sputtered film on the right shows an average grain diameter of 50 nm and a surface roughness of 11 nm.

These results show that the roughness of the DC sputtered film was reduced by the etching process while the roughness of the smoother RF sputtered film was increased. RIE is known to increase the roughness of thin films.

Rutherford back scattering (RBS) measurements were performed to determine the stoichiometry of the films and to determine the nature of any impurities present after the etching process had been completed. The ion sources used a 1.0 MeV $^{4}He^{+}$ at an incident angle normal to the plane of the film. The detector was mounted at an angle of 165^{o} in a backscattering geometry, allowing a depth resolution at the surface of better than 20 nm.

Results show a carbon rich surface layer on all dry etched samples at all annealing temperatures. For the DC sputtered films, the carbon occupies the top 45 nm at a concentration of 25+/- 2 %. The remainder of the film was measured to be stoichiometric. It is hypothesised that carbon from the CHF_3 etching gas is incorporated into the surface layer during etching.

The RF sputtered film was also found to have a 30 nm surface layer of carbon incorporated into the film.

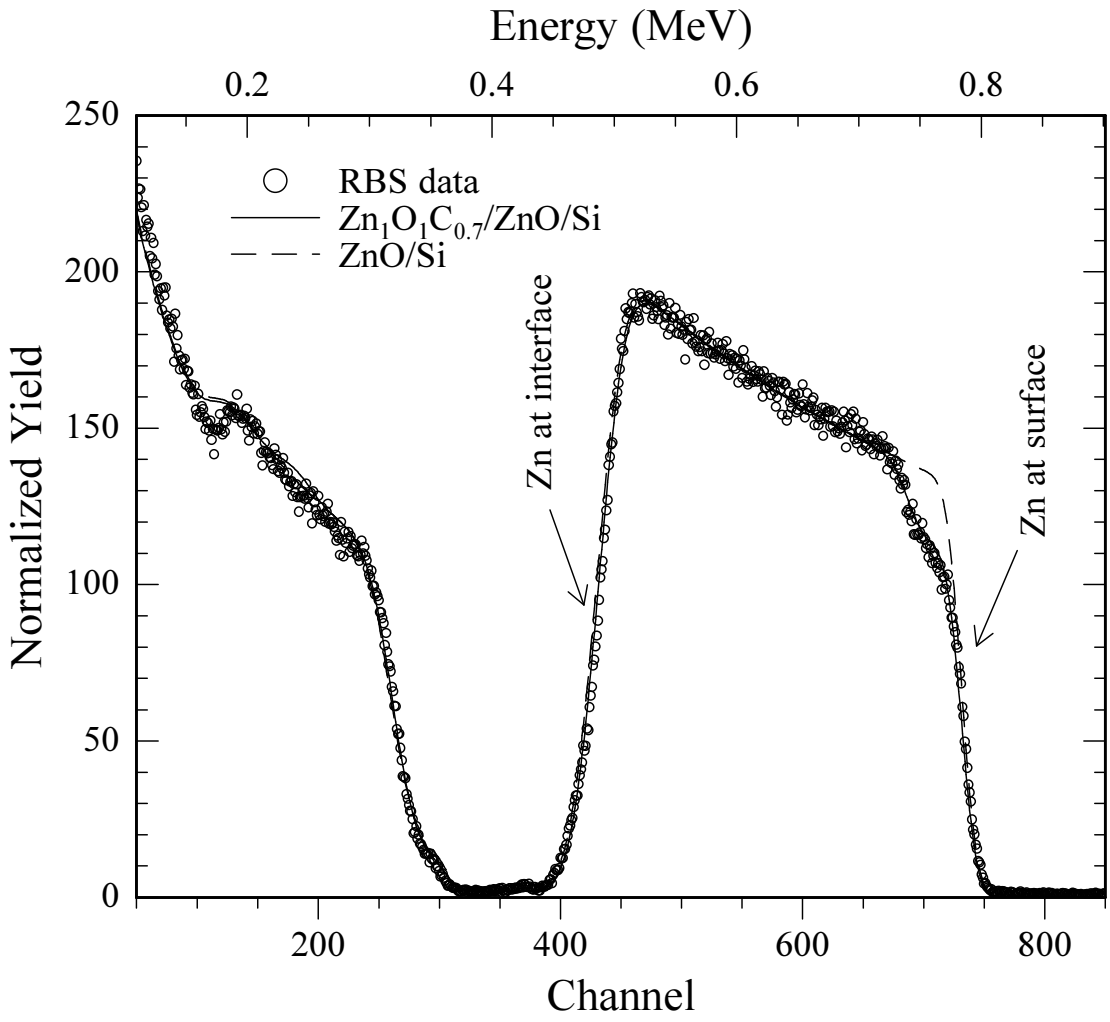

Figure 4-15 RBS results showing carbon incorporation

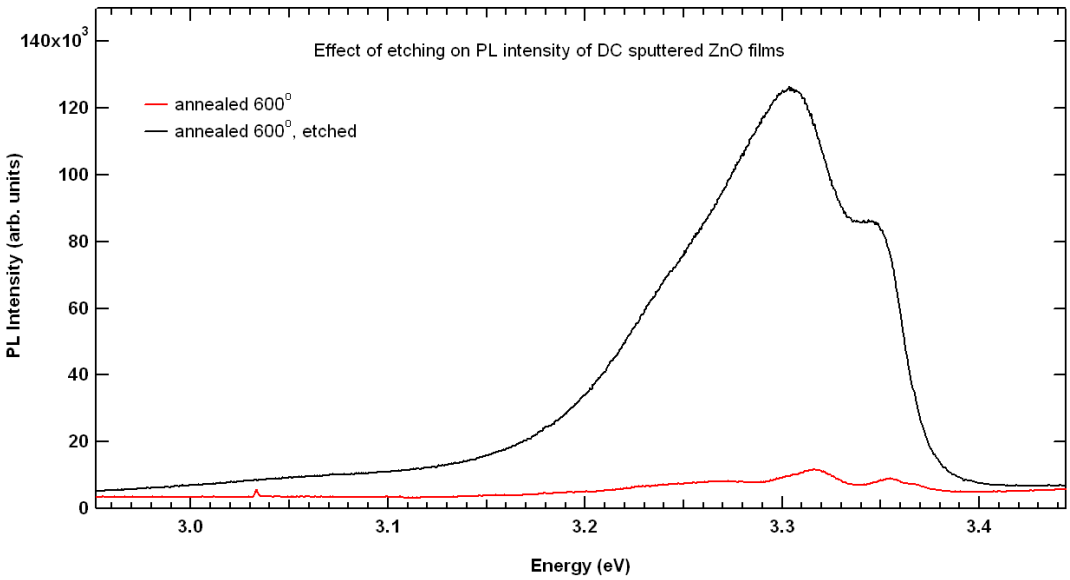

Figure 4-16 Enhanced PL after RIE etching – carbon incorporation

Figure 4-16 shows the effect of this carbon enriched layer on the PL intensity. The etching process is clearly shown to increase the intensity of the PL emission by an order of magnitude and also to shift the peak position to a slightly lower energy. The PL experiment under these conditions is a surface measurements as the laser penetration depth is limited to the top 40 nm of the film at this wavelength[44]. This suggests that the shift in peak position may be a result of the strain in a film being thickness dependent, with material close to the substrate being more strained than material at the surface, as the film is etched away it exposes increasingly strained layers of the film. The increase in PL intensity can be attributed to the carbon acting as a radiative centre as suggested by the observation of enhanced luminescence as the result of incorporated carbon reported in PLD grown zinc oxide[122]

4.3 Substrate trials

Thin films of zinc oxide have been deposited directly on several different substrate materials via DC sputtering. Samples of each film were then annealed in a nitrogen atmosphere over a wide range of temperatures.

The ZnO films used in the annealing trial were grown to a thickness of 500 nm by DC sputtering under identical conditions. Each sample used in the trials was cleaved from the same as grown film in order to promote uniformity. The samples were annealed in a nitrogen atmosphere for half an hour over a range of temperatures in order to determine the effect of annealing temperature on the films optical and physical properties.

Recently a similar trial was performed by Kong et al[123] using MOCVD as the growth method.

Desired properties

- Preferred crystal structure in [002] orientation.
- Highly insulating films (low losses).
- Transparent films.
- Smooth and uniform deposition.
- Highly piezoelectric characteristics.
- High optical response.

4.3.1 Silicon

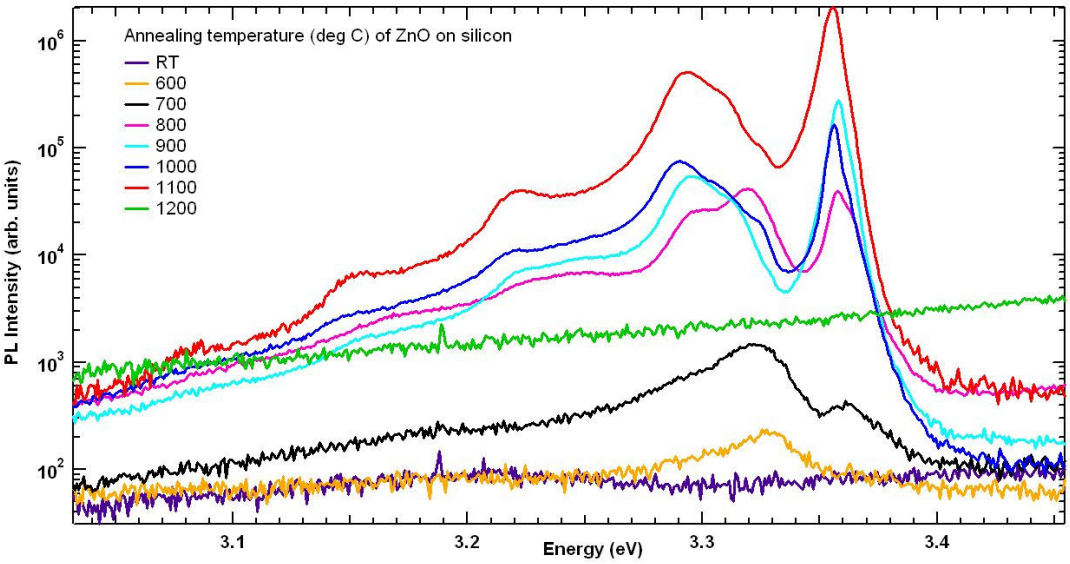

Figure 4-17 4K PL of ZnO on silicon - annealed

Zinc oxide films grown on silicon responded well to the annealing trials. The peak PL response increased by 4 orders of magnitude when annealed at 1100 ˚C. The spectrum is characterized by a dominant narrow emission at 3.35 eV, typically associated with neutral donors, and a broader less intense peak at 3.3 eV. This second peak, while frequently observed in many films, remains somewhat controversial, but is now commonly attributed to excitons bound to structural defects. Third and fourth order phonon replicas of the main PL peak are clearly observed, indicating good crystal quality throughout the film.

As expected the SEM images (below) show an increase in grain size with annealing temperature. However at an annealing temperature of 1200 ˚C we observe the complete quenching of the photoluminescence, a rapid drop from the peak intensity observed at 1100 ˚C which corresponds with a fundamental change in the observable structure of the films. The XRD results show a rapidly decreasing ZnO peak around 34 degrees as the annealing temperature is increased. At 1200 ˚C the ZnO peak is undetectable, leaving only indications of the formation of a Zn_2SiO compound.

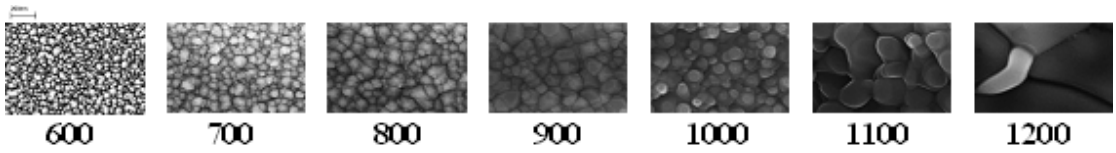

Figure 4-18 SEM of ZnO on silicon - annealed
Annealing temp in deg C. 50,000x magnification.

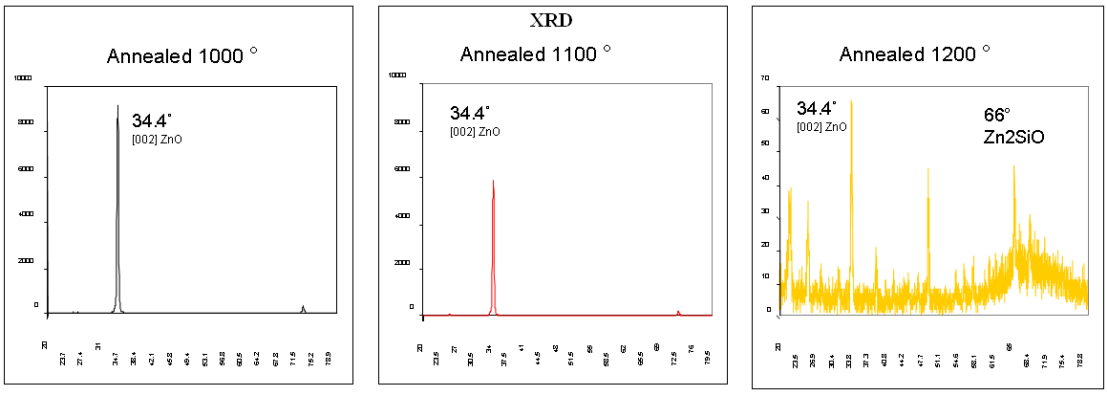

Figure 4-19 XRD of ZnO on silicon - annealed

4.3.2 Sapphire

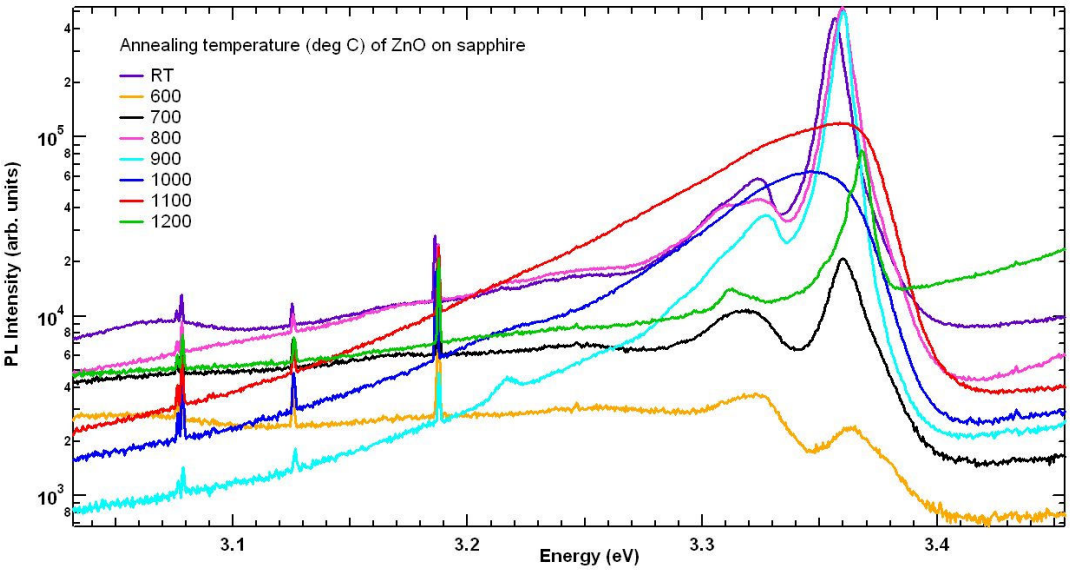

Figure 4-20 4K PL of ZnO on sapphire – annealed

The most interesting results of the trial were obtained for the zinc oxide films grown on a sapphire substrate. The as-grown films showed good optical properties with a strong narrow emission peak at 3.36 eV dominating the photoluminescence spectrum. XRD results[124] indicate a high quality zinc oxide film and the SEM images show a flat

uniform surface. Annealing this film in nitrogen at a temperature of 600 ˚C appears to have a detrimental effect on the films properties. Although the band edge features are visible they have diminished in intensity by nearly two orders of magnitude. The XRD profile shows no sign of the characteristic ZnO peak, indicative of a highly disordered film. Increasing the annealing temperature to 700 and 800 ˚C restores some of the films original optical properties. The XRD images for these annealing temperatures also shows indications of the ZnO peak returning. However increasing the annealing temperature further still results in the formation of what is likely to be $ZnAl_2O_4$ as suggested by the emerging peak at 59 degrees on the XRD images. The most notable feature is the abrupt transformation of the films visible appearance as the temperature is increased from 1000 to 1100 ˚C. The previously uniform films takes on a badly fractured appearance which corresponds with the films metamorphosis from ZnO to $ZnAl_2O_4$ as it begins reacting with the substrate material.

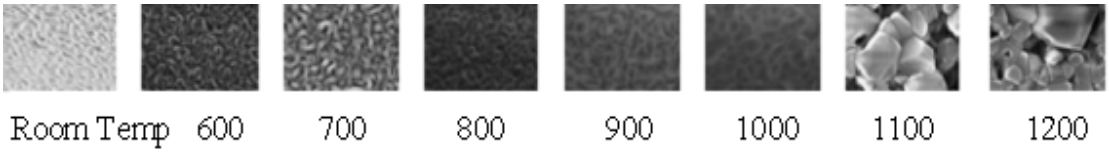

Figure 4-21 SEM of ZnO on sapphire - annealed

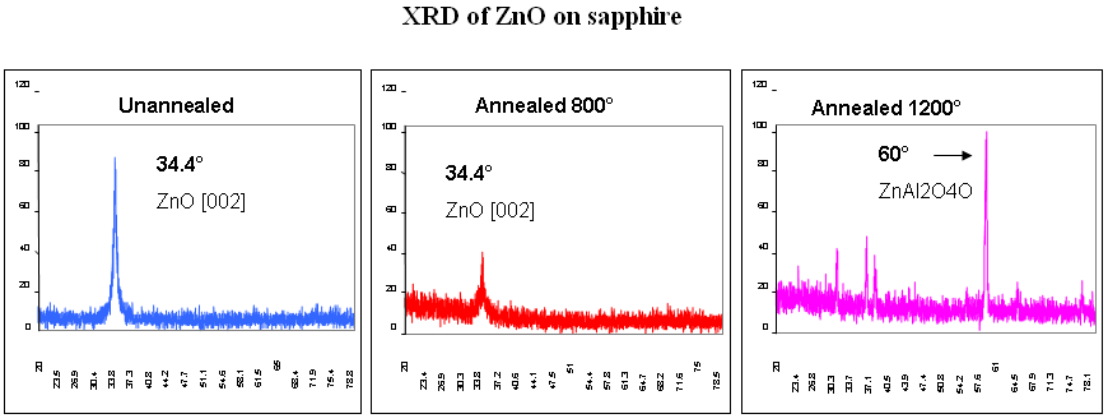

Figure 4-22 XRD of ZnO on sapphire

4.3.3 Quartz

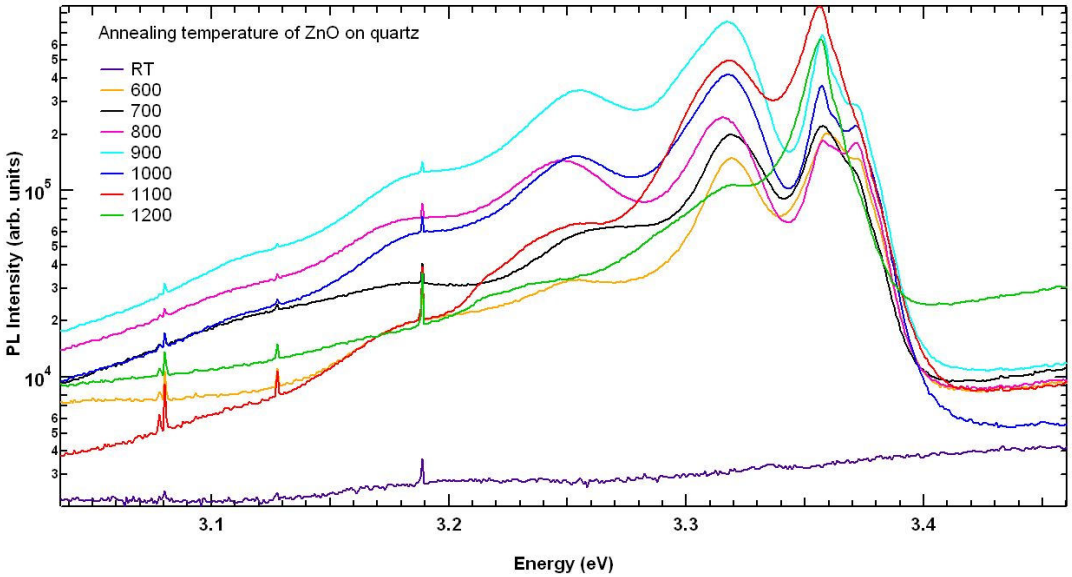

Figure 4-23 4K PL of ZnO on quartz - annealed

The PL of ZnO grown on a quartz substrate indicates similar growth to that of ZnO on silicon. The line width of the PL relating to donor bound excitons at 3.37 eV is relatively broad when compared to that of single crystal ZnO and the presence of the strong defect related PL peak at 3.32 eV indicates a highly polycrystalline film. This conclusion is further supported by the SEM images. Annealing the films at higher temperatures improves the quality of the films by increasing grain size. At temperatures above 1000 ˚C "terracing" of the grains occurs in which successively smaller layers of ZnO appear atop one another.

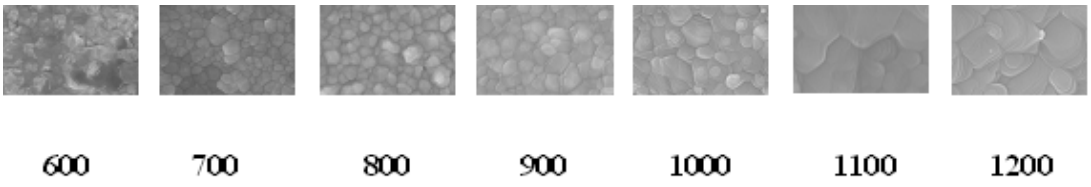

Figure 4-24 SEM of ZnO on quartz - annealed
50,000x magnification.

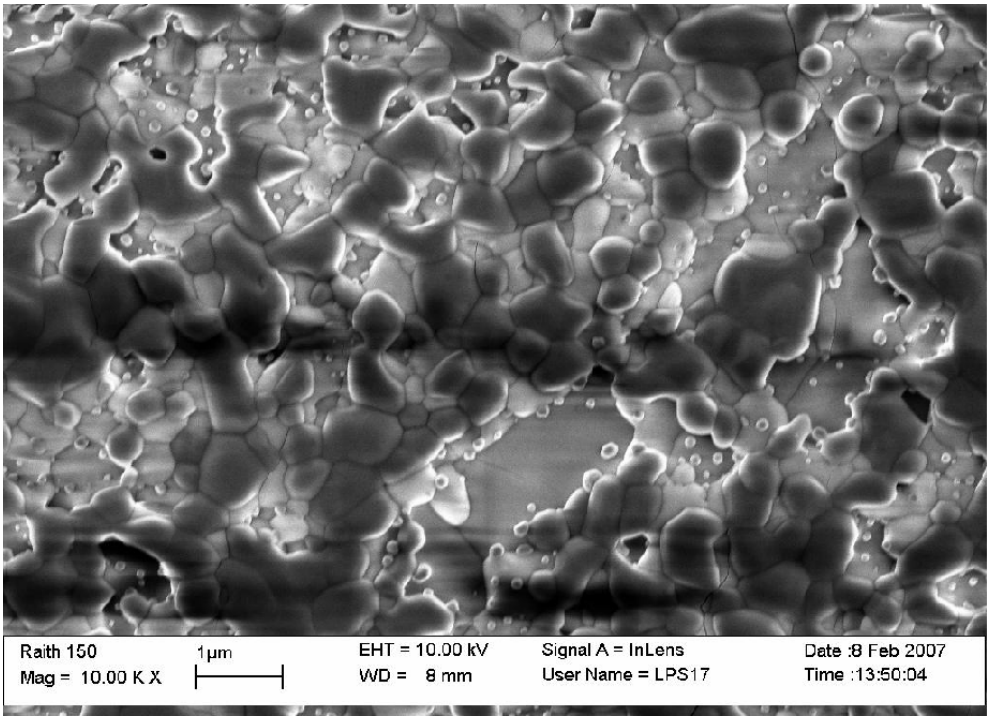

Figure 4-25 SEM of ZnO on quartz after annealing at 1200 ^{o}C – 10,000x magnification

The high resolution SEM image in Figure 4-25 shows the surface of the film after annealing at 1200 ^{o}C. The substrate is clearly visible through gaps in the film that were not apparent pre-annealing. This is direct evidence of the degradation of the ZnO film at annealing temperatures above 1100 ^{o}C.

4.3.4 Fused Silica Glass

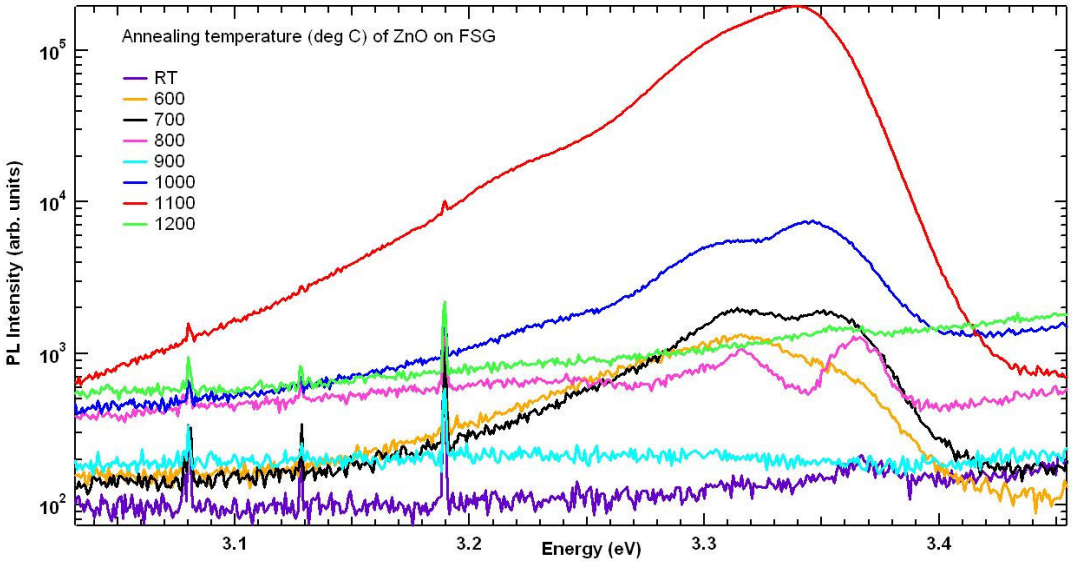

Figure 4-26 4K PL of ZnO on glass - annealed

The band edge photoluminescence (PL) of DC sputtered zinc oxide, on a fused silica substrate, is again characterised by broad emissions centred around 3.35 eV, consistent with PL related to excitons bound to neutral donors. A relatively large fraction of the laser light is scattered or reflected from the surface of the films. These characteristics indicate highly polycrystalline zinc oxide.

Treating the films by thermal annealing for half an hour is shown to significantly enhance the intensity of the PL by up to three orders of magnitude. Corresponding SEM images of the film surface show a clear indication of increased grain size, up to an annealing temperature of 1100 ˚C. Annealing above this temperature shows a marked change in film properties. The photoluminescence is entirely quenched, and the visual indications of large zinc oxide grains within the film in the SEM images have vanished.

Figure 4-27 SEM of ZnO on glass - annealed

4.3.5 Summary of substrate trials

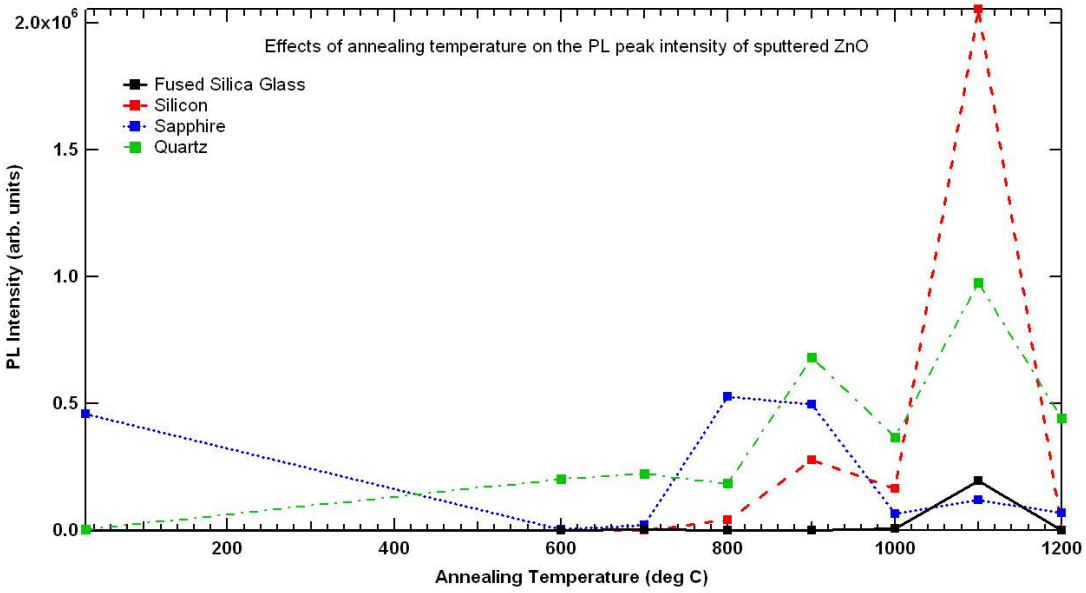

Figure 4-28 PL intensity of ZnO on various substrates - annealed

Figure 12 shows the effect of annealing temperature on the peak PL intensity of films deposited on various materials. Annealing at temperatures up to 700 ˚C for half an hour shows no significant improvement of the films optical properties, and in the case of the film grown on sapphire, appears to have a detrimental effect. The sapphire shows the most improvement when annealed at 800-900 ˚C, as well as presenting a local maximum at 1100 degrees.

The films grown on silicon, quartz and fused silica glass both respond best to an annealing temperature of 1100 ˚C and exhibit a small local maxima at 900 degrees. A minimum occurs at an annealing temperature of 1000 degrees, indicating that there are perhaps two separate mechanisms through which the optical properties of ZnO films are enhanced by annealing. A common feature of all three films, is the loss of photoluminescence at a temperature of 1200 degrees. The SEM image shown previously in Fig 5. shows exposed substrate and a loss of film uniformity.

An explanation for the two optimum annealing temperatures requires invoking multiple competing effects. The mostly likely reason for the shape of the lines are as follows. As a general rule, improving the crystal quality improves the optical efficiency of the material. This means that when the annealing temperature is increased and point defects such as interstitial atoms, and vacancies are annealed out, the PL will increase. As the temperature is increased further defects begin to be introduced, such as oxygen and zinc vacancies, this effect inhibits the NBE luminescence. When point defects are being annealed out faster than they are being generated the PL efficiency increases, at higher temperatures when point defects are being generated faster than they are annealed the PL efficiency decreases. The point at which defect generation outstrips the rate at which they are annealed out would appear to take place at an annealing temperature between 800 and 900 ^{o}C for sputtered zinc oxide.

The second maximum occurs at a higher temperature and is likely the result of large scale morphological changes in the films resulting in larger crystal domains which generally results in improved PL efficiency. Between 1000 and 1100 ^{o}C this improves the efficiency faster than point defects are created, resulting in an increase in PL efficiency with increased annealing temperature. However at temperatures above 1100 ^{o}C the zinc oxide begins to chemically react with the substrate material, regardless of the type, which has a detrimental effect on the optical quality of the material and reduces the overall optical efficiency.

4.4 Opto-Piezo hybrid device

In additional to having useful optical properties, zinc oxide is highly piezo-electric, however crystal conditions conducive to high optical quality are not necessarily conducive to high piezo-electricity. With this in mind, based on previous work, attempts were made to design a multistage growth capable of producing a film with a strongly piezo-electric surface layer and an optically active buffer layer, grown on an optically transparent substrate.

To optimise optical properties 100 nm of ZnO was deposited via DC sputtering. The substrate of choice, quartz, was a compromise between using an optically transparent substrate and maximising the PL signal of the film. The deposited film was annealed

in nitrogen at 900 ^{o}C for one hour as this was shown to be an optimum annealing temperature, without risking the formation of new compounds at the ZnO/Quartz interface that could prove problematic at the higher annealing temperature of 1100 ^{o}C. Unannealed ZnO was previously determined to have excellent piezo-electric properties and so 200 nm of ZnO was sputtered on top of the PL layer and left as grown.

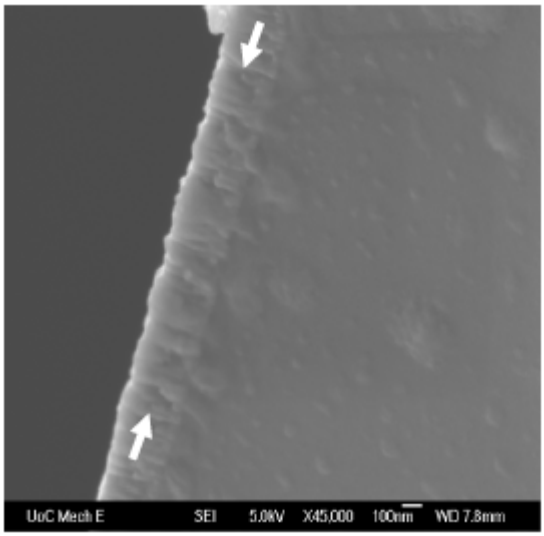

Figure 4-29 SEM of opto-piezo hybrid device

Cross sectional SEM shows the substrate/film interface clearly and also indications of the plane interface between the optical and piezo layers of the film and XRD results show two distinct peaks corresponding to the two separate layers. No other peaks were detected, indicating that the growth is highly c-axis oriented.

In principle this shows that two clearly distinct layers of ZnO can be deposited, one on top of the other, and maintain their physical characteristics.

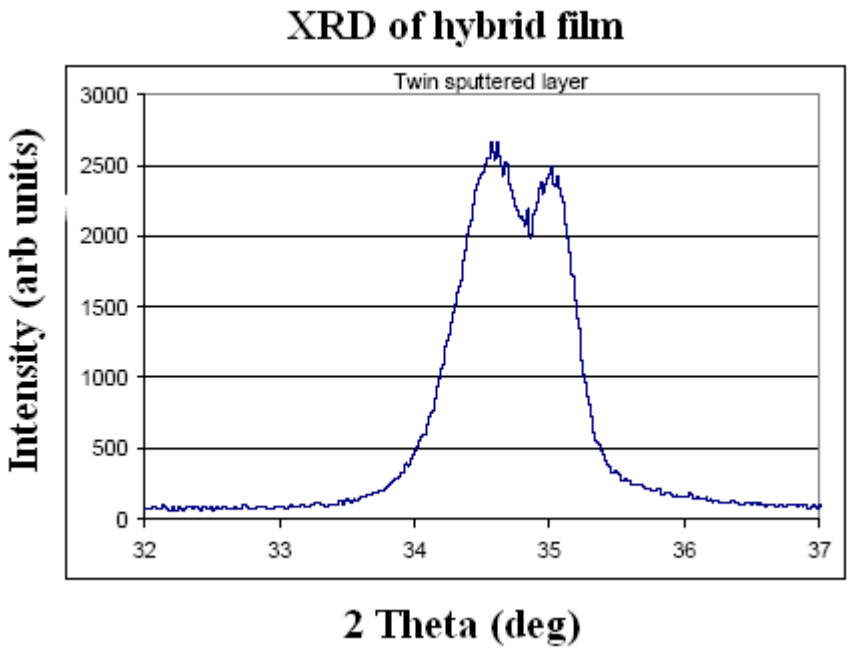

Figure 4-30 XRD of hybrid film

While no photoluminescence was detected from the films, the technique is still highly experimental and potentially subject to a high degree of refinement.

Potential areas of concern include the optical quality of the first 40 nm of the PL layer, even after annealing, as this is the volume of film being excited by a laser directed in from the back side. Experiments need to be conducted to determine this.

4.5 Conclusions

Initial sputtering growths were performed using both DC and RF sputtering to determine the optimum growth method maximizing the optical properties of ZnO thin films. The DC method was determined to produce higher quality material and once initial growth trials had been performed became the default growth method for subsequent experiments. PL line widths were typically in the order of 50 meV, much larger than that of either bulk growth methods, or MBE thin films.

XRD results show that annealing at temperatures as low as 600 ^{o}C significantly reduced strain in the [0001] plane. Optical quality films were successfully grown on a variety of substrates, confirming the potential of the growth method for future ZnO based devices.

Films grown on silicon, quartz and sapphire substrates showed strong optical characteristics at all annealing temperatures above 600 ˚C, and enhanced luminescence when annealed at temperatures of 900 and 1100 ˚C. Films grown on a fused silica substrate showed weak photoluminescence at all annealing temperatures below 1100 degrees. The PL of films grown on fused silica had a much larger line width than the films grown on sapphire and silicon, indicating poor crystallinity, further evidenced in SEM scans. Silicon provided for the highest quality zinc oxide, as determined by the PL, showing narrow line width of the PL associated with near band edge donor bound excitons and up to 4th order phonon replicas, consistent with results obtained by Song et al[125] who sputtered films on Si and glass substrates. Annealing zinc oxide at a temperature of 1200 ˚C on any of the selected substrates resulted in a significant degradation of the film quality, which can be clearly observed in both SEM images and in the XRD patterns. Annealing at this temperature on a silicon substrate showed strong evidence of the formation of a zinc silicate compound, Zn_2SiO_4 while annealing on a sapphire substrate shows the formation of $ZnAl_2O_4$. Both are a clear indication of a critical operating temperature for future ZnO devices.

Attempts to grow a hetero piezo-opto film were inconclusive. Although the principle remains sound, difficulty was had detecting luminescence from a high quality optical film sandwiched between a highly piezoelectric surface layer and a quartz substrate. It is plausible that the substrate/film hetero-junction is not optically active yet the piezo/opto hetero-junction is. Suggestions to improve the results of the experiment include increasing the thickness of the optical layer and changing the substrate to maximise the quality of the optical layer at the ZnO/substrate interface.

5 Conclusions and Future Work

In the first chapter zinc oxide was discussed as a potential candidate for a wide range of useful applications. Different classes of device often require vastly different properties, for this reason many different techniques are used for the growth of zinc oxide.

The primary goals of this thesis were threefold.

In chapter two the aim was to gain an understanding of the optical properties of single crystal bulk zinc oxide, to identify the known transitions, to investigate the influence of the polar nature of zinc oxide on the PL and to expand the knowledge of the unassigned or disputed transitions.

The goal of chapter three was to investigate the optical properties of MBE grown thin films and use that information to optimise the growth and post growth treatment for enhanced film quality and attempts to introduce majority acceptors via doping for the growth of p-type material.

In chapter four the aim was to optimise the growth of optically active sputtered zinc oxide on a wide range of substrates, to improve those properties through post growth treatment and to attempt to devise a means of coupling optically and piezo active layers in a single thin film.

This chapter summaries the main results of the three previous chapters and discusses their impact within the framework of the stated goals of the thesis.

5.1 Summary of investigation of bulk zinc oxide

A contentious near band edge transition was conclusively identified and classified as a phonon replica and the primary competing model, the transition as a donor acceptor pair recombination, is robustly tested and subsequently dismissed.

Measurable difference in the luminescence of the two polar faces are observed in unannealed, low carrier concentration crystals which may be indicative of band bending at the surface as a result of the free carriers being redistributed by the internal electric field. This has potential impact on the formation of Schottky diode for device applications.

The splitting of the A_T and A_L free excitons is shown to vary considerably across a range of different samples which may account for much of the discrepancy in quoted transition energies in the literature.

After annealing in vacuum traces of copper were shown to be present in the material by the observation of characteristic PL features. Debate as to whether the copper was introduced during annealing or was already present was solved when the samples were re-annealed in a hydrogen forming gas. It is hypothesised that hydrogen sitting at an interstitial site quenches the optical transitions of the neighbouring copper atom and that annealing the crystal in vacuum drives out the interstitial hydrogen, freeing up the copper as an optically active center, while re-annealing in hydrogen gas reintroduces hydrogen back into the bulk, thus quenching the copper center.

The deep level PL emission is fit using three Gaussians which demonstrate a consistent method of fitting the PL emission over a wide range of treated samples.

5.2 Summary of MBE grown films

Films grown showed a typical line width in the order of 5 meV, indicating a lower degree of uniformity than that present in single crystal bulk zinc oxide. This was to be expected due to a serious lattice mismatch between zinc oxide and the commonly used sapphire substrates. The best results were obtained from ZnO grown on an MgO buffer layer and gave line widths as low as 2.5 meV. PL results show the films surface to be chemically stable in air over a period exceeding nine months which has positive implications for future device applications. Growth of p-type zinc oxide was attempted by nitrogen incorporation during growth. PL indicates the presence of acceptors as a result of the nitrogen in the form of donor-acceptor pairs. The basis for the peak assignment is the observation of a shift in the peak energy across the sample,

while the band gap remains constant, these effect would be typical of a change in the carrier concentration across the film which is not entirely unexpected for MBE grown films.

The temperature dependence of an MBE grown film was studied and the near band edge luminescence was shown to have a dual activation energy of 6.4 and 30.7 meV, various methods for analysing the change in bandgap with temperature were also compared in order to provide a more quantitative result than the commonly used Vaarshni fit.

5.3 Summary of sputtered films

DC sputtering was found to be superior to RF sputtering for the growth of optically active films, this is likely a function of larger average grain size and improved crystallinity. Etching the films using a common method was shown to incorporate carbon into the surface of the film which, contrary to expectation, improved the optical efficiency of the material.

Optical quality films were successfully grown on a variety of substrates. These included glass, silicon, quartz and sapphire.

Annealing the samples grown on various substrates over a range of temperatures showed optimum annealing temperatures at both 900 and 1100 degrees for all substrate types indicating two distinct and possibly competing modes of crystal annealing. Increasing the annealing temperature to 1200 degrees proved devastating to the optical quality of the material. XRD results show a new chemical composition to the material that indicates a large scale chemical reaction between the film and substrate. This temperature indicates a hard ceiling for all zinc oxide based devices.

5.4 Future work

The identity of many of the dominant PL feature in most hydrothermally grown bulk zinc oxide still remains unknown, current theories suggest that lithium, iron or lead may all be potential candidates. A film grown by the same method was shown to be absent this feature, it is hoped that SIMS results may be able to distinguish a difference in the chemical composition of the doping concentrations in the samples that would then provide a clear lead for subsequent implantation experiments.

New experimental equipment implemented in the research lab has significantly improved the capacity to accurately measure the deep level luminescence, much of the difficulty in this thesis in identifying unambiguous transition energies is compounded by the presence of grating defects in the area of interest. The removal of this barrier provides new opportunities for superior data acquisition.

The substrate used in MBE grown films is of great significance. The improvement of overall film quality through better buffer layers or through alternative substrates with a lower lattice mismatch than that of sapphire will play a major role in the improvement in a reduction in defects and an improvement in overall quality of MBE grown films. Growth of p-type material however must still remain the primary goal if widespread implementation of ZnO devices is to be realised.

Attempts to grow a hetero piezo-opto film were inconclusive. Although the principle remains sound, difficulty was had detecting luminescence from a high quality optical film sandwiched between a highly piezoelectric surface layer and a quartz substrate. It is plausible that the substrate/film hetero-junction is not optically active yet the piezo/opto hetero-junction is. Suggestions to improve the results of the experiment include increasing the thickness of the optical layer and changing the substrate to maximise the quality of the optical layer at the ZnO/substrate interface. An additional possibility is to increase the bandgap of the piezo layer by incorporating magnesium. This could increase the bandgap sufficiently to allow the transmission of the excitation laser to the optical layer through the front side of the film, thus opening up a significantly wider range of substrates for growth purposes.

Bibliography

1. M. Faraday, *On conducting power generally.* Experimental Researches in Electricity, 1839. **1**(1).
2. F. Braun, *Uber die Stromleitung durch Schwefelmetalic.* Annalen der Physik and Chemie, 1874. **153**(4): p. 556-553.
3. H. J. Round, *A Note on Carborundum.* Electrical World, 1907. **49**: p. 309.
4. F. J. Manjon, K. Syassen, and R. Lauck, *Effect of pressure on phonon modes in wurtzite zinc oxide.* High Pressure Research, 2002. **22**(2): p. 299-304.
5. J. Serrano, et al., *Pressure dependence of the lattice dynamics of ZnO: An ab initio approach.* Physical Review B, 2004. **69**(9): p. 094306 (1-13).
6. A. A. Ashrafi, et al., *Role of ZnS buffer layers in growth of zincblende ZnO on GaAs substrates by metalorganic molecular-beam epitaxy.* Journal of Crystal Growth, 2000. **221**: p. 435-439.
7. U. Rossler, *Energy bands of hexagonal 2-6 semiconductors.* Physical Review, 1969. **184**(3): p. 733.
8. R. Thangavela, M. Rajagopalanb, and J. Kumara, *Theoretical investigations on ZnCdO2 and ZnMgO2 alloys: A first principle study.* Solid State Communications, 2006. **137**(9): p. 507-511.
9. B. K. Meyer, et al., *Bound exciton and donor-acceptor pair recombinations in ZnO.* phys. stat. sol., 2004. **241**(2): p. 231-260.
10. D. C. Reynolds, et al., *Valence-band ordering in ZnO.* Physical Review B, 1999. **60**(4): p. 2340-2344.
11. A. Teke, et al., *Excitonic fine structure and recombination dynamics in single-crystalline ZnO.* Physical Review B, 2004. **70**(19): p. 195207.
12. J. W. Wang, et al., *Enhanced p-type ZnO films through nitrogen and argentum codoping grown by ultrasonic spray pyrolysis* Chinese Physics Letters, 2008. **25**(9): p. 3400-3402.
13. F. Y. Mao, et al., *High quality p-type ZnO film growth by a simple method and its properties.* Chinese Science Bulletin, 2008. **53**(17): p. 2582-2585.
14. G. D. Yuan, et al., *p-type ZnO nanowire arrays.* Nano Letters, 2008. **8**(8): p. 2591-2597.
15. R. Triboulet and Jacques Perriere, *Epitaxial growth of ZnO films.* Progress in Crystal Growth and Characterisation of Materials, 2003. **47**: p. 65-138.
16. S. J. Pearton, et al., *Recent progress in processing and properties of ZnO.* Progress in Materials Science, 2005. **50**(3): p. 293-340.
17. U. Ozgur, et al., *A comprehensive review of ZnO materials and devices.* Journal of Applied Physics, 2005. **98**(4): p. 041301
18. D. C. Look, et al., *The future of ZnO light emitters.* Physica Status Solidi A-applied research, 2004. **201**(10): p. 2203-2212.
19. C. L. Zhang, W. N. Zhou, and Y. Hang, *Hydrothermal growth and characterization of ZnO crystals* Journal of Crystal Growth, 2008. **310**(7-9): p. 1819-1822.
20. A. Y. Cho and S.E. Stokowsk, *Molecular Beam Epitxay and Optical Evaluation of Alxgal-Xas.* Solid State Communications, 1971. **9**: p. 565.

21. M. A. L. Johnson, et al., *MBE growth and properties of ZnO on sapphire and SiC substrates.* Journal of Electronic Materials, 1996. **25**: p. 855-862.
22. Y. F. Chen, D. M. Bagnall, and Z. Q. Zhu, *Growth of ZnO single crystal thin films on c-plane (0 0 0 1) sapphire by plasma enhanced molecular beam epitaxy.* Journal of Crystal Growth, 1997. **181**(1-2): p. 165-169.
23. H. B. Kang, et al., *Single-crystalline ZnO films grown on (0001)Al2O3 substrate by electron cyclotron resonance-assisted molecular beam epitaxy technique* Japanese Journal of Applied Physics, 1997. **36**(7B): p. L933-L955.
24. S. Yamauchi, et al., *Low temperature epitaxial growth of ZnO layer by plasma-assisted epitaxy.* Thin Solid Films, 1999. **345**(1): p. 12-17.
25. S. Yamauchi, et al., *Plasma-assisted epitaxial growth of ZnO layer on sapphire.* Journal of Crystal Growth, 2000. **214-215**: p. 63-67.
26. S. Yamauchi, Y. Goto, and T. Hariu, *Photoluminescence studies of undoped and nitrogen-doped ZnO layers grown by plasma-assisted epitaxy.* Journal of Crystal Growth, 2004. **260**(1-2): p. 1-6.
27. P. Fons, et al., *Growth of high-quality epitaxial ZnO films on α-Al2O3.* Journal of Crystal Growth, 1999. **201-202**: p. 627-632.
28. Yefan Chen, et al., *Two-dimensional growth of ZnO films on sapphire(0 0 0 1) with buffer layers.* Journal of Crystal Growth, 2000. **214-215**: p. 87-91.
29. Soon-Ku Hong, et al., *Control of polarity of heteroepitaxial ZnO films by interface engineering.* Applied Surface Science, 2002. **190**(1-4): p. 491-497.
30. A. Setiawan, et al., *Study on MgO buffer in ZnO layers grown by plasma-assisted molecular beam epitaxy on Al2O3(0001).* Thin Solid Films, 2003. **445**(2): p. 213-218.
31. H. J. Ko, et al., *MBE growth of high-quality ZnO films on epi-GaN.* Journal of Crystal Growth, 2000. **209**(4): p. 816-821.
32. Soon-Ku Hong, et al., *Control and characterization of ZnO/GaN heterointerfaces in plasma-assisted MBE-grown ZnO films on GaN/Al2O3.* Applied Surface Science, 2000. **159-160**: p. 441-448.
33. Hang-Ju Ko, et al., *A challenge in molecular beam epitaxy of ZnO: control of material properties by interface engineering.* Thin Solid Films, 2002. **409**(1): p. 153-160.
34. Y. M. Lu, et al., *Effects of low-temperature-grown ZnO buffer layer and Zn/O ratio on the properties of high-temperature-overgrown ZnO main layer on Si substrate by MBE.* Journal of Crystal Growth, 2007. **301-302**: p. 373-377.
35. K. Sakurai, et al., *Effects of substrate offset angles on MBE growth of ZnO.* Journal of Crystal Growth, 2000. **214-215**: p. 92-94.
36. K. Nakahara, et al., *Growth and characterization of undoped ZnO films for single crystal based device use by radical source molecular beam epitaxy (RS-MBE).* Journal of Crystal Growth, 2001. **227-228**: p. 923-928.
37. P. Fons, et al., *Nucleation and growth of ZnO on sapphire substrates using molecular beam epitaxy.* Journal of Crystal Growth, 2001. **227-228**: p. 911-916.
38. X. Wang, et al., *Growth and photoluminescence for undoped and N-doped ZnO grown on 6H-SiC substrate.* Journal of Luminescence, 2007. **122-123**: p. 165-167.
39. H. Kumano, et al., *Luminescence properties of ZnO films grown on GaAs substrates by molecular-beam epitaxy excited by electron–cyclotron resonance oxygen plasma.* Journal of Crystal Growth, 2000. **214-215**: p. 280-283.

40. K. Iwata, et al., *ZnO growth on Si by radical source MBE.* Journal of Crystal Growth, 2000. **214-215**: p. 50-54.
41. K. Ogata, et al., *Effects of thermal annealing of ZnO layers grown by MBE.* Journal of Crystal Growth, 2000. **214**: p. 312-315.
42. Y. W. Heo, et al., *Growth of ZnO thin films on c-plane Al2O3 by molecular beam epitaxy using ozone as an oxygen source.* Applied Surface Science, 2006. **252**(20): p. 7442-7448.
43. L. P. Schuler, *Properties and characterisation of sputtered zinc oxide.* PhD Thesis, University of Canterbury holdings, 2008.
44. I. S. Jeong, et al., *n-ZnO/p-Si U photodetectors employing AlO films for antireflection.* Thin Solid Films, 2004. **447-448**: p. 111-114.
45. Y. P. Varshni, Physica, 1967. **34**: p. 149.
46. R. Passler, et al., *Temperature dependence of exciton peak energies in ZnS, ZnSe, ZnTe epitaxial films.* Journal of Applied Physics, 1999. **86**(8): p. 4403-4411.
47. M. Fernandez, et al., Physical Review B, 1997. **55**: p. 7660.
48. A. Manoogian and J.C. Woolley, Canadian Journal of Physics, 1984. **62**: p. 285.
49. D. W. Hamby, et al., *Temperature dependent exciton photoluminescence of bulk ZnO.* Journal of Applied Physics, 2003. **93**(6): p. 3214-3217.
50. C. Rincon, et al., *Temperature dependence of the photoluminescence spectra os single crystals of CulnTe2.* Journal of Applied Physics, 1997. **82**(9): p. 4500-4503.
51. L. Vina, S. Logothetidis, and M. Cardona, Physical Review B, 1984. **30**: p. 1979.
52. T. Schmidt, K. Lischka, and W. Zulehner, *Excitation-power dependence of the near band-edge photoluminescence of semiconductors.* Physical Review B, 1992. **45**(16): p. 8989-8994.
53. B. Gil and A. V. Kavokin, *Giant exciton-light coupling in ZnO quantum dots.* Applied Physics Letters, 2002. **81**(4): p. 748-750.
54. N. N. Syrbu, et al., *Exciton polariton spectra and carrier effective masses in ZnO single crystals* Physica B-condensed matter, 2004. **353**(1-2): p. 111-115.
55. K. Hummer and P. Gebhardt, *Angular-dependence of reflection spectra and directional dispersion of anisotropic exciton polaritons in ZnO.* Physica Solidi B-basic research, 1978. **85**(1): p. 271-282.
56. K. Hummer and P. Gebhardt, *Interband magnetoreflection of ZnO.* Physica Status Solidi B-basic research, 1973. **65**(1): p. 249-260.
57. T. C. Collins, AIP Conf Proceedings 557: 183 2001, 2001.
58. S. F. Chichibu, et al., *Polarized photoreflectance spectra of excitonic polaritons in a ZnO single crystal.* Journal of Applied Physics, 2003. **93**(1): p. 756-758.
59. S. F. Chichibu, et al., *Photoreflectance spectra of a ZnO heteroepitaxial film on the nearly lattice-matched ScAlMgO4 (0001) substrate grown by laser molecular-beam epitaxy.* Applied Physics Letters, 2002. **80**(16): p. 2860-2862.
60. J. Lagois, *Excitonic surface-polaritons in anisotropic ZnO crystals* Solid State Communications, 1981. **39**(4): p. 563-567.
61. M. Zamfirescu, et al., *ZnO as a material mostly adapted for the realization of room-temperature polariton lasers.* Physical Review B, 2002. **65**(16): p. 161205.

62. H. Alves, et al., *Optical investigations on excitons bound to impurities and dislocations in ZnO.* Optical Materials, 2003. **23**(1-2): p. 33-37.
63. S. J. Xu, Shi-Jie Xiong, and S.L. Shi, *Resonant coupling of bound excitons with LO phonons in ZnO: Excitonic polaron states and Fano interference.* Journal of Chemical Physics, 2005. **123**: p. 221105.
64. Kui-juan Jin and S.J. Xu, *Fano resonance in the luminescence spectra of donor bound excitons in polar semiconductors.* Applied Physics Letters, 2007. **90**(3): p. 032107.
65. D. C. Look, et al., *Characterization of homoepitaxial p-type ZnO grown by molecular beam epitaxy* Applied Physics Letters, 2002. **81**(10): p. 1830-1832.
66. S. Guha, et al., *Temperature-dependent photoluminescence of organic semiconductors with varying backbone conformation.* Physical Review B, 2003. **67**(12): p. 125204.
67. M. W. Allen, et al., *Influence of spontaneous polarization on the electrical and optical properties of bulk, single crystal ZnO.* Applied Physics Letters, 2007. **90**: p. 062104.
68. D. C. Reynolds, D. C. Look, and B. Jogai, *Fine structure on the green band in ZnO.* Journal of Applied Physics, 2001. **89**(11): p. 6189-6191.
69. R. Dingle, *Luminescent transitions associated with divalent copper impurities and green emission from semiconducting zinc oxide.* Physical Review Letters, 1969. **23**(11): p. 579-582.
70. N. Y. Garces, et al., *Role of copper in the green luminescence from ZnO crystals.* Applied Physics Letters, 2002. **81**(4): p. 622-624.
71. K. Vanheusden, et al., *Correlation between photoluminescence and oxygen vacancies in ZnO phosphors.* Applied Physics Letters, 1995. **68**(3): p. 403-405.
72. S. A. Studenikin, N. Golego, and M. Cocivera, *Fabrication of green and orange photoluminescent, undoped ZnO films using spray pyrolysis.* Journal of Applied Physics, 1998. **84**(4): p. 2287-2294.
73. K. Vanheusden, et al., *Mechanisms behind green photoluminescence in ZnO phosphor powders.* Journal of Applied Physics, 1996. **79**(10): p. 7983-7990.
74. X. Q. Meng, et al., *The structural and optical properties of ZnO nanorod arrays.* Solid State Communications, 2005. **135**(3): p. 179-182.
75. N. E. Hsu , W. K. Hung, and Y.F. Chen, *Origin of defect emission identified by polarized luminescence from aligned ZnO nanorods.* Journal of Applied Physics, 2004. **96**(8): p. 4671-4673.
76. A. Van Dijken, et al., *Identification of the transition responsible for the visible emission in ZnO using quantum size effects.* Journal of Luminescence, 2000. **90**(3-4): p. 123-128.
77. A. Van Dijken, et al., *The luminescence of nanocrystalline ZnO particles: the mechanism of the ultraviolet and visible emission.* Journal of Luminescence, 2000. **87-89**: p. 454-456.
78. F. K. Shan, et al., *Aging effect and origin of deep-level emission in ZnO thin film deposited by pulsed laser deposition.* Applied Physics Letters, 2005. **86**(22): p. 221910.
79. S. H. Jeong, B. S. Kim, and B.T. Lee, *Photoluminescence dependence of ZnO films grown on Si(100) by radio-frequency magnetron sputtering on the growth ambient* Applied Physics Letters, 2003. **82**(16): p. 2625-2627.

80. X. Liu, et al., *Growth mechanism and properties of ZnO nanorods synthesized by plasma-enhanced chemical vapor deposition.* Journal of Applied Physics, 2004. **95**(6): p. 3141-3147.
81. M. Liu, A. H. Kitai, and P. Mascher, *Point-Defects and Luminescence-centers in zinc oxide and zinc oxide doped with manganese.* Journal of Luminescence, 1992. **54**(1): p. 35-42.
82. Y. W. Heo, D. P. Norton, and S.J. Pearton, *Origin of green luminescence in ZnO thin film grown by molecular-beam epitaxy.* Journal of Applied Physics, 2005. **98**(7): p. 073502.
83. A. Zubiaga, et al., *Correlation between Zn vacancies and photoluminescence emission in ZnO films* Journal of Applied Physics, 2006. **99**(5): p. 053516.
84. Q. X. Zhao, et al., *Deep-level emissions influenced by O and Zn implantations in ZnO.* Applied Physics Letters, 2005. **87**(21): p. 211912.
85. B. X. Lin, Z. X. Fu, and Y. B. Jia, *Green luminescent center in undoped zinc oxide films deposited on silicon substrates* Applied Physics Letters, 2001. **79**(7): p. 943-945.
86. Y. M. Sun, et al., *A FP-LMTO study on the native shallow donor in ZnO.* Journal of Electron Spectroscopy and Related Phenomena, 2001. **114**: p. 1123-1125.
87. I. Broser, et al., *Local vibrational modes of the CuO4-cluster in ZnO.* Journal of Crystal Growth, 1996. **159**: p. 889-892.
88. W. C. T. Lee, et al., *Effect of annealing on the morphology and optoelectrical characteristics of ZnO thin films grown by plasma-assisted molecular beam epitaxy.* Journal of Electronic Materials, 2006. **35**(6): p. 1316-1321.
89. W. C. T. Lee, et al., *Effects of plasma conditions on properties of ZnO films grown by plasma-assisted molecular beam epitaxy.* Journal of Vacuum Science and Technology B, 2006. **24**(3): p. 1514-1518.
90. J. Narayan, et al., *Defects and interfaces in epitaxial ZnO/alpha-Al2O3 and AlN/ZnO/alpha-Al2O3, heterostructures.* Journal of Applied Physics, 1998. **84**(5): p. 2597-2601.
91. S. P. Chang, et al., *ZnO epitaxial layers grown on nitridated Si (1 0 0) substrate with HT-GaN/LT-ZnO double buffer.* Journal of Crystal Growth, 2008. **310**: p. 290-294.
92. X. N. Wang, et al., *Low-temperature interface engineering for high-quality ZnO epitaxy on Si(111) substrate.* Applied Physics Letters, 2007. **90**(15): p. 151912.
93. W. C. T. Lee, *Harvesting Philosphers Wool: A study in the growth, structure and optoelectrical behaviour of epitaxial ZnO.* PhD Thesis, University of Canterbury holdings, 2008.
94. K. Hirano, et al., *ZnO epitaxial films grown by flux-modulated RF-MBE.* Journal of Crystal Growth, 2007. **301**: p. 370-372.
95. H. J. Ko, et al., *Investigation of ZnO epilayers grown under various Zn/O ratios by plasma-assisted molecular-beam epitaxy.* Japanese Journal of Applied Physics, 2002. **92**(8): p. 4354-4360.
96. H. Kato, et al., *Homoepitaxial growth of high-quality Zn-polar ZnO films by plasma-assisted molecular beam epitaxy.* Japanese Journal of Applied Physics Part 2-Letters, 2003. **42**(8B): p. L1002-L1005.
97. K. Nakahara, et al., *Growth of N-doped and Ga+N-codoped ZnO films by radical source molecular beam epitaxy.* Journal of Crystal Growth, 2002. **237-239**: p. 503-508.

98. S. H. Park, et al., *Lattice deformation of ZnO films with high nitrogen concentration.* Applied Surface Science, 2008.
99. H. B. Bebb and E. W. Williams, Semiconductors and Semimetals, 1972. **8**: p. 181.
100. H. Kitabayashi and P. M. Smith, *Analysis of SAW propagation in gratings on ZnO/diamond substrates* IEEE Transactions on ultrasonic ferroelectrics and frequency control, 2001. **48**(1): p. 249-261.
101. M. B. Assouar, et al., *Modelling of SAW filter based on ZnO/diamond/Si layered structure including velocity dispersion* Applied Surface Science, 2000. **164**: p. 200-204.
102. J. G. Smits, et al., *Resonant diaphragm pressure measurement system with ZnO on Si excitation.* Sensors and Actuators, 1983. **4**(4): p. 565-571.
103. S. Muthukumar, et al., *Control of morphology and orientation of ZnO thin films grown on SiO2/Si substrates.* Journal of Crystal Growth, 2001. **225**(2-4): p. 197-201.
104. F. S. Hickernell, *DC triode sputtered zinc oxide surface elastic wave transducers.* Journal of Applied Physics, 1973. **44**(3): p. 1061-1071.
105. T. Mitsuyu, O. Yamazaki, and K. Wasa, *A 4.4 GHz SAW filter using a single-crystal ZnO film on sapphire.* IEEE transactions on sonics and ultrasonics, 1982. **29**(3): p. 191.
106. T. Shiosaki, M. Adachi, and A. Kawabata, *Sputtering and chemical vapor-deposition of piezoelectric ZnO, AlN and K3Li2Nb5O15 films for optical-waveguides and surface acoustic-wave devices.* Thin Solid Films, 1982. **96**(2): p. 129-140.
107. G. Perluzzo, C. K. Jen, and E.L. Adler, *Characteristics of reactive magnetron sputtered ZnO films.* Ultrasonics Symposium-1989, 1989: p. 373-376.
108. M. Kadota, T. Kasanami, and M. Minakata, *Characteristics of ZnO films on glass substrates deposited by RF mode electron cyclotron resonance sputtering system.* Electronic Letters, 1993. **28**: p. 2315-2316.
109. J. J. Chen, et al., *Effect of sputtering oxygen partial pressure on structure and physical properties of high resistivity ZnO films.* Applied Surface Science, 2003. **223**: p. 318-329.
110. F. Moeller, et al., *Properties of ZnO layers on oxidised silicon.* Ultrasonics Symposium-1994, 1994: p. 403-405.
111. D. Song, D. H. Neuhaus, and J. Xia, *Structure and characteristics of ZnO:Al/n-Si heterojunctions prepared by magnetron sputtering.* Thin Solid Films, 2002. **422**(1-2): p. 180-185.
112. S. Takada, *Relation between optical property and crystallinity of ZnO thin-films prepared by RF Magnetron sputtering.* Journal of Applied Physics, 1993. **73**(10): p. 4739-4742.
113. T. Hata, et al., Applied Physics Letters, 1980. **37**(10): p. 633-635.
114. T. Yamamoto, T. Shiosaki, and A. Kawabata, *Characterization of ZnO piezoelectric films prepared by RF planar-magnetron sputtering.* Journal of Applied Physics, 1980. **51**(6): p. 3113-3120.
115. L. P. Schuler, et al., *Comparison of DC and RF sputtered zinc oxide films with post-annealing and dry etching and effect on crystal composition.* Japanese Journal of Applied Physics, 2005. **44**(10): p. 7555-7560.
116. C. H. Choi and S. H. Kim, *Effects of post-annealing temperature on structural, optical, and electrical properties of ZnO and Zn(1-x)Mg(x)O films*

by reactive RF magnetron sputtering. Journal of Crystal Growth, 2005. **283**: p. 170-179.
117. W. S. Shi, O. Agyeman, and C.N. Xu, *Enhancement of the light emissions from zinc oxide films by controlling the post-treatment ambient* Journal of Applied Physics, 2002. **91**(9): p. 5640-5644.
118. M. K. Ryu, et al., *Postgrowth annealing effect on structural and optical properties of ZnO films grown on GaAs substrates by the radio frequency magnetron sputtering technique* Journal of Applied Physics, 2002. **91**(1): p. 110-116.
119. K. Ozaki and M. Gomi, *Strong ultraviolet photoluminescence in polycrystalline ZnO sputtered films* Japanese Journal of Applied Physics, 2002. **41**(9): p. 5614-5617.
120. T. W. Kim, et al., *Effect of thermal annealing on the surface and the microstructural properties of ZnO thin films grown on p-Si (100) substrates.* Journal of Crystal Growth, 2004. **262**(1-4): p. 72-77.
121. Y. G. Wang, et al., *Enhancement of near-band-edge photoluminescence from ZnO films by face-to-face annealing.* Journal of Crystal Growth, 2003. **259**: p. 335-342.
122. R. J. Mendelsberg, et al., *Carbon enhanced blue-violet luminescence in ZnO films grown by pulsed laser deposition.* Current Applied Physics, 2007. **8**(3-4): p. 283-286.
123. B. H. Kong, et al., *Optical and structural properties of ZnO thin films grown on various substrates by metalorganic chemical vapor deposition.* Physica B-condensed matter, 2007. **401**: p. 399-403.
124. L. P. Schuler, et al., *The effect of substrate material and postannealing on the photoluminescence and piezo properties of DC-sputtered ZnO.* Journal of Electronic Materials, 2006. **36**(4): p. 507-518.
125. D. Song, et al., *Comparative study of ZnO:Al films on Si and glass prepared by RF magnetron sputtering at room temperature.* IEEE, 2002: p. 239-242.